DEWETTING OF THIN SOLID FILMS

MODELING, ANALYSIS AND NUMERICAL SIMULATION

vorgelegt von

Diplom- Mathematikerin
Marion Dziwnik

geboren in Crailsheim

von der Fakultät II - Mathematik und Naturwissenschaften
der Technischen Universität Berlin
zur Erlangung des akademischen Grades

Doktor der Naturwissenschaften
- Dr. rer. nat. -

genehmigte Dissertation

Promotionsausschuss:

Vorsitzender:	Prof. Dr. Peter Bank
Gutachter:	Prof. Dr. Andreas Münch
Gutachterin:	Prof. Dr. Barbara Wagner
Gutachter:	Prof. Dr. Tom Witelski

Tag der wissenschaftlichen Aussprache: 17. März 2016

Berlin 2016

Dedicated to the loving memory of Sigrid Born.

1927 – 2015

DEWETTING OF THIN SOLID FILMS
MODELING, ANALYSIS AND NUMERICAL SIMULATION

MARION DZIWNIK

ABSTRACT. This dissertation is devoted to the mathematical study of solid state dewetting and deals with various mathematical topics such as phase field modeling, the derivation of corresponding sharp interface limits, existence of solutions, numerical simulations and linear stability analysis of the dewetting front.

We start with the formulation of a two-dimensional anisotropic phase field model for solid state dewetting on a solid substrate. The evolution is described by a Cahn-Hilliard type equation with a bi-quadratic degenerate mobility and a polynomial homogeneous free energy. We propose an anisotropic free boundary condition at the film/substrate contact line which correspond to the natural boundary condition from the variational derivation. We show via matched asymptotic analysis that the resulting sharp interface model is consistent with the pure surface diffusion model. In addition, we show that the corresponding natural boundary conditions at the substrate imply a contact angle condition which is known as Young-Herring condition.

We provide an existence result for the present degenerate partial differential equation on a simplified domain with homogeneous Neumann boundary conditions. Under the assumption that the strength of the anisotropy is sufficiently small, we establish certain convexity properties and higher order bounds of the strongly non-linear anisotropic operator. This enables to prove existence of weak solutions. Furthermore, we show that solutions are bounded by one without having a maximum principle.

Completing the part which is concerned with the phase field representation, we consider the numerical simulation of the present model, where we apply a diffuse boundary approximation to handle the boundary conditions at the substrate. The reformulated equation can be solved by a standard finite element method. A matched asymptotic analysis shows that solutions of the re-formulated equations formally converge to those of the original equations. We provide numerical simulations which confirm this analysis. In addition, we address the previously discussed question of how the mobility influences the evolution and simulate dewetting scenarios for different mobilities and anisotropies.

In the last main chapter we consider a generalized class of thin film equations, including the case which corresponds to the small slope approximation of the sharp interface model for isotropic solid state dewetting. We present an improved method for the linear stability analysis of unsteady, non-uniform base states in thin film equations which exploits that the initial fronts evolve on a slower time-scale than the typical perturbations. The result is a unique value for the dominant wavelength which is different from the one obtained by the frequently applied linear stability analysis with "frozen modes". Furthermore we show that for the present class of stability problems the dispersion relation is linear in the long wave limit, which is in contrast to many other instability problems in thin film flows.

PUBLICATIONS

Some ideas and figures have appeared previously in the following publications:

- *Stability analysis of unsteady, non-uniform base states in thin film equations*, by Marion Dziwnik, Maciek Korzec, Andreas Münch and Barbara Wagner,
  published in SIAM, Multiscale Model. Simul. 12-2 (2014), pp. 755-780, doi: 10.1137/130943352
- *An anisotropic phase-field model for solid-state dewetting and its sharp-interface limit*, by Marion Dziwnik, Andreas Münch und Barbara Wagner,
  submitted to Nonlinearity- IOPscience

ACKNOWLEDGMENTS

Firstly, I would like to express my sincere gratitude to my first advisors Andreas Münch and Barbara Wagner for providing me the opportunity to research on such an interesting topic, for their motivation and immense knowledge, for their insightful comments and encouragement, which gave me confidence, but also for the hard question which have led me to widen my research from various perspectives. It was a pleasure to work with them.

I sincerely thank my mentor and co-advisor Maciek Korzec, who essentially helped me to become familiar with the issue quickly, for his patience and for the competent and custom made introduction into the numerical and analytical methods.

Besides my advisors, I would also like to thank my colleague Sebastian Jachalski for many fruitful discussions on the existence result presented in this thesis. For positive feedback as well as critical comments which helped me to improve my results.

My sincere thanks also goes to Dirk Peschka who gave me an incredibly fast introduction into the finite element method and who provided me with some first basic finite element codes. This made a significant contribution in view of the quick completion of my numerical results.

I also thank the other present and former colleagues of the research group "Mathematical Methods for Photovoltaics" at the Technical University of Berlin - Esteban, Sibylle and Tobias - for the friendly and collegiate working atmosphere.

Last but not least, I thank the "Competence Center Thin-Film- and Nanotechnology for Photovoltaics Berlin" and the Technical University of Berlin for the financial support.

CONTENTS

Part I

INTRODUCTION

1

DEWETTING OF THIN SOLID FILMS

1.1 EXPERIMENTS AND APPLICATIONS

Doing research is like exploring a city using the subway. You only really understand what it looks like on the surface after getting off at various stations.

— Maciek Korzec

"getting off at various stations"

This dissertation is devoted to the study of solid state dewetting and incorporates a variety of different mathematical topics including modeling, asymptotic analysis, numerics and existence theory. The goal is to gain a comprehensive mathematical insights into the phenomenon by examining it from various theoretical perspectives - by "getting off at various stations".

What is solid state dewetting?

When a thin solid film is heated to sufficiently high temperatures, but well below the material's melting temperature, it may lead to an interesting phenomenon. The thin film may dewet or agglomerate to form islands, similar as in the liquid state, while it still remains solid. This process is called solid state dewetting and is due to the fact that thin films generally occur under conditions for which atomic motion is restricted and non-equilibrium structures are obtained. As a consequence, most films are unstable, or metastable, and will spontaneously dewet via surface diffusion when heated to temperatures at which the mobility of the atoms is sufficiently high.

Applications

A fundamental understanding of the mechanisms governing solid state dewetting is desirable since it is one of the important processes used for nanostructuring and functionalizing surfaces for a variety of technological applications, such as for example in thin-film solar cells

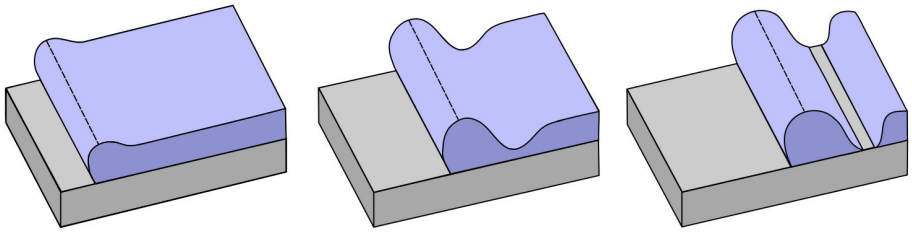

Figure 1: Schematic illustration of a retracting dewetting front showing how the rim thickens, and the valley in front of of the rim deepens. Eventually the valley touches the substrate, as shown in the third picture, leading to the formation of an isolated island and a new dewetting front which continues to retract. This process is called pinch-off.

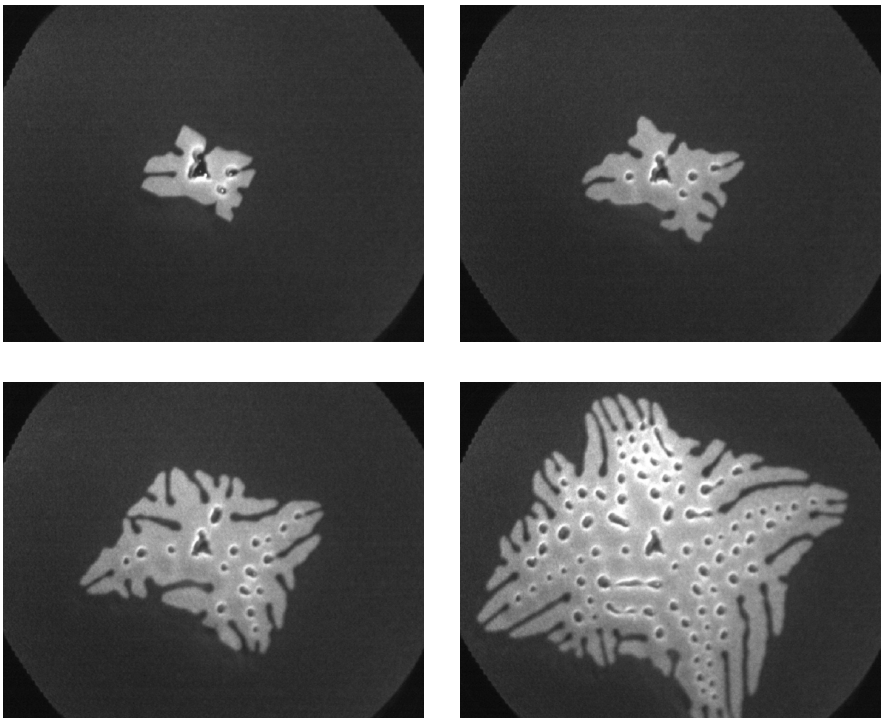

Figure 2: Typical low-energy electron microscopy (LEEM) pictures for SOI dewetting at $T = 815°C$. The silicon film appears black whereas the silicon oxide is bright. These picture sequence illustrates the void opening, the finger's growth and the island's formation. Low-energy electron microscopy (LEEM) pictures for SOI dewetting at $T = 815 \circ C$. Supplementary data (http://iopscience.iop.org/1367-2630/13/4/043017/media) taken from reference [13] with permission .

and other optoelectronic devices. On the one hand, dewetting of films creates a restriction for the fabrication of advanced devices [51] and also negatively influences the reliability of other micro-devices and systems, especially when high-temperature operations are required [99]. On the other hand, there are an increasing number of examples in which dewetting has been used positively, for example to produce self-organized nanocrystals occurring in several nanoscale processes [61] or to make particle arrays in sensors [79]. It is therefore of particular relevance to understand how to suppress dewetting when it is undesirable and how to control it when specific dewetted structures are desired.

Overview of the phenomenology

The dewetting scenario typically begins at preexisting holes, at film edges or requires the formation of new holes. Starting at the three-phase contact line between the thin solid film, the solid substrate and the surrounding vapor phase the subsequent retraction of the film leads to the accumulation of mass in the dewetting front which results in an elevated rim with a height greater than the surrounding film thickness, as qualitatively shown in Fig. 1. The rim height at the

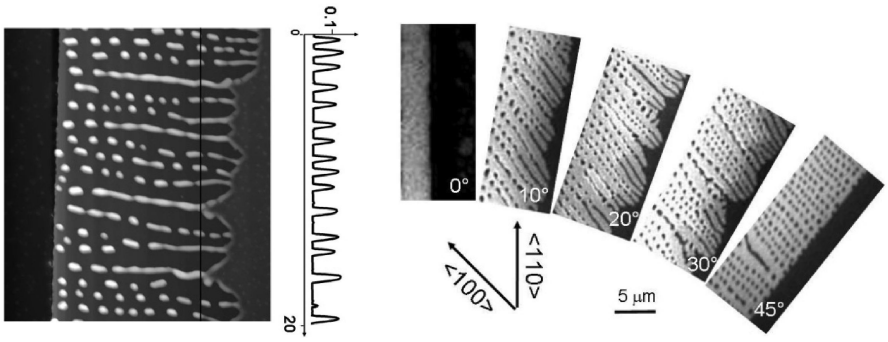

Figure 3: Left: AFM picture of an unstable $< 100 >$ front. The AFM profile (vertical and horizontal units are μm) shows that the finger instability is associated with a local height instability. Right: LEEM images (bright field) of UHV-annealed SOI artificial fronts with differing edge orientation with respect to the $< 110 >$ direction. The Si material is dark and the SiO_2 substrate is bright. The dewetting fronts form $< 100 >$ oriented Si fingers regardedless of the initial orientation. Both pictures have been taken from reference [65] with permission.

evolving front increases over time and as a consequence, the curvature at the dewetting front and the driving force for mass transport are reduced.

The following evolution is characterized by different observations, such as hole coincidence, fingering instabilities and rim pinch-off, which may also occur simultaneously. In the event that holes are sparse and don't interfere with one another, the fingering instabilities may occur with a regular and periodic distance between them, as shown in Fig 2 and Fig. 3 to the left. In particular, if considering a single crystalline film, the fingering instabilities may depend on the crystal orientation. An ultra-thin crystalline silicon-on-insulator (SOI) film, for example, only provides instabilities in the $< 100 >$ oriented front, while the $< 110 >$ front is stable, as documented in Fig. 3.

Fingering instabilities

The late stages of dewetting are characterized by rim pinch-off and agglomeration into an assembly of islands which leads to a system of more stable configurations. The equilibrium shape of these islands corresponds to the minimum of the surface energy for a fixed volume and satisfies particular boundary conditions which also depend on the surface energy of the substrate. For islands with isotropic surface energy, the equilibrium shape is a simple regular droplet and the particular isotropic boundary conditions prescribe a fixed contact angle. If the surface energy is not isotropic, then its equilibrium shape is determined by the Wulff construction [115], or Winterbottom construction [112] if including a substrate, respectively. In the Wulff construction the equilibrium shape of a crystal is determined graphically in two main steps. To begin, the surface energy is represented in a polar plot as a function of orientation, the so-called gamma plot. The next step is to draw lines from the origin to every point on the gamma plot and

Pinch- off and equilibrium shapes

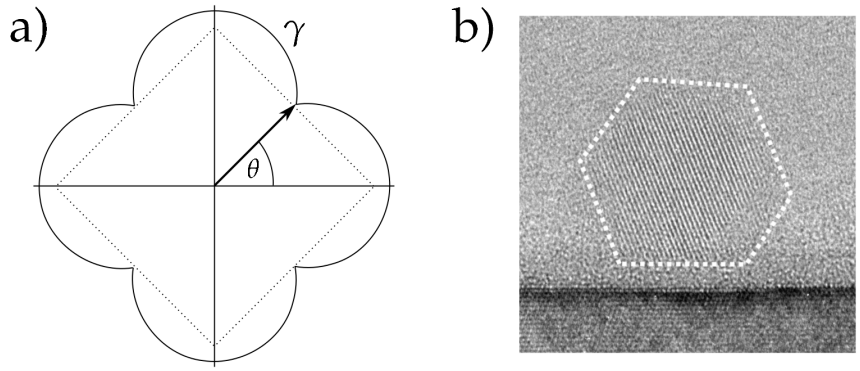

Figure 4: a) A polar plot of the surface energy (solid line) and the corresponding equilibrium shape (dotted line) determined by the Wulff construction, i.e. the equilibrium shape of the corresponding interface energy is described by the envelope of lines drawn normal to the orientation vectors at each point of the gamma plot, in this case a simple square shape. b) Cross-sectional TEM image of a crystalline silicon equilibrium dot sitting on a SiO_2 layer that is located on top of a Si(111) wafer. The experimental picture is shown with permission of Maurizio Roczen (Experimental Physics, HU Berlin)

planes perpendicular to these lines at the points where they intersect the gamma plot. The equilibrium shape of the crystal is then described by the inner envelope of these planes. In the case of a two-dimensional crystal, this leads to a surface energy plot such as for example shown in Fig. 4 a). This gamma plot has four cusps at which the surface energy is minimized which correspond to facets on the equilibrium shape of the crystal. The equilibrium shape can be determined by finding the envelope of lines drawn normal to the orientation vectors at each point of the gamma plot. In the case shown in Fig. 4 a), the equilibrium shape is a simple square shape, displayed as a dotted line.

The underlying physics

Whilst the dynamical evolution has many similarities with the dewetting of thin liquid films, which has been investigated in numerous theoretical and experimental studies [3, 58, 95, 96] and recently reviewed in [20], solid dewetting has not received as much attention. The physical mechanisms underlying the mass transport of dewetting of solid films is also quite distinct and is based on capillarity driven surface diffusion [54, 104, 114]. In addition, further properties such as anisotropy of its surface energy can dominate the dynamics [27, 105, 121], having important implication for the stability of the moving three-phase contact-line - where vapor, solid film and solid substrate meet.

There are mainly two kinds of continuum models for solid state dewetting - sharp interface and diffuse interface/phase field models. Both have been applied in the past in order to simulate and analyze

solid state dewetting and there are further model reductions with significantly simplify the analysis. The following section provides a brief overview of the different kinds of models and motivates the particular suitability for different mathematical approaches. This provides the basis for the subsequent outline of the mathematical topics.

1.2 MODELS FOR SOLID STATE DEWETTING

The phase field model: a powerful candidate for simulation

As the dynamical dewetting process usually involves a succession of topological transitions of the thin dewetting film, the phase field framework provides an adequate modeling approach for a continuum description. The basic idea is to substitute the equation for the interface with a partial differential equation for the evolution of an auxiliary field, the phase field, that plays the role of an order parameter. This auxiliary field takes two distinct values in each of the phases, for example "$+1$" in the solid phase and "-1" in the vapor phase, with a smooth transition layer between both phases in the zone around the interface. The new interface is then diffuse with a finite width and the discrete location of the interface may be defined as the zero level set of the phase field function.

Advantages and disadvantages

The great advantage of this representation is that it allows the creation and vanishing of interfaces to occur naturally as part of the solution and it also enables to easily deal with present complex geometries. Thus, the phase field method represents a powerful candidate for simulation and has already been successfully applied to a number of similar problems [52, 94, 106]. In comparison, the numerical simulation of sharp interface models has to separately handle topological changes and the computation of fourth-order derivatives along the surface presents a challenge for the frequently used interface tracking methods [24, 26, 114]. For a discussion of the different methods concerning the numerical simulation of thin crystalline films we refer to the review article by Li et al. [67]. On the other hand the derivation of a phase field model contains particular degrees of freedom, e.g. regarding the choices for the bulk free energy and the mobility, which implies that there exists no unique phase field representation for a particular physical process. Therefore the use of phase field models as a numerical tool requires careful consideration in view of the correct physical relationship [40, 64].

From phase field to sharp interface

The proper correspondence is given by the sharp interface limit, i.e. the limit equation if the thickness of the diffuse interface in the phase field framework tends to zero. This limit equation has to coincide with the corresponding sharp interface model which has a direct physical interpretation and unique representation. Establishing this correspondence between phase field and sharp interface models has therefore been investigated intensively during the last decades, see for example the review by [87].

From sharp interface to thin film model

A basic property of the thin solid films which we consider here is that the characteristic height scale of the initial film is much smaller than the length scale. Under the additional assumption that the present slopes are small, we are able to reduce the sharp interface model to a particular case of the so-called thin film equation. This significant model reduction does not only simplify the numerical simulation, it also enables to systematically study some of the characteristic dewetting properties such as the dewetting rate or fingering instabilities of the dewetting front.

1.3 CONTENT, RESULTS AND STRUCTURE OF THIS STUDY

Part I: Models for solid state dewetting

This dissertation begins with a derivation of the different models for surface diffusion dewetting. We first introduce a two-dimensional phase field model which includes weakly anisotropic surface energies and a free boundary condition at the film-substrate contact line. The evolution is generally described by a Cahn-Hilliard type equation and this first model derivation leaves particular degrees of freedom for further modeling. We then present the sharp interface model which corresponds to evolution by pure surface diffusion. The contact angle boundary condition at the moving contact line is derived via the variational method and is a result of surface energy minimization. The modeling section is completed by a small slope approximation for the previously derived sharp interface model which leads to a particular case of the so-called thin film equations. The further division of this dissertation then refers to the particular models. The phase field model is the main topic of Part II, in which also the corresponding sharp interface model will be discussed. Part III refers to a generalized class of thin film equations including the case which corresponds to the small slope approximation of the sharp interface model for isotropic solid state dewetting.

Part II: The phase field model

Part II begins with the formulation of a complete phase field model for solid state dewetting and includes the particular choices for the degrees of freedom which we have left open in the first model approach. In contrast to the frequently used quadratic degenerate mobility, we chose a bi-quadratic one in combination with a polynomial homogeneous free energy. The question naturally arises as to whether the resulting model recovers motion by pure surface diffusion. Establishing the correct correspondence is the subject of Chapter 3, where the sharp interface limits of the phase field model are derived via matched asymptotic analysis. Since the standard matched asymptotic derivations lead to inner and outer expansions, which can not be matched by terms of polynomial orders of the small parameter, the present asymptotic analysis requires the incorporation of multiple interfacial layers and techniques of exponential matching.

Sharp interface limits

The second part of Chapter 3 is concerned with the inclusion of the

A matching method for the solid boundary

boundary conditions at the solid substrate. We introduce a matching method which exploits an additional inner layer about the solid substrate and a particular geometry in order to derive the corresponding sharp interface limits of the boundary conditions at the substrate. In particular, the method allows to match the inner and outer layers without matching "into the substrate", which is not well-defined. As a result we obtain that the sharp interface limits of the boundary conditions at the substrate recover the Young-Herring equation for the contact angle, and Young's equation in the isotropic case. The matching is completed by a balance of fluxes condition at the contact line. The results, which are presented in this chapter, have been submitted to Nonlinearity in a joint paper by Dziwnik, Münch and Wagner and publication is expected soon.

Existence of solutions

Chapter 4 provides an existence result for the present phase field model, which can be classified as an anisotropic version of the Cahn-Hilliard equation with degenerate mobility. The Cahn-Hilliard equation, even with degenerate mobility, has been studied intensively in the past [2, 4, 32, 71, 91], but little mathematical analysis has been done for the case where the surface energy is anisotropic. The combination of both - a degenerate mobility and an anisotropic free energy - represents a mathematical challenge in order to prove the existence of weak solutions. Focusing on this mathematical difficulty, the corresponding chapter considers homogeneous Neumann boundary conditions and a rectangular domain. Under the assumption that the strength of the anisotropy is sufficiently small, we establish certain convexity properties and higher order bounds of the strongly non-linear anisotropic operator. This enables to prove existence of weak solutions in $L^\infty(0,T;H^1(\Omega)) \cap C([0,T];L^2(\Omega))$. In addition, we show that solutions are bounded by one without having a maximum principle.

Numerical simulation

Completing Part II, we discuss the numerical simulation of the phase field model in Chapter 5. The numerical algorithm presented in this dissertation has a long history of development and deals with a variety of numerical challenges, such as the strong nonlinearity, anisotropy, high derivatives and anisotropic boundary conditions. There are additional less than obvious numerical difficulties, which just became apparent during the process of developing the numerical code. This gave us the opportunity to steadily built our knowledge about applying particular methods and implementing the present nonlinear structures. The result is a semi-implicit time-stepping method, applying the finite element method and providing a diffuse boundary approximation which significantly simplifies the implementation of the anisotropic boundary conditions at the substrate. We use the method of matched asymptotic expansions in order to show that solutions of the problem including the diffuse boundary approximation converge to those of the original problem. Finally, we present numerical simulations for various initial states which demonstrate the diffuse

boundary approximation and reveal some interesting characteristics of solid state dewetting. Motivated by the previous chapters, we address the question of how the mobility influences the evolution. We compare the result with bi-quadratic degenerate mobility to the simulation with quadratic mobility and demonstrate a significant difference. Furthermore we consider various pinch-off scenarios and anisotropies.

Part III: The thin film model, linear stability analysis

Part III refers to a whole class of thin film equations which includes the case corresponding to the small slope approximation of the sharp interface model for surface diffusion dewetting. We present an improved method for the stability analysis of unsteady, non-uniform base states in thin film equations which exploits that the initial fronts evolve on a slower time-scale than the typical perturbations. The result is a unique value for the dominant wavelength which is different from the one obtained by the frequently applied linear stability analysis with "frozen modes". Furthermore, we show that for the present class of stability problems the dispersion relation is linear in the long wave limit, which is in contrast to many other instability problems in thin film flows. The results, which are presented in this chapter, are published in a joint paper by Dziwnik, Korzec, Münch and Wagner (see [28]).

The dissertation finishes with a summary of the main results and suggestions for future research.

2

MODELING

2.1 DERIVATION OF AN ANISOTROPIC PHASE FIELD MODEL

General derivation

A phase field model can generally be derived by physical arguments originating from an explicit expression for the free energy of the system. In this section we derive a phase field model from an anisotropic free energy which leaves the particular choices for the homogeneous free energy and mobility as degrees of freedom for further modeling, as these will be motivated at the beginning of Chapter 3.

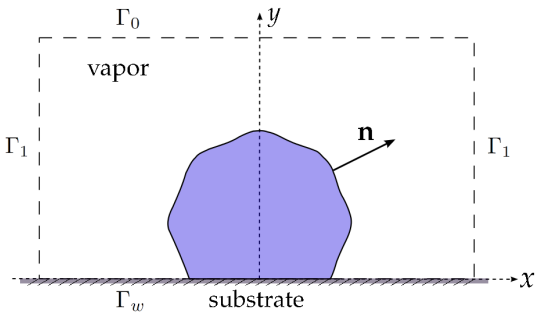

Figure 5: Sketch of the modeling domain.

Model domain and phase field function

Considering a one-dimensional film/vapor interface, we define the model domain Ω to be a two-dimensional rectangular box around this interface with boundary $\partial\Omega = \Gamma_0 \cup \Gamma_1 \cup \Gamma_w$ (see Fig. 5). Then we introduce the phase field function $u = u(\mathbf{x})$ such that the zero-level set $\chi_0 := \{\mathbf{x} : u(\mathbf{x}) = 0\}$ denotes the film/vapor interface, while $\{\mathbf{x} : u(\mathbf{x}) > 0\}$ denotes the film and $\{\mathbf{x} : u(\mathbf{x}) < 0\}$ the vapor phase. In this context the total energy of the system W^ϵ may be written as

$$W^\epsilon = W^\epsilon_{FV} + W^\epsilon_w = \int_\Omega f_{FV}\, d\Omega + \int_{\Gamma_w} f_w\, d\Gamma, \tag{1}$$

where ϵ is a small parameter that describes the interface width, W^ϵ_{FV} represents the energy of both the film and vapor phases, W^ϵ_w represents the wall energy, i.e. the energy at the substrate, and f_{FV} and f_w are the corresponding energy densities. Following the approach initiated by Kobayashi [59] and similar as in [103, 113], we consider an anisotropic free energy functional of the form

Free energy

$$f_{FV}(u, \nabla u) = \frac{\lambda_m}{\epsilon}\left(F(u) + \frac{\epsilon^2}{2}\gamma(\theta)^2|\nabla u|^2\right), \tag{2}$$

where $F(u)$ is the homogeneous free energy (whose particular choice will be motivated at the beginning of Chapter 3), $\gamma : \mathbb{R}^2 \to \mathbb{R}^+$ is the

anisotropic interface energy between film and vapor and λ_m represents the mixing energy density. In general the free energy has to fulfill $f_{FV} \to \infty$, if $|u| \to \infty$, which ensures that the energy minimizing solution has bounded order parameter, and a second stability criterion is that the highest order gradient term has positive coefficient, which ensures that the energy minimizing solution has bounded fluctuations. Furthermore the constant λ_m is needed since the ratio λ_m/ϵ produces the interfacial tension in the classical way as $\epsilon \to 0$ [49], [117]. For the scope of our work λ_m is necessary in order to obtain the correct boundary conditions at the triple junction. At this point it is also worth mentioning that the scaling in view of ϵ of this frequently used free energy differs in the literature, but the different models may be identified with each other after appropriate rescaling. The only thing which is to keep in mind, is that the different energies which contribute to the model derivation are scaled in the same way.

Anisotropy

We assume that γ is a smooth 2π-periodic function and $-\pi < \theta \leq \pi$ is the angle between $-\nabla u$ and the positive direction of the x-axis. In order to write $\gamma(\theta)$ in terms of ∇u we introduce the following common generalization of the arctangent function

$$\theta = \operatorname{atan2}(u_y, u_x) = \begin{cases} \arctan \frac{u_y}{u_x} & \text{for } u_x > 0 \\ \arctan \frac{u_y}{u_x} + \pi & \text{for } u_x < 0 \text{ and } u_y \geq 0 \\ \arctan \frac{u_y}{u_x} - \pi & \text{for } u_x < 0 \text{ and } u_y < 0 \\ + \frac{\pi}{2} & \text{for } u_x = 0 \text{ and } u_y > 0 \\ - \frac{\pi}{2} & \text{for } u_x = 0 \text{ and } u_y < 0 \\ 0 & \text{for } u_x = 0 \text{ and } u_y = 0, \end{cases} \tag{3}$$

so that

$$\gamma(\theta) = \gamma\left(\operatorname{atan2}(u_y, u_x)\right).$$

We prefer this representation of θ to the frequently applied simple arctan representation, i.e. $\theta = \arctan\left(\frac{u_y}{u_x}\right)$, since it provides the correct projection in view of the four quadrants of the Euclidean coordinate system and the spectrum $-\pi < \theta \leq \pi$. Concerning the anisotropic function γ we assume that $\gamma(\frac{\pi}{2}) = \gamma(-\frac{\pi}{2})$ and $\gamma(\pi) = \gamma(-\pi)$ which implies continuity of γ everywhere except for $u_x = u_y = 0$. Note that in this special case all the expressions where γ occur become zero anyway due to multiplication by u_x and u_y. Moreover we will require the interface energy to be only weakly anisotropic, i.e.

$$\gamma(\theta) + \gamma''(\theta) > 0, \tag{4}$$

for all $\theta \in [-\pi, \pi]$, to avoid ill-posedness of the resulting evolution equations. To be more precise, if $\gamma^2|\nabla u|^2$ is not convex then the term ∇u may be backwards diffusive for some initial data [30, 113] and in the two-dimensional case, which we consider here, this corresponds to the case if and only if $\gamma(\theta) + \gamma''(\theta) \leq 0$, which is referred to as strongly anisotropic.

Energy at the substrate

Finally we consider the energy a the solid substrate which is represented by the wall energy density

$$f_w(u) = \frac{\gamma_{VS} + \gamma_{FS}}{2} - \frac{u(3-u^2)}{4}(\gamma_{VS} - \gamma_{FS}), \tag{5}$$

as suggested in [50, 118]. As discussed in [42], it is convenient to choose f_w such that away from the contact line, f_w gives the vapor/substrate interfacial energy in the vapor phase, i.e. $f_w = \gamma_{VS}$, when $u = -1$, and the film/surface interfacial energy in the film phase, i.e. $f_w = \gamma_{FS}$, when $u = 1$. Moreover f_w has to satisfy $f_w'(\pm 1) = 0$, which provides that the energy minimizing solution of the free energy part, i.e. $\int_\Omega f_{FV}$, is undisturbed by f_w. Physically more meaningful expressions for the wall energy can be found in [93].

Variational derivative

Calculating the variational derivative of the energy function W^ϵ with respect to u, we then have

$$\begin{aligned}
\frac{\epsilon}{\lambda_m}\frac{d}{dt}W^\epsilon(u+tv)\big|_{t=0} &= \int_\Omega \left(F'(u)v + \epsilon^2 \left(\gamma \frac{\partial \gamma}{\partial \nabla u} |\nabla u|^2 + \gamma^2 \nabla u \right) \nabla v \right) \\
&\quad + \int_{\Gamma_w} \frac{\epsilon}{\lambda_m} f_w'(u) v \, ds \\
&= \int_\Omega \left(F'(u)v - \epsilon^2 \nabla \cdot \left(\gamma\gamma' \frac{\partial \theta}{\partial \nabla u} |\nabla u|^2 + \gamma^2 \nabla u \right) v \right) \\
&\quad + \int_{\Gamma_w} \left(\epsilon^2 \mathbf{n}_\Omega \cdot \left[\gamma \frac{\partial \gamma}{\partial \nabla u} |\nabla u|^2 + \gamma(\theta)^2 \nabla u \right] + \frac{\epsilon}{\lambda_m} f_w'(u) \right) v ds \\
&\quad + \int_{\partial\Omega \setminus \Gamma_w} \left(\epsilon^2 \mathbf{n}_\Omega \cdot \left[\gamma \frac{\partial \gamma}{\partial \nabla u} |\nabla u|^2 + \gamma(\theta)^2 \nabla u \right] \right) v ds,
\end{aligned} \tag{6}$$

where $\mathbf{n}_\Omega$ is the unit outward pointing normal vector onto Ω. Exploiting the particular representation of θ, i.e. (3), we find that

$$\frac{\partial \theta}{\partial u_x} = -\frac{u_y}{|\nabla u|^2} \qquad \text{and} \qquad \frac{\partial \theta}{\partial u_y} = \frac{u_x}{|\nabla u|^2}, \tag{7}$$

Natural boundary conditions

and imposing natural boundary conditions, i.e.

$$\epsilon \, \mathbf{n}_\Omega \cdot \left[\gamma(\theta)\gamma'(\theta) \begin{pmatrix} -u_y \\ u_x \end{pmatrix} + \gamma(\theta)^2 \nabla u \right] + \frac{f_w'}{\lambda_m} = 0 \tag{8}$$

on Γ_w, and

$$\mathbf{n}_\Omega \cdot \left[\gamma(\theta)\gamma'(\theta) \begin{pmatrix} -u_y \\ u_x \end{pmatrix} + \gamma(\theta)^2 \nabla u \right] = 0 \tag{9}$$

on $\partial\Omega \setminus \Gamma_w$, the variational derivative becomes

$$\frac{\epsilon}{\lambda_m}\frac{\delta W^\epsilon}{\delta u} = F'(u) - \epsilon^2 \nabla \cdot \left(\gamma\gamma' \begin{pmatrix} -u_y \\ u_x \end{pmatrix} + \gamma^2 \nabla u \right). \tag{10}$$

Mass flux and Fick's second law

We assume that the order parameter u is conserved and define the mass flux of u to be

$$\mathbf{j} = -m(u)\nabla \mu, \tag{11}$$

where the chemical potential μ is the variational derivative (10)

$$\mu(u) := F'(u) - \epsilon^2 \nabla \cdot \left(\gamma\gamma' \begin{pmatrix} -u_y \\ u_x \end{pmatrix} + \gamma^2 \nabla u \right) \tag{12}$$

and $m(u)$ is the diffusional mobility.

The anisotropic phase field model

Fick's second law then yields the anisotropic phase field model, which can be classified as anisotropic Cahn-Hilliard type equation

$$\begin{aligned} \partial_t u &= -\nabla \cdot \mathbf{j}, \\ \mathbf{j} &= -m(u)\nabla\mu, \\ \mu &= F'(u) - \epsilon^2 \nabla \cdot \left(\gamma\gamma' \begin{pmatrix} -u_y \\ u_x \end{pmatrix} + \gamma^2 \nabla u \right), \end{aligned} \tag{13a}$$

subject to the following boundary conditions

$$\begin{aligned} \epsilon\, \mathbf{n}_\Omega \cdot \left[\gamma(\theta)\gamma'(\theta) \begin{pmatrix} -u_y \\ u_x \end{pmatrix} + \gamma(\theta)^2 \nabla u \right] + \frac{f'_w}{\lambda_m} &= 0, \\ \mathbf{n}_\Omega \cdot (m(u)\nabla\mu) &= 0, \end{aligned} \tag{13b}$$

on Γ_w and

$$\mathbf{n}_\Omega \cdot \nabla u = 0, \qquad \mathbf{n}_\Omega \cdot (m(u)\nabla\mu) = 0, \tag{13c}$$

on $\partial\Omega \setminus \Gamma_w$. The former condition in each case is the natural boundary condition, according the variational derivative of the total energy, and the latter one corresponds to conservation of mass.

The anisotropic phase field model (13)-(13c) establishes the base of Part II, where a complete model formulation, regarding the particular choices for the homogeneous free energy $F(u)$ and mobility $m(u)$ is specified and motivated in Chapter 3.

2.2 THE ANISOTROPIC SHARP INTERFACE MODEL

Gibbs-Thomson relation

The anisotropic evolution of a one-dimensional film/vapor interface can alternatively be modeled as a type of surface-tracking problem which is driven by interfacial energy minimization. If we assume that surface diffusion is the only driving force, the increase in chemical potential per atom that is transferred from a point of zero curvature to a point of curvature κ is given by the well known anisotropic Gibbs-Thomson relation

$$\mu = \Omega \left(\gamma + \frac{\partial^2 \gamma}{\partial \theta^2} \right) \kappa, \tag{14}$$

where Ω is the atomic volume and γ is the anisotropic surface energy per unit area. The orientation of the surface is specified by the angle θ between the surface normal and the vertical axis. The average drift

velocity of surface atoms is derived from (14) by using the Nernst-Einstein equation, and reads

Nernst-Einstein equation

$$V = -\frac{D_s}{kT}\frac{\partial \mu}{\partial s}, \tag{15}$$

where D_s is the surface diffusion coefficient, kT is the thermal energy per atom, and s is the arc length along the surface. This drift velocity generates a surface current of atoms which is the product of V by the number of diffusing surface atoms per unit area ν

$$J = -\frac{D_s \nu}{kT}\frac{\partial \mu}{\partial s}. \tag{16}$$

If the surface divergence of $-J$ is taken, one obtains the increase in the number of atoms per unit area per unit time. This implies that (16) may be converted to the speed of movement v_n of the surface element along its normal

$$v_n = C\frac{\partial^2}{\partial s^2}\left[\left(\gamma + \frac{\partial^2 \gamma}{\partial \theta^2}\right)\kappa\right] \tag{17}$$

where $C = D_s \nu \Omega^2 / kT$. Note that the evolution of the fim profile $\mathbf{X} := (x(s,t), y(s,t))$ may then be written in the Lagrangian representation

$$\frac{\partial \mathbf{X}}{\partial t} = v_n \, \mathbf{n}, \tag{18}$$

where $\mathbf{n}$ is the interface outer unit normal vector. Equation (17) governs the motions of the particles on a one-dimensional surface and the corresponding boundary conditions at the substrate are derived in the next section.

2.2.1 *Derivation of the anisotropic boundary condition by the variational method*

Young-Herring contact angle condition

In addition to the anisotropic surface diffusion type of surface-tracking problem, we consider the feature of a moving contact line. More specifically, the contact line is a triple junction - where the film, substrate, and vapor phases meet- that migrates as the surface evolves. The boundary conditions at the triple junctions are the contact-point condition, zero mass flux condition and an anisotropic contact angle boundary condition, referred to as Young-Herring condition. Herring [46] originally derived this condition for the interception point of up to three interfaces by the method of virtual displacement. We now present a variational derivation of the anisotropic contact angle condition at the moving boundary. This method has previously been adapted by Mullins [82] and Min et al. [78] in view of the anisotropic surface diffusion dewetting problem and the main steps of the following derivation can also be reviewed in Appendix D in [78].

Literature referring to the method

Consider a two-dimensional solid film on a straight substrate and in equilibrium with vapor. This implies that the total free energy of

Minimizing the total free energy

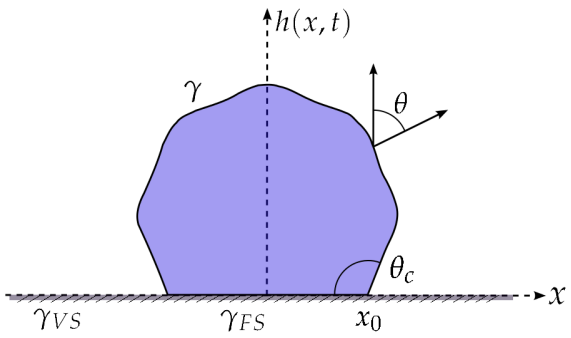

Figure 6: Sketch of a two- dimensional solid film on a substrate.

the system is at a minimum and its variation is zero

$$\delta \int_{x_l}^{x_r} \left[\gamma(\theta) \sqrt{1 + h_x^2} + \gamma_{FS} - \gamma_{VS} + \lambda h \right] dx = 0, \tag{19}$$

where δ represents the variation, $h = h(x,t)$ is the film height with spacial derivative $h_x = \partial h / \partial x$, $\gamma = \gamma(h_x)$ is the anisotropic interface energy between film and vapor depending on the angle h_x, γ_{FS} and γ_{VS} are the film/substrate and vapor/substrate surface energies per unit area, respectively, and x_l and x_r are the moving contact points. The first term in the integral represents the surface energy of the film/vapor interface and the second and third terms represent the surface energy at the solid substrate. Conservation of mass is imposed by a Lagrange multiplier λ. Calculating the variational derivative [19], we obtain

Variational derivative

$$\begin{aligned} 0 = &\int_{x_l}^{x_r} \lambda \delta h dx + \int_{x_l}^{x_r} \left[(1 + h_x^2)^{1/2} \frac{d\gamma}{dh_x} + \frac{\gamma h_x}{(1 + h_x^2)^{1/2}} \right] \delta h_x dx \\ &+ \left[\gamma (1 + h_x^2)^{1/2} + \gamma_{FS} - \gamma_{VS} \right]_{x = x_r} \delta x_r \\ &- \left[\gamma (1 + h_x^2)^{1/2} + \gamma_{FS} - \gamma_{VS} \right]_{x = x_l} \delta x_l. \end{aligned} \tag{20}$$

Since $\delta h_x = d(\delta h)/dx$, integration by parts of the second integral gives

$$\begin{aligned} &\int_{x_l}^{x_r} \left[(1 + h_x^2)^{1/2} \frac{d\gamma}{dh_x} + \frac{\gamma h_x}{(1 + h_x^2)^{1/2}} \right] \delta h_x dx \\ &= \left[\left((1 + h_x^2)^{1/2} \frac{d\gamma}{dh_x} + \frac{\gamma h_x}{(1 + h_x^2)^{1/2}} \right) \delta h \right]_{x = x_l}^{x = x_r} \\ &\quad - \int_{x_l}^{x_r} \left[(1 + h_x^2)^{1/2} h_{xx} \frac{d^2\gamma}{dh_x^2} + \frac{2 h_x h_{xx}}{(1 + h_x^2)^{1/2}} \frac{d\gamma}{dh_x} + \frac{\gamma h_{xx}}{(1 + h_x^2)^{3/2}} \right] \delta h dx. \end{aligned} \tag{21}$$

Exploiting this in (20) and invoking $\delta h|_{x=x_l} = -h_x|_{x=x_l}\delta x_l$ and $\delta h|_{x=x_r} = -h_x|_{x=x_r}\delta x_r$, we find

$$\begin{aligned} 0 = \int_{x_l}^{x_r} & \left[\lambda - (1+h_x^2)^{1/2} h_{xx} \frac{d^2\gamma}{dh_x^2} - \frac{2h_x h_{xx}}{(1+h_x^2)^{1/2}} \frac{d\gamma}{dh_x} - \frac{\gamma h_{xx}}{(1+h_x^2)^{3/2}}\right] \delta h \\ & + \left[\frac{\gamma}{(1+h_x^2)^{1/2}} + \gamma_{FS} - \gamma_{VS} - h_x(1+h_x^2)^{1/2}\frac{d\gamma}{dh_x}\right]_{x=x_r} \delta x_r \\ & - \left[\frac{\gamma}{(1+h_x^2)^{1/2}} + \gamma_{FS} - \gamma_{VS} - h_x(1+h_x^2)^{1/2}\frac{d\gamma}{dh_x}\right]_{x=x_l} \delta x_l. \end{aligned} \tag{22}$$

Three equilibrium conditions

Realizing that δh is arbitrary, the above equation yields three equilibrium conditions. The first one reads

$$\lambda = \frac{\gamma h_{xx}}{(1+h_x^2)^{3/2}} + (1+h_x^2)^{1/2} h_{xx} \frac{d^2\gamma}{dh_x^2} + \frac{2h_x h_{xx}}{(1+h_x^2)^{1/2}} \frac{d\gamma}{dh_x}. \tag{23}$$

Introducing the surface normal angle θ, which is the angle between the film surface normal and the vertical axis, (Fig. 6) yields

$$\tan\theta = h_x, \tag{24}$$

and consequently

$$\frac{\partial\gamma}{\partial\theta} = (1+h_x^2)\frac{d\gamma}{dh_x}, \tag{25}$$

$$\frac{\partial^2\gamma}{\partial\theta^2} = 2h_x(1+h_x^2)\frac{d\gamma}{dh_x} + (1+h_x^2)^2\frac{d^2\gamma}{dh_x^2}. \tag{26}$$

condition (23) may be rewritten as

$$\lambda = -\left(\gamma + \frac{d^2\gamma}{d\theta^2}\right)\kappa, \tag{27}$$

where we also exploited that

$$\kappa = -\frac{h_{xx}}{(1+h_x^2)^{3/2}}. \tag{28}$$

With the Lagrange multiplier $\lambda = -\mu/\Omega$ equation (27) is recognized as the anisotropic Gibbs-Thomson relation as presented in (14). The other two equilibrium conditions yield the boundary conditions at $x = x_l$ and $x = x_r$, respectively. Since this condition turns out to be equal for x_l and x_r we can write it in a generalized form for a contact point x_0, which corresponds to x_l or x_r respectively. The equilibrium condition

$$\frac{\gamma}{(1+h_x^2)^{1/2}} + \gamma_{FS} - \gamma_{VS} - h_x(1+h_x^2)^{1/2}\frac{d\gamma}{dh_x} = 0 \tag{29}$$

then becomes

$$\gamma(\theta_c)\cos\theta_c - \gamma'(\theta_c)\sin\theta_c + \gamma_{FS} - \gamma_{VS} = 0, \tag{30}$$

where $\gamma' = d\gamma/d\theta$ and θ_c denotes the equilibrium contact angle, which is equal to θ at $x = x_0$. This surface energy minimizing contact angle boundary condition is referred to as Young-Herring condition [78] and if the surface energy is isotropic, i.e. $\gamma \equiv const.$ equation (30) reduces to the well known Young's condition.

Young-Herring condition

The anisotropic sharp interface model

The full anisotropic sharp interface model which describes the anisotropic evolution due to surface diffusion then reads

$$v_n = C\frac{\partial^2}{\partial s^2}\left[\left(\gamma + \frac{\partial^2\gamma}{\partial\theta^2}\right)\kappa\right], \tag{31a}$$

with the contact point condition

$$h(x_0, t) = 0, \tag{31b}$$

contact angle condition

$$\left[\gamma(\theta_c)\cos\theta_c - \gamma'(\theta_0)\sin\theta_c\right]_{x=x_0} + \gamma_{FS} - \gamma_{VS} = 0, \tag{31c}$$

and zero mass flux condition

$$\frac{\partial}{\partial s}\left[\left(\gamma + \frac{\partial^2\gamma}{\partial\theta^2}\right)\kappa\right]\Big|_{x=x_0} = 0, \tag{31d}$$

where $x_0 \in \{x_l, x_r\}$. Note that the determination of x_l and x_r is part of the problem, which implies that all of the boundary conditions are necessary and the problem is well-posed.

2.2.2 *Nondimensional Problem*

Introducing suitable scalings

In order to nondimensionalize the equations (31a)- (31d), let H_0 be the characteristic length scale corresponding to the unperturbed film height and let γ_0 be the scale for the film/vapor interface. Rescaling according to

$$\begin{aligned} t = \frac{H_0^4}{C\gamma_0}\tilde{t}, \quad x = H_0\tilde{x}, \quad h = H_0\,\tilde{h}, \quad s = H_0\tilde{s}, \\ \kappa = H_0\tilde{\kappa}, \quad \gamma = \gamma_0\tilde{\gamma}, \quad v_n = \frac{C\gamma_0}{H_0^3}\tilde{v}_n \end{aligned} \tag{32}$$

then leads to the dimensionless form

$$v_n = \frac{\partial^2}{\partial s^2}\left[\left(\gamma + \frac{\partial^2\gamma}{\partial\theta^2}\right)\kappa\right], \tag{33a}$$

with the contact point condition

$$h(x_0, t) = 0, \tag{33b}$$

contact angle condition

$$\left[\gamma(\theta_c)\cos\theta_c - \gamma'(\theta_0)\sin\theta_c\right]_{x=x_0} + \frac{\gamma_{FS}-\gamma_{VS}}{\gamma_0} = 0, \tag{33c}$$

and zero mass flux condition

$$\frac{\partial}{\partial s}\left[\left(\gamma + \frac{\partial^2\gamma}{\partial\theta^2}\right)\kappa\right]\Big|_{x=x_0} = 0, \tag{33d}$$

where $x_0 \in \{x_l, x_r\}$ and x_l, x_r denote the positions of the left and right contact points, respectively, in the rescaled system. Note that $v_n, s, \gamma, \kappa, h$, and t are dimensionless variables, and we still used the same notations for brevity.

The present sharp interface model will be relevant in Chapter 3 as it is the desired limit model of the previously introduced anisotropic phase field model. Moreover we will consider the corresponding small slope approximation in Part III which is introduced in the next section.

2.3 THE SMALL SLOPE APPROXIMATION

A significant model reduction

A basic property of the thin solid films which we consider here is that the characteristic height scale of the initial film is much smaller than the length scale. Under the additional assumption that the present slopes are small, we are able to reduce the sharp interface model to a particular case of the so-called thin film equations. This significant model reduction does not only simplify the numerical simulation, but also enables to systematically study some of the characteristic dewetting properties such as the dewetting rate or fingering instabilities of the dewetting front.

Lubrication approximation for thin liquid films

In order to stay consistent with the previous model derivations we consider a model for solid state dewetting in one space dimension. In addition we will confine ourselves to the isotropic case during the derivation. Note that the class of thin film equations which will be considered in Part III is more general and the most common derivation of this whole class of models is via a lubrication approximation of the Navier-Stokes equations for thin film viscous flows. However, since lubrication theory refers to thin liquid films, which are not the focus of this work, we skip the corresponding general derivation and present the approach which corresponds to solid films instead.

Transformation to Cartesian coordinates

We begin by demonstrating the transformation (33a)-(33d) into Cartesian coordinates which enables to apply the small slope approximation. Observing that the transformation in curvilinear coordinates is based on the parametrization of the one-dimensional surface

$$\vec{\Gamma}(\mathbf{x}) := \begin{pmatrix} x \\ h(x) \end{pmatrix} \tag{34}$$

and the basis vectors

$$\vec{s} := \frac{1}{\sqrt{1+h_x^2}}\begin{pmatrix}1\\ h_x\end{pmatrix}, \qquad \vec{n} := \frac{1}{\sqrt{1+h_x^2}}\begin{pmatrix}-h_x\\ 1\end{pmatrix} \tag{35}$$

we have the transformation rule

$$\begin{pmatrix}dx\\ dh\end{pmatrix} = \frac{1}{\sqrt{1+h_x^2}}\begin{pmatrix}1 & -h_x\\ h_x & 1\end{pmatrix}\begin{pmatrix}ds\\ dn\end{pmatrix}. \tag{36}$$

This reveals that the surface derivative of an arbitrary function $\Psi(x)$ depending on x reads

$$\frac{\partial \Psi}{\partial s} = \frac{1}{\sqrt{1+h_x^2}}\frac{\partial \Psi}{\partial x}. \tag{37}$$

Considering (33a) and using the definition (28), we then obtain

$$v_n = -\frac{1}{\sqrt{1+h_x^2}}\left[\frac{\partial}{\partial x}\frac{1}{\sqrt{1+h_x^2}}\frac{\partial}{\partial x}\left(\left(\gamma+\frac{\partial^2\gamma}{\partial\theta^2}\right)\frac{h_{xx}}{(1+h_x^2)^{3/2}}\right)\right], \tag{38}$$

which is still valid for arbitrary slopes. A simple geometrical projection of the velocity dh/dt gives the relation

$$v_n = \frac{1}{\sqrt{1+h_x^2}}\frac{dh}{dt}. \tag{39}$$

Small slope approximation

We are now in the position to apply the small slope approximation, i.e. we assume that $|h_x| \ll 1$. Note that, according to (3), this assumption also implies $\theta \approx \pi/2$ and consequently it also makes sense to assume that surface energy is isotropic, i.e. $\gamma \equiv 1$.

Applying the small slope approximation, the isotropic sharp interface model for surface diffusion dewetting reads

$$\frac{dh}{dt} = -C\,\partial_{xxxx}h, \tag{40a}$$

with the contact point condition

$$h(x_0,t) = 0, \tag{40b}$$

contact angle condition

$$h_x\big|_{x=x_0} = \theta_c, \tag{40c}$$

and zero mass flux condition

$$\partial_{xxx}h\big|_{x=x_0} = 0, \tag{40d}$$

where x_0 corresponds to x_l or x_r, respectively and $\theta_c < 1$. Note that again the determination of x_l and x_r is part of the problem, which implies that all of the boundary conditions are necessary and the

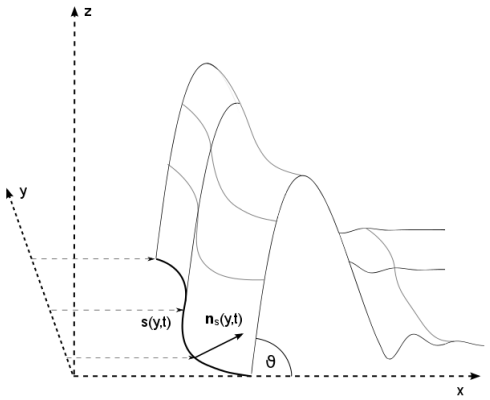

Figure 7: A sketch of a retracting rim with a sinusoidal perturbation in the spanwise (y-) direction.

problem is well-posed.

Notes on the two-dimensional case

Note that the thin film model which will be investigated in Part III refers to two space dimensions and the corresponding small slope approximation reads

$$\frac{dh}{dt} = -\Delta^2 h \tag{41a}$$

with boundary conditions

$$h = 0\,, \qquad x = s(y,t) \tag{41b}$$

$$\nabla h \cdot \mathbf{n}_s = \theta\,, \qquad x = s(y,t) \tag{41c}$$

$$h^n \left(\nabla \Delta h \cdot \mathbf{n}_s\right) = 0\,, \qquad x = s(y,t) \tag{41d}$$

where $x = s(y,t)$ is the position of the two-dimensional contact line. Moreover, assuming that the initial film height is small compared to the film length and scaling the height of the unperturbed film to $h \equiv 1$, suggests to replace the boundary conditions on the right hand side by the far field condition

$$\lim_{x\to\infty} h \equiv 1, \tag{42}$$

as shown in Figure 7. The model domain will consequently be replaced by $\Omega = \{(x,y);\, s(y,t) < x < L,\ -\infty < y < \infty\}$.

Part II

THE PHASE FIELD MODEL

3

SHARP INTERFACE LIMITS OF THE ANISOTROPIC PHASE FIELD MODEL

3.1 THE DIFFICULTY OF MODELING ANISOTROPIC SURFACE DIFFUSION CORRECTLY

Completing the model derivation

Considering the anisotropic phase field model which we derived in Chapter 2.1, the question naturally arises for which particular choices of mobility and bulk free energy motion by pure surface diffusion is recovered in the sharp interface limit. For an introduction to phase field modeling of microstructure evolution and a general motivation of modeling choices we refer to the review by Moelans et al. [87]. Since establishing the correspondence between phase field and sharp interface models has been investigated intensively during the last decades, we start this chapter with an overview of related models and their sharp interface derivations.

First sharp interface derivations

One of the first systematic derivations of sharp interface models using matched asymptotic expansions has been carried out by Pego [92]. His analysis concerned the Cahn-Hilliard equation

$$\partial_t u = -\nabla \cdot \mathbf{j}, \qquad \mathbf{j} = -m(u)\nabla\mu, \qquad \mu = F'(u) - \epsilon^2 \Delta u, \tag{43}$$

with the homogeneous free energy $F(u) = \frac{1}{2}(1-u^2)^2$ and constant mobility $m(u) = 1$ together with the no-flux boundary condition $\mathbf{j} \cdot \mathbf{n} = 0$. For this model Pego has shown that the sharp interface limit $\epsilon \to 0$ reduces to the so-called Mullins-Sekerka problem [83] on a long time scale $t = O(\varepsilon^{-1})$, which corresponds to interface motion by pure bulk diffusion.

Motivating F and m

The particular choice for $F(u) = \frac{1}{2}(1-u^2)^2$ and $m(u) = 1$ is actually an approximation of the Cahn-Hilliard equation as derived in [89] with the concentration dependent degenerate mobility $m(u) = 1 - u^2$ and the logarithmic free energy

$$F(u) = \frac{T}{2}((1+u)\ln(1+u) + (1-u)\ln(1-u)) + \frac{1}{2}(1-u^2)^2 \tag{44}$$

in the limit $T \to 1$, where T is the temperature. A concentration dependent degenerate mobility appears reasonable according to the original derivation of the Cahn-Hilliard equation [17], and the logarithmic terms in the homogeneous free energy (44) arise from entropic contributions. The sharp interface asymptotic analysis for this case has been considered by Cahn et al. [15]. For the deep quench limit, $T = 0$, and for $T = O(\varepsilon^\alpha)$ with $\alpha > 0$, Cahn et al. show that the equation (43) reduces to the so-called Mullins' model [81] in the sharp interface

limit $\varepsilon \to 0$, which is a model for surface diffusion. Note that in the isotropic case this corresponds to the normal velocity of the interface being proportional to the surface Laplacian of the mean curvature. However, the complicated logarithmic representation (44) seems rather inconvenient in view of analysis and numerical simulation.

Inconsistencies in sharp interface derivations

Phase field models combining other approximations of the bulk free energy and the mobility have frequently been investigated as candidates for sharp interface models driven by surface diffusion in the limit $\varepsilon \to 0$, and popular examples are the polynomial free energy $F(u) = \frac{1}{2}(1-u^2)^2$ combined with the degenerate mobility $m(u) = 1-u^2$ or with the bi-quadratic degenerate mobility $m(u) = (1-u^2)^2$, referring to the studies [52, 101]. However, as has been pointed out by Guggenberger et al. [40] and more recently by Dai et al. [22, 23] the standard matched asymptotic derivations that recover Mullins' model with pure surface diffusion lead to inconsistencies that appear in the asymptotic derivations except when the interface is flat. Indeed, in Lee et al. [64] it was shown that for the combination $F(u) = \frac{1}{2}(1-u^2)^2$ and $m(u) = 1-u^2$ a careful asymptotic analysis involving multiple inner layers and exponential asymptotic expansions is necessary in order to resolve this problem. The result is a sharp interface model where bulk diffusion contributes to the interfacial mass flux at the same order in ε as surface diffusion. This implies that the phase field model describes a different driving mechanism for the interface evolution than intended, i.e. than in Mullins' model.

The isotropic phase field model proposed by Jiang et al.

Such is the case for the isotropic phase field model proposed by Jiang et al. [52] with a phase field variable $u = u(\mathbf{x}, t)$ that is defined on the domain Ω and where $u(\mathbf{x}, t) > 0$ characterizes the film phase, $u(\mathbf{x}, t) < 0$ the vapor phase and $u(\mathbf{x}, t) = 0$ the location of the interface. For this phase field variable the total free energy

$$W^\epsilon = \int_\Omega f_{FV}\, d\Omega + \int_{\Gamma_w} f_w\, d\Gamma, \tag{45}$$

combines a bulk contribution from the Ginzburg-Landau free energy density

$$f_{FV} = \lambda_m \left(F(u) + \frac{\varepsilon^2}{2} |\nabla u| \right), \tag{46}$$

with a surface energy density contribution from the wall $\Gamma_w \subset \partial\Omega$,

$$f_w = \frac{\gamma_{VS} + \gamma_{FS}}{2} - \frac{u(3-u^2)}{4}(\gamma_{VS} - \gamma_{FS}). \tag{47}$$

The width of the diffuse interface layer is denoted by ϵ, λ_m denotes the mixing energy density and γ_{VS} and γ_{FS} the vapor/substrate and film/substrate interface energy densities, respectively. A derivation via the first variational derivative of the total free energy functional

with respect to u, following the derivation proposed in Chapter 2.1, yields the corresponding chemical potential $\mu = (1/\lambda_m)\delta W^\epsilon/\delta u$, so that by making use of the fact that u is a conserved order parameter, the Cahn-Hilliard equation (43) is obtained together with a no-flux boundary condition on $\partial\Omega$. Note that this model so far is very similar to our first model derivation in Chapter 2.1, except that it does not include anisotropic surface energies. In Jiang et al. [52] the mobility and homogeneous free energy are then chosen to be $m(u) = 1 - u^2$ and $F(u) = \frac{1}{2}(1-u^2)^2$, respectively, which was suggested to correspond to the sharp-interface model for pure surface diffusion. However, as already mentioned before and shown in [64] the asymptotic limit does not yield this result.

Choosing an appropriate mobility

Realizing that the degeneracy of the mobility at the pure phases suppresses the mass flux in the normal direction and therefore the diffusion from or into the bulk and that a higher order of degeneracy increases this effect, we suggest the mobility of form $m(u) = (1-u^2)^2$ together with the same homogeneous free energy as in the reference [52], i.e. $F(u) = \frac{1}{2}(1-u^2)^2$. Note that in [64] it is also pointed out that this combination is a suitable candidate in order to recover motion by pure surface diffusion in the sharp interface limit.

Including anisotropies

In addition, the phase field model considered here includes an anisotropic surface energy $\gamma(\theta)$, where θ is the interface orientation angle. We note that anisotropic surface energy may lead to an ill-posed problem when there are missing orientations in the corresponding Wulff shape. To be more precise, if $\gamma^2|\nabla u|^2$ is not convex then the term ∇u may be backwards diffusive for some initial data [30, 113]. In particular, in the two-dimensional case which we consider here, ∇u is backwards diffusive if and only if $\gamma(\theta) + \gamma''(\theta) < 0$. This case is referred to as strongly anisotropic and has been investigated by Cahn and Taylor [18], Eggleston et al. [30], suggesting various convexification schemes and has been numerically treated for example by Wise et al. [113] to solve the regularized, anisotropic Cahn-Hilliard equation.

For weak anisotropy different Cahn-Hilliard models were studied by McFadden et al. [77] and Rätz et al. [94], where in both cases the method of matched asymptotic expansions is used to recover the appropriate anisotropic form of the Gibbs-Thomson equation in the sharp interface limit.

Boundary conditions at the solid boundary

Furthermore we incorporate the sharp interface limit towards adequate anisotropic boundary conditions at the triple junction where film, vapor and substrate meet. Other studies that deal with the boundary conditions at triple junctions have considered the isotropic Cahn-Hilliard equation [88], or a system of isotropic Cahn-Hilliard equations [37], where the ideas of [11] are adapted in order to show that in the

asymptotic limit the boundary condition leads to Young's law at triple junctions [116], i.e.

$$\gamma_{VS} - \gamma_{FS} = \gamma_{FV} \cos\theta_c, \tag{48}$$

where γ_{VS}, γ_{FS} and γ_{FV} are the interface energy densities describing the interfaces between vapor/substrate, film/substrate, and film/vapor, respectively, and θ_c is the equilibrium contact angle. Of particular interest in our study is the technique as well as the geometry presented in [90], in order to study the asymptotic behavior at the three phase contact line of our problem.

Previously done studies on anisotropies in phase field models

As mentioned above, anisotropies in phase field models and in particular their sharp interface limit [36, 77, 94] as well as boundary conditions at triple junctions [11, 37, 88, 90] have been discussed in the literature. Nevertheless, to the best of our knowledge, there is no work investigating an anisotropic phase field model together with boundary conditions at solid boundaries. Furthermore, for the particular choice of free energy F and mobility m in this work, the sharp interface limit via matched asymptotic analysis was not studied so far, which is also a topic of particular interest, since the frequently applied models show an apparent inconsistency in view of motion by pure surface diffusion as pointed out in [40] and [64].

Overview of this chapter

The chapter is organized as follows. In section 3.3 we derive the sharp interface limit in the weakly anisotropic case and inside the model domain which confirms the approach of surface diffusion for the present choice of mobility m and free energy F. In section 3.4 we deal with the corresponding boundary condition at the solid boundary and apply an appropriate asymptotic method in order to derive the anisotropic contact angle boundary condition.

3.2 MODEL FORMULATION

Recalling the model as introduced in Chapter 2.1, we will in the following consider

$$\begin{aligned} \partial_t u &= \nabla \cdot \mathbf{j}, \\ \mathbf{j} &= m(u)\nabla\mu, \\ \mu &= F'(u) - \epsilon^2 \nabla \cdot \left(\gamma\gamma' \begin{pmatrix} -u_y \\ u_x \end{pmatrix} + \gamma^2 \nabla u \right), \end{aligned} \tag{49a}$$

subject to the conditions

$$\begin{aligned} \epsilon\, \mathbf{n}_\Omega \cdot \left[\gamma(\theta)\gamma'(\theta) \begin{pmatrix} -u_y \\ u_x \end{pmatrix} + \gamma(\theta)^2 \nabla u \right] + \frac{f_w'}{\lambda_m} &= 0, \\ \mathbf{n}_\Omega \cdot (m(u)\nabla\mu) &= 0, \end{aligned} \tag{49b}$$

on Γ_w, where f_w is given by (47) and

$$\mathbf{n}_\Omega \cdot \nabla u = 0, \qquad \mathbf{n}_\Omega \cdot (m(u)\nabla\mu) = 0, \tag{49c}$$

on $\partial\Omega \setminus \Gamma_w$. Note that in the original derivation in Chapter 2.1 we had, due to the definition of the flux, minus signs in front of the first two equations in (49). However, since the formulation without the minus signs is equivalent from a mathematical point of view, we choose this representation for the sake of simplification.

Motivated by the previous section we consider the homogeneous free energy

$$F(u) = \frac{1}{2}(1-u^2)^2 \tag{50}$$

and the bi-quadratic diffusional mobility $m(u)$

$$m(u) = \left(1-u^2\right)^2. \tag{51}$$

Moreover, in order to guarantee well-posedness of the problem, we limit ourselves to anisotropic surface energies which are weak anisotropic, i.e. which fulfill

$$0 \leq \gamma(\theta) + \gamma''(\theta). \tag{52}$$

3.3 SHARP INTERFACE LIMIT FROM MATCHED ASYMPTOTIC EXPANSIONS

Rescaling the time variable

In this section we will use the method of matched asymptotic expansions in order to study the long time behavior of (49) in the limit $\epsilon \to 0$ and capture the contribution from surface diffusion. Observing that the evolution of the order parameter occurs at an $O(1/\epsilon^2)$ time scale (see [64]), we suggest to rescale time via $\tau = \epsilon^2 t$, so that (49) reads

$$\begin{aligned} \epsilon^2 \partial_\tau u &= \nabla \cdot \mathbf{j}, \\ \mathbf{j} &= m(u)\nabla\mu, \\ \mu &= F'(u) - \epsilon^2 \nabla \cdot \left(\gamma\gamma' \begin{pmatrix} -u_y \\ u_x \end{pmatrix} + \gamma^2 \nabla u\right), \end{aligned} \tag{53}$$

with mobility $m(u)$ defined by (51) and free energy $F(u)$ defined by (50) and boundary conditions (49b) and (49c).

3.3.1 *Sharp interface dynamics away from the solid boundary*

Existing works and how they differ from our approach

We first study the asymptotic behavior of the solution in the outer region and the inner interface region away from the solid substrate i.e. $y \gg \epsilon$. The method of matched asymptotic expansions for anisotropic sharp interface limits has already been applied in [77] and [36] in order to recover the appropriate anisotropic sharp interface form of an anisotropic Allen-Cahn-type equation. In [36] it is in addition pointed out how the analysis has to be modified when considering the Cahn-Hilliard system or the related minimum problem. The Cahn-Hilliard case was also studied in [94] where a connection between

sharp interface models for isotropic and anisotropic surface evolution and their diffuse interface counterparts is given. In contrast to our work, [94] as well as [36] also consider different driving forces such as deposition flux and elastic stress in the diffuse interface model, which induce that the evolution in the sharp interface limit is not only driven by surface diffusion. In this section we will present a matched asymptotic analysis for the anisotropic Cahn-Hilliard equation (53) with the aim to recover pure surface diffusion in the sharp interface limit. As shown in [64] this is already in the isotropic case a non-trivial topic and we will exploit this knowledge as well as the particular asymptotic method presented in [64] in order to verify the sharp interface limit in our case.

3.3.2 *Outer problem*

The equations (53) are already stated in outer variables. For the outer expansions, we will use

$$\begin{aligned} u &= u_0 + \epsilon u_1 + \epsilon^2 u_2 ..., \\ \mu &= \mu_0 + \epsilon \mu_1 + \epsilon^2 \mu_2 ..., \\ \mathbf{j} &= \mathbf{j}_0 + \epsilon \mathbf{j}_1 + \epsilon^2 \mathbf{j}_2 .... \end{aligned} \tag{54}$$

which suggests the following expansions for $M(u)$ and $F(u)$

$$\begin{aligned} m(u) &= m(u_0) + \epsilon m'(u_0) u_1 + \epsilon^2 \left(\frac{1}{2} m''(u_0) u_1^2 + m'(u_0) u_2 \right) ... \\ F'(u) &= F'(u_0) + \epsilon F''(u_0) u_1 + \epsilon^2 \left(\frac{1}{2} F'''(u_0) u_1^2 + F''(u_0) u_2 \right) ... \end{aligned}$$

As we consider the sharp interface dynamics away from the solid boundary we only impose the boundary condition

$$\mathbf{n}_\Omega \cdot \nabla u = 0, \qquad \mathbf{n}_\Omega \cdot (m(u) \nabla \mu) = 0, \tag{55}$$

on $\partial\Omega \setminus \Gamma_w$.

3.3.3 *Inner problem*

Introducing curvilinear coordinates

Considering the inner expansion about the interface, it is convenient to pass to curvilinear coordinates, and work in local coordinates in the asymptotic expansion.

Transformation to inner variables

Similar as in [64, 92], we define the inner layer in a coordinate system relative to the interface

$$\mathbf{x} = \mathbf{R}(s, \tau) + \epsilon \rho \, \mathbf{n}(s, \tau), \tag{56}$$

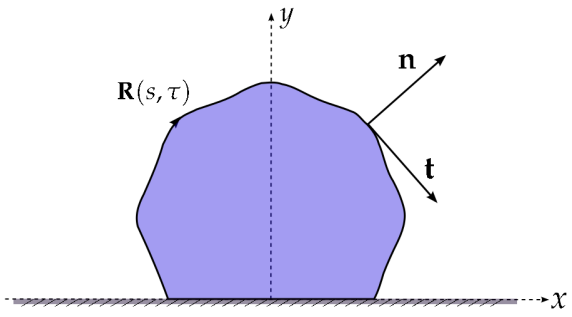

Figure 8: Sketch of the solid-vapor interface showing the orientation of the curvilinear coordinate system.

and let $U(s,\rho,\tau) = u(\mathbf{x},t)$, $M(s,\rho,\tau) = \mu(\mathbf{x},t)$ and $\mathbf{J}(s,\rho,\tau) = \mathbf{j}(\mathbf{x},t)$. Here, $\mathbf{R} := (R_1, R_2)^T$ is the position of the interface defined by

$$u(\mathbf{R},t) = 0, \tag{57}$$

s is the arclength and $\mathbf{n} = (n_1, n_2)^T$ is the unit normal to the solid-vapor interface oriented such that it points out of the solid. The orientation of the unit tangent $\mathbf{t} = (t_1, t_2)^T$ and of the corresponding arclength parametrization of R are chosen so that $(\mathbf{t}, \mathbf{n})$ forms a right-handed system, i.e. $\mathbf{t} = (n_2, -n_1)^T$, thus the solid always lies to the right of the curve and we have the relation

$$\mathbf{t} = \partial_s \mathbf{R}. \tag{58}$$

The sign of the curvature κ is defined so that the normal and tangent unit vectors satisfy the Frenet-Serret formulae in the form

Frenet-Serret formulae

$$\partial_s \mathbf{t} = -\kappa \mathbf{n}, \qquad \partial_s \mathbf{n} = \kappa \mathbf{t} \tag{59}$$

This choice implies that $\kappa > 0$, if the curve is convex with respect to the solid. Calculating the partial derivatives of $\mathbf{x}(s,\rho)$ we obtain the basis of the coordinate transform

$$\mathbf{e}_s := \frac{\partial \mathbf{x}}{\partial s} = (1 + \epsilon\rho\kappa)\mathbf{t}, \qquad \mathbf{e}_\rho := \frac{\partial \mathbf{x}}{\partial \rho} = \epsilon \mathbf{n} \tag{60}$$

where we exploited (58) and (59). Thus the corresponding metric tensor reads

$$(g_{\alpha\beta}) = \underline{g} := \begin{pmatrix} 1 & 0 \\ 0 & (1+\epsilon\rho\kappa)^2 \end{pmatrix}, \tag{61}$$

where the elements of the tensor are given by $g_{\alpha\beta} = \mathbf{e}_\alpha \cdot \mathbf{e}_\beta$. The determinant is

$$g := \det \underline{g} = (1 + \epsilon\rho\kappa)^2 \tag{62}$$

and the corresponding contravariant components of the metric tensor are given by

$$(g^{\alpha\beta}) = \underline{g}^{-1} := \begin{pmatrix} 1 & 0 \\ 0 & (1+\epsilon\rho\kappa)^{-2} \end{pmatrix}. \tag{63}$$

Using the summation convention from now on, we can write vectors in the reciprocal basis. Exploiting the index contraction rule $\mathbf{e}^\alpha = g^{\alpha\beta}\mathbf{e}_\beta$, we obtain

$$\mathbf{e}^s := \epsilon^{-1}\mathbf{n}, \qquad \mathbf{e}^\rho := \frac{1}{1+\epsilon\rho\kappa}\mathbf{t} \tag{64}$$

Differential operators in curvilinear coordinates

which reveals that the gradient operator in these curvilinear coordinates reads

$$\nabla = \mathbf{e}^\alpha \partial_\alpha = \mathbf{n}\epsilon^{-1}\partial_\rho + \frac{1}{1+\epsilon\rho\kappa}\mathbf{t}\partial_s, \tag{65}$$

From tensor analysis we know that the divergence operator of a vector field $\mathbf{A}$ is defined to be

$$\begin{aligned}\nabla\mathbf{A} &= \frac{1}{\sqrt{g}}\partial_\alpha\left(\sqrt{g}A^\alpha\right)\\ &= \frac{1}{\sqrt{g}}\partial_\alpha\left(\sqrt{g}g^{\alpha\beta}A_\beta\right)\\ &= \frac{1}{1+\epsilon\rho\kappa}\left[\epsilon^{-1}\partial_\rho\big((1+\epsilon\rho\kappa)A_\rho\big) + \partial_s\left(\frac{1}{1+\epsilon\rho\kappa}A_s\right)\right].\end{aligned} \tag{66}$$

The Laplacian in inner coordinates becomes

$$\begin{aligned}\Delta u &= \nabla\cdot(\nabla u)\\ &= \frac{1}{\epsilon^2}\frac{1}{1+\epsilon\rho\kappa}\partial_\rho\left((1+\epsilon\rho\kappa)\partial_\rho u\right) + \frac{1}{1+\epsilon\rho\kappa}\left(\frac{1}{1+\epsilon\rho\kappa}\partial_s u\right)\end{aligned} \tag{67}$$

and expanding in orders of ϵ reveals

$$\begin{aligned}\Delta u =&(\epsilon^{-2}\partial_{\rho\rho} + \epsilon^{-1}\kappa\partial_\rho + \partial_{ss} - \rho\kappa^2\partial_\rho + \epsilon^2(\rho^2\kappa^3\partial_\rho - \rho\kappa\partial_s - \partial_s\rho\kappa\partial_s))u\\ &+ O(\epsilon^2)u.\end{aligned} \tag{68}$$

Inner expansions

Inner expansions for the main variables

For the inner expansions, we will use

$$\begin{aligned}U &= U_0 + \epsilon U_1 + \epsilon^2 U_2 ...,\\ M &= M_0 + \epsilon M_1 + \epsilon^2 M_2 ...,\\ \mathbf{J} &= \epsilon^{-1}\mathbf{J}_{-1} + \mathbf{J}_0 + \epsilon\mathbf{J}_1 + \epsilon^2\mathbf{J}_2 ....\end{aligned} \tag{69}$$

where the reason why the asymptotic expansion for $\mathbf{J}$ starts at order ϵ^{-1} will become clear in the following. Moreover we will apply

$$F'(U) = F'(U_0) + \epsilon F''(U_0)U_1 ... \tag{70}$$

and introduce expansions for θ and γ respectively, as these are relevant for the first three orders of the inner problem

$$\begin{aligned}\theta &= \theta_0 + \epsilon\theta_1 + \epsilon^2\theta_2 ...,\\ \gamma &= \gamma(\theta_0) + \epsilon\gamma'(\theta_0)\theta_1 + \epsilon^2\left(\frac{1}{2}\gamma''(\theta_0)\theta_1^2 + \gamma'(\theta_0)\theta_2\right) ....\end{aligned} \tag{71}$$

Taylor expanding γ in ϵ around $\epsilon = 0$ then reveals the identification

$$\gamma_0 = \gamma(\theta_0) \quad \text{and} \quad \gamma_1 = \gamma'(\theta_0)\theta_1. \tag{72}$$

For further analysis it will prove useful to calculate γ_0, γ_1 or θ_0, θ_1 explicitly in view of inner coordinates.

Inner expansions for θ

To this end we first consider the case when $u_x = 0$.
In inner coordinates $u_x = 0$ is equivalent to

$$\epsilon^{-1} n_1 U_\rho + (1 + \epsilon\rho\kappa)^{-1} t_1 U_s = 0,$$

for all $\epsilon > 0$, which may be rewritten to

$$n_1 U_\rho + \epsilon(\rho\kappa n_1 U_\rho + t_1 U_s) = 0.$$

As this is a polynomial in ϵ it is zero for all ϵ if an only if

$$n_1 U_\rho = 0 \quad \wedge \quad \rho\kappa n_1 U_\rho + t_1 U_s = 0.$$

Since we consider the inner problem at the interface, which describes phase transition we can assume that $U_\rho \neq 0$ and the condition may be rewritten as

$$n_1 = 0 \quad \wedge \quad U_s = 0, \tag{73}$$

where we also exploited that $t_1 = n_2 \neq 0$ since $(n_1, n_2) = 0$ cannot occur in inner coordinates, i.e. near the interface. Consequently we obtain that from $u_x = 0$ it follows that $n_1 = -t_2 = 0$ in inner coordinates, thus u_y reads

$$u_y = \epsilon^{-1} n_2 U_\rho + (1 + \epsilon\rho\kappa)^{-1} t_2 U_s = \epsilon^{-1} n_2 U_\rho.$$

Exploiting the definition of θ, i.e. (3) we then obtain that for $u_x = 0$ we have

$$\theta = \theta_0(u_y) = \begin{cases} +\frac{\pi}{2} & \text{for } n_2 U_\rho > 0 \\ -\frac{\pi}{2} & \text{for } n_2 U_\rho < 0 \end{cases} \tag{74}$$

where we also used that $n_2 U_\rho \neq 0$. Finally, since $\gamma(\theta) = \gamma(-\theta)$ we obtain that $\gamma = \gamma_0 = \gamma(\theta_0)$ is constant and in particular independent of ρ.

We now consider $u_x \neq 0$.
According to (73) this implies either $n_1 \neq 0$ or $U_s \neq 0$. We first consider $n_1 \neq 0$. In inner coordinates and exploiting $(t_1, t_2) = (n_2, -n_1)$, as well as $n_1^2 + n_2^2 = 1$, we have

$$\begin{aligned} \frac{u_y}{u_x} &= \frac{\epsilon^{-1} n_2 U_\rho + (1 + \epsilon\rho\kappa)^{-1} t_2 U_s}{\epsilon^{-1} n_1 U_\rho + (1 + \epsilon\rho\kappa)^{-1} t_1 U_s} = \frac{\epsilon^{-1} n_2 U_\rho + \rho\kappa n_2 U_\rho + t_2 U_s}{\epsilon^{-1} n_1 U_\rho + \rho\kappa n_1 U_\rho + t_1 U_s} \\ &= \frac{n_2 U_\rho + \epsilon\left(\rho\kappa n_2 U_\rho + t_2 U_s\right)}{n_1 U_\rho + \epsilon\left(\rho\kappa n_1 U_\rho + t_1 U_s\right)} \sim \frac{n_2}{n_1} - \epsilon \frac{U_s}{n_1^2 U_\rho}. \end{aligned}$$

A Taylor-expansion of θ at $\epsilon = 0$ then leads to

$$\theta = \arctan 2\,(n_2, n_1) - \epsilon \frac{U_s}{U_\rho} + O(\epsilon^2), \tag{75}$$

which reveals the identification

$$\theta_0 = \arctan 2\,(n_2, n_1) \quad \text{and} \quad \theta_1 = -\frac{U_s}{U_\rho}. \tag{76}$$

On the other hand, for $n_1 = -t_2 = 0$ and $U_s \neq 0$, we have

$$\frac{u_y}{u_x} = \epsilon^{-1} \frac{U_\rho}{U_s} + \rho\kappa \frac{U_\rho}{U_s},$$

such that in the limit $\epsilon \to 0$ we obtain

$$\theta = \theta_0 = \operatorname{sign}\left(\frac{U_\rho}{U_s}\right) \frac{\pi}{2}. \tag{77}$$

Finally we conclude that

$$\theta_0 = \begin{cases} \arctan 2(n_2, n_1) & \text{for } n_1 \neq 0 \\ \pm \frac{\pi}{2} & \text{for } n_1 = 0 \end{cases} \tag{78}$$

and

$$\theta_1 = \begin{cases} -\dfrac{U_s}{U_\rho} & \text{for } n_1 \neq 0 \\ 0 & \text{for } n_1 = 0. \end{cases} \tag{79}$$

Hence the leading order of θ and consequently also of γ is independent of ρ.

Time derivative in inner coordinates

Consider now the time derivative in inner coordinates. Since $\mathbf{R}$ is time dependent the time derivative becomes

$$\begin{aligned} \partial_\tau u &= \partial_\tau U - \nabla U \cdot \partial_\tau \mathbf{R} \\ &= \partial_\tau U - v_n \epsilon^{-1} \partial_\rho U - \frac{v_t}{1 + \epsilon\rho\kappa} \partial_s U, \end{aligned} \tag{80}$$

where $v_n := \partial_\tau \mathbf{R} \cdot \mathbf{n}$ and $t_n := \partial_\tau \mathbf{R} \cdot \mathbf{t}$ are the normal and tangential velocities respectively. Applying these inner expansions in (53) we find that the first two equations combined become

$$\epsilon^2 \partial_\tau U - \epsilon v_n \partial_\rho U - \frac{\epsilon^2 v_t}{1 + \epsilon\rho\kappa} \partial_s U = \nabla \cdot (m(U) \nabla M), \tag{81}$$

where

$$\begin{aligned} &\nabla \cdot (m(U)\nabla) \\ &= \epsilon^{-2} \partial_\rho m(U_0) \partial_\rho + \epsilon^{-1} \Big[\partial_\rho \Big(\kappa\rho m(U_0) + m'(U_0) U_1 \Big) \partial_\rho - \kappa\rho \partial_\rho m(U_0) \partial_\rho \Big] \\ &\quad + \Big[\kappa^2 \rho^2 \partial_\rho m(U_0) \partial_\rho - \kappa\rho \partial_\rho \Big(\kappa\rho m(U_0) + m'(U_0) U_1 \Big) \partial_\rho \\ &\quad + \partial_\rho \Big(\kappa\rho m'(U_0) U_1 + \frac{1}{2} m''(U_0) U_1^2 + m'(U_0) U_2 \Big) \partial_\rho + \partial_s m(U_0) \partial_s \Big] \\ &\quad + O(\epsilon). \end{aligned} \tag{82}$$

Taking only the first equation in (53) we have

$$\begin{aligned}\epsilon^2\partial_\tau U - \epsilon v_n \partial_\rho U - \frac{\epsilon^2 v_t}{1+\epsilon\rho\kappa}\partial_s U \\ = \frac{1}{1+\epsilon\rho\kappa}\left[\epsilon^{-1}\partial_\rho\Big((1+\epsilon\rho\kappa)\mathbf{n}\cdot\mathbf{J}\Big) + \partial_s\left(\frac{1}{1+\epsilon\rho\kappa}\mathbf{s}\cdot\mathbf{J}\right)\right],\end{aligned} \tag{83}$$

where we will only need to know the normal component $J_n = \mathbf{n}\cdot\mathbf{J}$, which can be expanded as

$$\begin{aligned}J_n &= \frac{m(U)}{\epsilon}\partial_\rho M \\ &= \epsilon^{-1}m(U_0)\partial_\rho M_0 + m'(U_0)U_1\partial_\rho M_0 + m(U_0)\partial_\rho M_1 \\ &+ \epsilon\left[m(U_0)\partial_\rho M_2 + m'(U_0)U_1\partial_\rho M_1 + m'(U_0)U_2\partial_\rho M_0 + \frac{1}{2}m''(U_0)U_1^2\partial_\rho M_0\right] \\ &+ \epsilon^2\left[m(U_0)\partial_\rho M_3 + m'(U_0)U_1\partial_\rho M_2 + \left(m'(U_0)U_2 + \frac{1}{2}m''(U_0)U_1^2\right)\partial_\rho M_1\right. \\ &\qquad \left. + \left(m'(U_0)U_3 + m''(U_0)U_1U_2 + \frac{1}{6}m'''(U_0)U_1^3\right)\partial_\rho M_0\right] + O(\epsilon^3).\end{aligned} \tag{84}$$

3.3.4 *Solutions with $|u| \leq 1$*

Resolution to an apparent contradiction

For the scope of this work, we will only consider solutions of the phase field model with $|u| \leq 1$. Such solutions have been shown to arise for the standard (isotropic) Cahn-Hilliard equation with degenerate mobilities from appropriate regularizations [32], and we will assume that similar procedures can be invoked in the anisotropic case. However, if we proceed with our long-time asymptotics in the usual way by assuming non-trivial outer solutions on both sides of the interface (where trivial means that $u = 1$ or $u = -1$ everywhere to all orders, i.e., the outer solution consists of the pure phases), then the $O(\varepsilon)$ correction to $u_0 = \pm 1$ leads to u that does not satisfy $|u| \leq 1$ on the convex side of the interface. This observation has been discussed at some length for the isotropic case in [23, 64].

In [64], a resolution to this apparent contradiction has been suggested, which we also apply here. Here we only summarize the salient features of the argument. The apparent contradiction can be resolved by observing that where the solution approaches $|u| = 1$ in the inner region on the convex side of the interface, it slows down due to the degeneracy in the mobility. In outer coordinates, we assume that this approach happens along a curve, χ, at a distance $\ll 1$ from the interface. The solution touches ± 1 along this curve in either finite time or approaches it in infinite time. In both cases, the problem effectively reduces to a problem with a free boundary χ. Derivation of the appropriate boundary conditions at χ would require an additional asymptotic analysis and, in the case where $u = \pm 1$ in finite time, an additional regularization. In principle, this regularization could permit

a non-zero flux through χ. However, fluxes from the outer solution including any fluxes through χ do not contribute to the interface motion to leading order (which is given by surface diffusion). Further conditions are required at the free boundary χ, and these we postulate in (86), following the example of [64].

Thus, let $\rho = -\omega(s,\tau)$ be the position of χ in inner (i.e. ρ-) coordinates. Introduce shifted inner coordinates, centered at χ, via

$$z = \rho + \omega(s,\tau). \tag{85}$$

The corresponding inner expansions may then be written as

$$\begin{aligned}\overline{U} &= 1 + \epsilon\overline{U}_1 + \epsilon^2\overline{U}_2...,\\ \overline{M} &= \overline{M}_0 + \epsilon\overline{M}_1 + \epsilon^2\overline{M}_2...,\\ \bar{\mathbf{J}} &= \epsilon^{-1}\bar{\mathbf{J}}_{-1} + \bar{\mathbf{J}}_0 + \epsilon\bar{\mathbf{J}}_1 + \epsilon^2\bar{\mathbf{J}}_2...\end{aligned}$$

and we postulate that the boundary conditions

$$\overline{U}(0) = 1, \qquad \partial_z\overline{U}(0) = 0 \tag{86}$$

hold to the first two orders in ϵ. Note that since the position of the two inner layers depends also on ϵ, the positions ω and R actually need to be expanded in terms of ϵ as well. But since we are only interested in the leading order behavior of the interface we use ω and R and their leading order contributions interchangeably. We now solve and match the outer and inner problems order by order.

3.3.5 *Matching*

Leading order

Outer problem

For the leading order outer problem we obtain

$$0 = \nabla\cdot\mathbf{j}_0, \qquad \mathbf{j}_0 = m(u_0)\nabla\mu_0, \qquad \mu_0 = F'(u_0), \tag{87}$$

and the corresponding boundary conditions are $\mathbf{n}_\Omega\cdot\nabla u = 0$ and $\mathbf{n}_\Omega\cdot\mathbf{j}_0 = 0$. Since we suppose that the "$-$" phase is outside the solid film, we conclude that

$$u_0 = -1, \qquad \mu_0 = 0. \tag{88}$$

Inner problem

The leading order inner expansion reads

$$\partial_\rho(m(U_0)\partial_\rho M_0) = 0, \tag{89a}$$

$$F'(U_0) - \partial_\rho\left(\gamma_0^2\partial_\rho U_0\right) = M_0. \tag{89b}$$

Integrating once in ρ, we obtain

$$m(U_0)\partial_\rho M_0 = a_1(s,\tau). \tag{90}$$

From the matching conditions we require

$$\lim_{\rho\to\infty} U_0(\rho) = -1, \tag{91}$$

which implies $a_1 \equiv 0$ and therefore first $M_0 = const.$ and then with the same argument and in view of (89b) also $M_0 = 0$. Moreover, from (77) we know that θ_0 is constant in ρ, which leads to

$$2(U_0^3 - U_0) - \gamma_0^2 \partial_{\rho\rho} U_0 = 0 \tag{92}$$

and, by applying the phase condition $U_0(0) = 0$ (obtained from (57)), consequently

$$U_0 = -\tanh\left(\frac{1}{\gamma_0}\rho\right). \tag{93}$$

Using $M_0 = 0$ we also conclude that

$$J_{n,-1} = 0. \tag{94}$$

Finally it is easily seen, that from the inner expansions about χ we get

$$\overline{U}_0 = 1, \qquad \overline{M}_0 = 0, \qquad \overline{J}_{n,-1} = 0. \tag{95}$$

Particular inner expansion for θ_1

For the $O(\epsilon)$ correction we will need to know the particular representation of the inner expansion for θ_1 in view of U_0. To this end we first consider the case $n_1 \neq 0$. From (79) we already know that

$$\theta_1 = -\frac{U_s}{U_\rho} \sim -\frac{\partial_s U_0}{\partial_\rho U_0}. \tag{96}$$

Exploiting the leading order representation of U, i.e.

$$U_0 = -\tanh\left(\frac{1}{\gamma_0}\rho\right),$$

we calculate

$$\begin{aligned} \partial_s U_0 &= (1 + U_0^2)\frac{\rho\, \partial_s \gamma_0}{\gamma_0^2}, \\ \partial_\rho U_0 &= -(1 + U_0^2)\frac{1}{\gamma_0}, \end{aligned} \tag{97}$$

and since $\gamma_0 = \gamma(\arctan 2(n_2, n_1))$ we obtain from the Frenet-Serret formulae (59)

$$\partial_s \gamma_0 = \gamma_0' \, \frac{n_1 \partial_s n_2 - n_2 \partial_s n_1}{n_1^2 + n_2^2} = -\gamma_0' \kappa. \tag{98}$$

Applying (97) and (98) in (96) then gives

$$\theta_1 \sim -\frac{\gamma_0'}{\gamma_0}\rho\kappa. \tag{99}$$

Note that in the case $n_1 = 0$ the leading order of γ is constant and in particular independent of s and ρ. Consequently the representation (99) can be applied to this case as well as it is zero and this is consistent with (79).

$O(\epsilon)$ correction

Outer problem

The first two parts of the outer $O(\epsilon)$ correction problem for (53) are trivial, since $\mu_0 = 0$ and $m(u_0) = 0$ and consequently

$$\mathbf{j}_1 = 0. \tag{100}$$

The last equation becomes

$$\mu_1 = F''(u_0)u_1 = 4u_1, \tag{101}$$

which we need to match to M_1 in the following. As $M_0 = 0$ we obtain for the first equation of the inner correction problem

Inner problem

$$\partial_\rho(m(U_0)\partial_\rho M_1) = 0, \tag{102}$$

such that $m(U_0)\partial_\rho M_1$ is constant in ρ. Comparison with (84) then reveals that (102) corresponds to the normal flux term $J_{n,0}$, which has to match with j_0 and consequently is zero. Thus M_1 does not depend on ρ.

Applying curvilinear coordinates the equation for M_1 reads

$$\begin{aligned} M_1 = F''(U_0)U_1 - \Big(&\mathbf{t}\partial_s\big(-\gamma_0\gamma_0'\mathbf{t}\partial_\rho U_0 + \gamma_0^2\mathbf{n}\partial_\rho U_0\big) + \mathbf{n}\partial_\rho\big(\gamma_0\gamma_0'\mathbf{n}\partial_s U_0 + \gamma_0^2\mathbf{t}\partial_s U_0\big) \\ &+ \mathbf{n}\partial_\rho\big(-(\gamma_1\gamma_0' + \gamma_0\gamma_1')\,\mathbf{t}\partial_\rho U_0 - \gamma_0\gamma_0'\mathbf{t}\partial_\rho U_1 + 2\gamma_0\gamma_1\mathbf{n}\partial_\rho U_0 + \gamma_0^2\mathbf{n}\partial_\rho U_1\big)\Big). \end{aligned} \tag{103}$$

Exploiting that $\gamma_0, \mathbf{n}$ and $\mathbf{t}$ do not depend on ρ, applying the two-dimensional Frenet-Serret formulae (59), i.e.

$$\partial_s\mathbf{t} = -\kappa\mathbf{n}, \qquad \partial_s\mathbf{n} = \kappa\mathbf{t},$$

and using the ρ-independence of θ_0 (see (77)) in order to calculate $\partial_s\gamma_0$, equation (103) becomes

$$M_1 = F''(U_0)U_1 - \kappa(\gamma_0'' + \gamma_0)\gamma_0\partial_\rho U_0 + \kappa\gamma_0'^2\partial_\rho U_0 + 2\kappa\gamma_0'^2\rho\partial_{\rho\rho}U_0 - \gamma_0^2\partial_{\rho\rho}U_1. \tag{104}$$

Note that we also exploited the particular representation (99) of θ_1. From (104) we then obtain the ordinary differential equation

$$\begin{aligned} \gamma_0^2\partial_{\rho\rho}U_1 - 2(3U_0^2 - 1)U_1 = &-\kappa c_1\gamma_0\partial_\rho U_0 + \kappa c_2\ \gamma_0\partial_\rho U_0 \\ &+ 2\kappa c_2\ \gamma_0\rho\partial_{\rho\rho}U_0 - M_1, \end{aligned} \tag{105}$$

where we substituted $c_1 := \gamma_0'' + \gamma_0$ and $c_2 := \gamma_0'^2/\gamma_0$. Then the general solution of (105) is given by

$$\begin{aligned} U_1 = {} & C_1\operatorname{sech}^2\left(\frac{\rho}{\gamma_0}\right) + C_2\operatorname{sech}^2\left(\frac{\rho}{\gamma_0}\right)\left(\frac{3\rho}{8\gamma_0} + \frac{1}{4}\sinh\left(\frac{2\rho}{\gamma_0}\right) + \frac{1}{32}\sinh\left(\frac{4\rho}{\gamma_0}\right)\right) \\ & + \frac{1}{8}(2c_1\kappa - M_1) + \frac{1}{48}(2c_1\kappa - 3M_1)\left(2\cosh\left(\frac{2\rho}{\gamma_2}\right) - 5\operatorname{sech}^2\left(\frac{\rho}{\gamma_0}\right)\right) \\ & - \frac{1}{2}c_2\kappa\left(\frac{\rho}{\gamma_0}\right)^2\operatorname{sech}^2\left(\frac{\rho}{\gamma_0}\right), \end{aligned} \tag{106}$$

and including the interface condition $U_1(0) = 0$ and boundedness as $\rho \to \infty$ to match with the outer solution, the two constants are given by

$$C_1 = -\frac{1}{16}(M_1 + 2c_1\kappa), \qquad C_2 = \frac{1}{3}(3M_1 - 2c_1\kappa). \tag{107}$$

Finally for the inner layer about χ, according to $\overline{U}_0 \equiv 1$, we obtain $F''(\overline{U}_0) = 4$ and $\partial_\rho \overline{U}_0 = 0$. Recalling (104), we then obtain the ordinary differential equation

$$M_1 = 4\overline{U}_1 - \gamma_0^2 \partial_{zz} \overline{U}_1, \tag{108}$$

with initial conditions

$$\overline{U}_1(0) = \overline{U}_1'(0) = 0. \tag{109}$$

The general solution of (108) is given by

$$\overline{U}_1 = A\exp(2z) + B\exp(-2z) + \frac{M_1}{4} \tag{110}$$

and substituting the initial conditions (109) we arrive at

$$\overline{U}_1 = \frac{M_1}{4}\left(1 - \cosh\left(\frac{2\bar{z}}{\gamma_0}\right)\right). \tag{111}$$

Exponential matching

Motivation for exponential matching

We will now match the two interior layers. We first observe that on the one hand, from the definition of $\omega(s,\tau)$ in the paragraph before equation (85), we have that $U(s,\omega,\tau) = 1$ and $U'(s,\omega,\tau) = 0$. On the other hand, for $\epsilon \to 0$, we also have that $U \to U_0 = -\tanh(\rho/\gamma_0) < 1$ which suggests to assume $\omega(s,\tau) \to \infty$ for $\epsilon \to 0$. Matching of the inner expansions therefore involves exponential terms with large negative arguments ρ, which we deal with in the spirit of Langer [63]. The corresponding method entails to explicitly match the exponentially growing and decaying terms in the expansion. Note that this method was also considered in Lee et al. [64] and has been generalized to partial differential equations of higher (fourth and sixth) order in [62]. The solution centered at the interface is expanded at $\rho \to -\infty$ and the result written and re-expanded in terms of $z = \rho + \omega(s,\tau)$. The solution for the layer around the free boundary ξ is directly expanded in terms of $z \to \infty$ and then the terms are matched between the two expansions.

Expanding U_0 and U_1 for $\rho \to -\infty$ and substituting $\rho = z - \omega$ gives

$$\begin{aligned} U_0 &= 1 - \underbrace{2e^{-\frac{2}{\gamma_0}\omega} e^{\frac{2}{\gamma_0}z}}_{\text{A}} + O(e^{4z}), \\ U_1 &= \underbrace{\frac{1}{24}(2c_1\kappa - 3M_1)e^{\frac{2}{\gamma_0}\omega} e^{-\frac{2}{\gamma_0}z}}_{\text{B}} + \underbrace{\frac{1}{2}(c_1\kappa - M_1)}_{\text{C}} \\ &\quad + \underbrace{\left[\left(\frac{7M_1}{4} - \frac{11c_1\kappa}{6}\right) + \left(\frac{3M_1}{2} - c_1\kappa\right)\frac{z-\omega}{\gamma_0} - 2c_2\kappa\left(\frac{z-\omega}{\gamma_0}\right)^2\right] e^{-\frac{2}{\gamma_0}\omega} e^{\frac{2}{\gamma_0}z}}_{\text{D}} \\ &\quad + O(e^{4z}). \end{aligned} \tag{112}$$

The inner expansion about the free boundary can be rewritten as

$$\overline{U} = 1 + \underbrace{\frac{\epsilon M_1}{4}}_{\text{E}} - \underbrace{\frac{\epsilon M_1}{8} e^{\frac{2}{\gamma_0}z}}_{\text{F}} - \underbrace{\frac{\epsilon M_1}{8} e^{-\frac{2}{\gamma_0}z}}_{\text{G}} + O(\epsilon^2). \tag{113}$$

Comparing the terms in (112) and (113) of the same order of ϵ, we first observe that the constant terms at $O(1)$ are already matched. Matching ϵC and E yields

$$\frac{M_1}{4} = \frac{1}{2}(c_1\kappa - M_1), \tag{114}$$

where $c_1 = \gamma_0'' + \gamma_0 > 0$, thus

$$M_1 = \frac{2}{3}(\gamma_0'' + \gamma_0)\kappa. \tag{115}$$

Applying (115) in B reveals B $= 0$. Matching term A and F we arrive at

$$2e^{-\frac{2}{\gamma_0}\omega} = \frac{\epsilon}{12}(\gamma_0'' + \gamma_0)\kappa, \tag{116}$$

which we solve for ω giving

$$\omega = \frac{\gamma_0}{2}\log\left(\frac{24}{\epsilon(\gamma_0'' + \gamma_0)}\right). \tag{117}$$

This asymptotic analysis shows that without the contact line χ, i.e. if we were to consider only one inner layer about the interface and would match to the outer solution of the "+" phase via $U' = 0$ for $\rho \to -\infty$, we would expect an outer solution (of the "+" phase) which tends to a value of 1 plus a positive $O(\epsilon)$ term, i.e. $u = 1 + c\epsilon(\gamma_0'' + \gamma_0)\kappa + O(\epsilon^2)$, where $c > 0$. This can be seen by matching (101) to (115). This solution intersects $u = 1$ at a distance $\omega = O(\log(1/\epsilon))$ from the interface, which is large but tends to zero in the outer variable. The assumption $|u| \leq 1$ thus implies that (86) has to be satisfied in the inner variable but since ω depends, though only logarithmically, on ϵ, this involves exponentially re-expanding the inner solution.

Note that at this stage, it is obvious that the matching is not yet complete to $O(\epsilon)$, as the terms in (112) and (113), or to be more precise

ϵD and G, are non-zero and lack counterparts in the other expansion. This can be resolved by considering the next higher order solutions U_2 and $\bar{U}_2$, which is similarly technical and does not influence the further asymptotic analysis of this work.

$O(\epsilon^2)$ correction

Since $m'(u_0) = 0$ we obtain for the outer correction problem *Outer problem*

$$\mathbf{n} \cdot \mathbf{j_2} = 0, \tag{118}$$

and again the first two parts of (53) are automatically satisfied. The last part requires

$$\mu_2 = \frac{1}{2} F'''(u_0) u_1^2 + F''(u_0) u_2, \tag{119}$$

where $F'''(u_0) = -12$ and $F''(u_0) = 4$.

Considering the inner correction problem and recalling that M_0, M_1 are independent of ρ we obtain for the first part of (53) *Inner problem*

$$\partial_\rho (\mu(U_0) \partial_\rho M_2) = 0, \tag{120}$$

thus $m(U_0)\partial_\rho M_2$ is constant in ρ and since we can identify this expression via (84) as $J_{n,1}$ which has to match with $\mathbf{n} \cdot \mathbf{j}_1$ we find that

$$J_{n,1} = m(U_0)\partial_\rho M_2 = 0. \tag{121}$$

Therefore, M_2 is independent of ρ.

$O(\epsilon^3)$ correction

Consider only the inner correction problem at this point. Since we have $m'(U_0) = m''(U_0) = 0$ we obtain from (84) that *Inner problem*

$$J_{n,2} = m(U_0)\partial_\rho M_3. \tag{122}$$

For $\rho \to -\infty$ the left hand side has to match with $\overline{J}_{n,2}$ and the right hand side with $m(1)\overline{M}_3$, but since $\overline{J}_{n,2} = 0$ we immediately obtain that M_3 is constant in ρ and

$$\lim_{\rho \to -\infty} J_{n,2} = \lim_{\rho \to -\infty} m(U_0)\partial_\rho M_3 = 0 \tag{123}$$

Moreover, $J_{n,2}$ also matches with $\mathbf{n} \cdot \mathbf{j}_2 = 0$ for $\rho \to \infty$. Considering the last part of the correction problem for (53) and exploiting that M_0, M_1 and M_2 are independent of ρ we find

$$\begin{aligned} -v_n \partial_\rho U_0 &= \partial_\rho m(U_0)\partial_\rho M_3 + \partial_s m(U_0)\partial_s M_1 \\ &= \partial_\rho m(U_0)\partial_\rho M_3 + \frac{2}{3} m(U_0)\partial_{ss}(c_1 \kappa). \end{aligned}$$

An integration over $(-\infty, \infty)$ then yields

$$v_n = \left(\frac{2}{3}\right)^2 \partial_{ss}(c_1 \kappa). \tag{124}$$

Identifying the sharp interface model

Finally, we obtain the sharp interface problem which correctly describes the anisotropic evolution due to surface diffusion

$$\begin{aligned} \mu_1 &= \frac{2}{3}(\gamma_0 + \gamma_0'')\kappa, \\ v_n &= \left(\frac{2}{3}\right)^2 \partial_{ss}((\gamma_0 + \gamma_0'')\kappa), \end{aligned} \tag{125}$$

on χ_0.

3.4 SHARP INTERFACE DYNAMICS ON SOLID BOUNDARIES

Literature on boundary conditions at triple junctions

We now focus our studies on the behavior of equation (53) in a local domain around the contact point $(x_0, 0)$ with boundary condition (49b). The more general topic of boundary conditions at triple junctions has already been studied by [11, 36] for the Allen-Cahn equation and in [88] for an Allen-Cahn/Cahn-Hilliard system where in both cases the surface energies are assumed to be isotropic which leads to Young's law in the sharp interface limit. Another work by Owen et al. [90] considers the boundary conditions for an Allen-Cahn gradient flow on a solid substrate where the corresponding geometry turns out to be suitable for our problem.

Motivated by [90] we study the behavior of u in a box around the contact point $(x_0, 0)$. Introducing a boundary layer and an interior layer which imply corresponding matching conditions, we will show that the leading order system of (53) with boundary condition (49b) leads to a contact angle boundary condition, which is referred to as the Young-Herring condition in the literature [8, 78]. The subsequent analysis is given for the left contact point but carries over correspondingly to the right contact point.

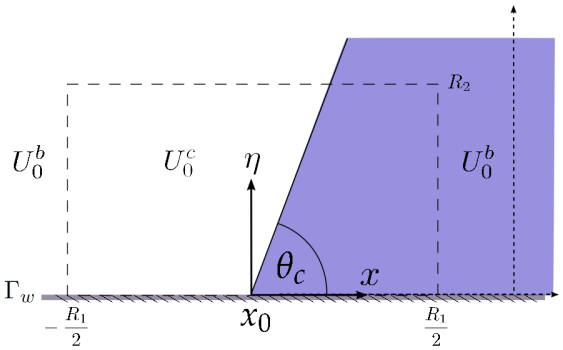

Figure 9: A sketch of the local domain.

3.4.1 *Boundary layer near* Γ_w

Cartesian coordinates, stretched in one direction

We first introduce the inner variable near Γ_w via

$$\eta = \frac{y}{\epsilon}, \tag{126}$$

see Fig. 9, and correspondingly U^b, M^b, γ^b and θ^b. We expand $U^b(x,\eta)$ and M^b into

$$\begin{aligned} U^b &= U_0^b + \epsilon U_1^b + \epsilon^2 U_2^b ..., \\ M^b &= M_0^b + \epsilon M_1^b + \epsilon^2 M_2^b .... \end{aligned} \tag{127}$$

Moreover we find for γ^b the expansion

$$\begin{aligned} \gamma^b &= \gamma(\theta_0^b) \quad + \epsilon\gamma'(\theta_0^b)\theta_1^b + ... \\ &=: \ \gamma_0^b \qquad + \epsilon\gamma_1^b \quad + ... \end{aligned} \tag{128}$$

Inner expansions for θ^b

where θ_0^b is the leading order of the inner expansion for

$$\theta^b = \operatorname{atan2}\left(\partial_\eta U^b, \epsilon\partial_x U^b\right).$$

Realizing that for ϵ sufficiently small we may assume that

$$\left|\frac{\partial_\eta U^b}{\epsilon\partial_x U^b}\right| > 1$$

the inverse tangent function can be represented by

$$\arctan\left(\frac{\partial_\eta U^b}{\epsilon\partial_x U^b}\right) = \operatorname{sgn}\left(\frac{\partial_x U^b}{\partial_\eta U^b}\right)\frac{\pi}{2} - \arctan\left(\frac{\epsilon\partial_x U^b}{\partial_\eta U^b}\right)$$

and applying a Taylor-expansion to this representation reveals

$$\arctan\left(\frac{\partial_\eta U^b}{\epsilon\partial_x U^b}\right) = \operatorname{sgn}\left(\frac{\partial_x U^b}{\partial_\eta U^b}\right)\frac{\pi}{2} - \epsilon\frac{\partial_x U^b}{\partial_\eta U^b} + ...$$

such that

$$\theta_0^b = \begin{cases} \operatorname{sgn}\left(\partial_\eta U_0^b\right)\frac{\pi}{2} & \text{for } \partial_x U_0^b \geq 0, \\ -\operatorname{sgn}\left(\partial_\eta U_0^b\right)\frac{\pi}{2} & \text{for } \partial_x U_0^b < 0, \\ 0 & \text{for } \partial_x U_0^b = 0 \text{ and } \partial_\eta U_0^b = 0. \end{cases} \tag{129}$$

Since, without loss of generality, we may assume that in the inner region the case $\partial_x U_0^b = 0$ and $\partial_\eta U_0^b = 0$ does not occur and since $\gamma(\frac{\pi}{2}) = \gamma(-\frac{\pi}{2})$, we conclude that γ_0^b is constant, i.e.

$$\gamma_0^b = \gamma(\theta_0^b) = \gamma(\pm\frac{\pi}{2}).$$

The leading order problem of (53) then reads

$$0 = \partial_\eta \left(m(U_0^b)\partial_\eta M_0^b \right), \tag{130a}$$

$$M_0^b = F'(U_0^b) - \partial_\eta \left((\gamma_0^b)^2 \partial_\eta U_0^b \right), \tag{130b}$$

with boundary conditions

$$(\gamma_0^b)^2 \partial_\eta U_0^b = \frac{f_w'(U_0^b)}{\lambda_m}, \qquad m(U_0^b)\partial_\eta M_0^b = 0, \tag{130c}$$

at $\eta = 0$. Considering (130a) we first observe that

$$a_1(\tau, x) = m(U_0^b)\partial_\eta M_0^b,$$

where $a_1(\tau, x)$ is a constant of integration and including the no-flux boundary condition at $\eta = 0$ it follows that $a_1(\tau, x)$ must be zero. This also implies that either $m(U_0^b) = 0$ or $\partial_\eta M_0^b = 0$. Considering $m(U_0^b) \neq 0$, which corresponds to the region about the interface, we obtain that M_0^b is constant in η. Matching to $M_0 = 0$ away from the substrate, i.e. for $\eta \to \infty$, we conclude that M_0^b must be zero as well. On the other hand, the region where $U_0^b = \pm 1$ corresponds to the pure phases where we may assume that the chemical potential is constant and similar arguments as before lead to $M_0^b = 0$. Consequently we obtain for (130b)

$$0 = F'(U_0^b) - \partial_\eta \left((\gamma_0^b)^2 \partial_\eta U_0^b \right). \tag{131}$$

Multiplying by $\partial_\eta U_0^b$ and integrating over η then yields

$$\int F'(U_0^b)\partial_\eta U_0^b \, d\eta = \int \partial_\eta \left((\gamma_0^b)^2 \partial_\eta U_0^b \right) \partial_\eta U_0^b \, d\eta \tag{132}$$

which, since γ_0^b is constant, leads to

$$F(U_0^b) = \frac{1}{2}(\gamma_0^b)^2 \left(\partial_\eta U_0^b \right)^2 + a_2(\tau, x). \tag{133}$$

As U_0^b has to match to $u_0 \equiv -1$ for $x \to -\infty$, a_2 must be zero as well, and consequently we have

$$F(U_0^b) = \frac{1}{2}(\gamma_0^b)^2 \left(\partial_\eta U_0^b \right)^2. \tag{134}$$

3.4.2 *Contact line region*

Next we introduce an interior layer centered at the contact point $(x_0, 0)$. We choose inner coordinates which are stretched in both directions, i.e.

Cartesian coordinates, stretched in both directions

$$\xi = \frac{x - x_0}{\epsilon}, \qquad \eta = \frac{y}{\epsilon}, \tag{135}$$

and also the corresponding dependent variables and their expansions

$$\begin{aligned} U^c &= U_0^c + \epsilon U_1^c + \epsilon^2 U_2^c ..., \\ M^c &= M_0^c + \epsilon M_1^c + \epsilon^2 M_2^c .... \end{aligned} \tag{136}$$

Similar as before we have for γ^c the expansion

$$\begin{aligned} \gamma^c &= \gamma(\theta_0^c) \quad + \epsilon \gamma'(\theta_0^c)\theta_1^c + ... \\ &=: \quad \gamma_0^c \qquad\quad + \epsilon \gamma_1^c \quad + ... \end{aligned} \tag{137}$$

where now

$$\theta_0^c = \operatorname{atan2}\left(\partial_\eta U_0^c, \partial_{\tilde{\xi}} U_0^c\right). \tag{138}$$

The leading order problem of (53) then reads (with $\nabla' \equiv (\partial_{\tilde{\xi}}, \partial_\eta)$)

$$0 = \nabla' \left(m(U_0^c) \nabla' M_0^c \right), \tag{139a}$$

$$M_0^c = F'(U_0^c) - \nabla' \cdot \left(\gamma_0^c \gamma_0^{c\prime} \begin{pmatrix} -\partial_\eta U_0^c \\ \partial_{\tilde{\xi}} U_0^c \end{pmatrix} + (\gamma_0^c)^2 \nabla' U_0^c \right). \tag{139b}$$

and we have the leading order boundary conditions

$$\gamma_0^c \gamma_0^{c\prime} \partial_{\tilde{\xi}} U_0^c + (\gamma_0^c)^2 \partial_\eta U_0^c = \frac{f_w'(U_0^c)}{\lambda_m}, \qquad m(U_0^c)\partial_\eta M_0^c = 0, \tag{139c}$$

at $\eta = 0$. Note that since no $O(1)$ contribution has occurred in all the previous sections and computation in the expansion for the chemical potential, neither in the outer solution nor in either of the types of inner solutions, it is reasonable to assume that $M_0^c \equiv 0$. This assumption was also made in [88]. Consider now a box R of size R_1 in the $\tilde{\xi}$-direction and R_2 in the η direction (see Fig. 9). Multiplying (139b) by $\partial_{\tilde{\xi}} U_0^c$ and integrating over R then leads to

$$\begin{aligned} \iint_R \partial_{\tilde{\xi}} U_0^c F'(U_0^c) = \iint_R \partial_{\tilde{\xi}} U_0^c \Big[& \partial_{\tilde{\xi}} \left(-\gamma_0^c \gamma_0^{c\prime} \partial_\eta U_0^c + (\gamma_0^c)^2 \partial_{\tilde{\xi}} U_0^c \right) \\ & + \partial_\eta \left(\gamma_0^c \gamma_0^{c\prime} \partial_{\tilde{\xi}} U_0^c + (\gamma_0^c)^2 \partial_\eta U_0^c \right) \Big], \end{aligned} \tag{140}$$

which can be rewritten as

$$\begin{aligned} (\text{LHS}) &:= \iint_R \partial_{\tilde{\xi}} \left[F(U_0^c) + \frac{1}{2}(\gamma_0^c)^2 \left(\partial_\eta U_0^c\right)^2 - \frac{1}{2}(\gamma_0^c)^2 \left(\partial_{\tilde{\xi}} U_0^c\right)^2 + \gamma_0^c \gamma_0^{c\prime} \partial_{\tilde{\xi}} U_0^c \partial_\eta U_0^c \right] \\ &= \iint_R \partial_\eta \left[\partial_{\tilde{\xi}} U_0^c \left(\gamma_0^c \gamma_0^{c\prime} \partial_{\tilde{\xi}} U_0^c + (\gamma_0^c)^2 \partial_\eta U_0^c \right) \right] =: (\text{RHS}) \end{aligned} \tag{141}$$

where we exploited that

$$\frac{1}{2}\partial_{\tilde{\xi}} (\gamma_0^c)^2 = \gamma_0^c \gamma_0^{c\prime} \, \frac{\partial_{\tilde{\xi}} \partial_\eta U_0^c \partial_{\tilde{\xi}} U_0^c - \partial_{\tilde{\xi}\tilde{\xi}} U_0^c \partial_\eta U_0^c}{\left(\partial_{\tilde{\xi}} U_0^c\right)^2 + \left(\partial_\eta U_0^c\right)^2}.$$

We first consider the left hand side (LHS) of (141), integrate in $\tilde{\xi}$ and apply that $\partial_{\tilde{\xi}} U_0^c \to 0$ as $|\tilde{\xi}| \to \infty$ for finite energy solutions, giving

$$\lim_{R_1, R_2 \to \infty} (\text{LHS}) = \lim_{R_1 \to \infty} \int_0^\infty \left[F(U_0^c) + \frac{1}{2}(\gamma_0^c)^2 \left(\partial_\eta U_0^c\right)^2 \right]_{-\frac{R_1}{2}}^{\frac{R_1}{2}} d\eta. \tag{142}$$

In order to match U_0^c with U_0^b for large ξ we have the matching conditions

$$\begin{aligned}\lim_{\xi\to+\infty} U_0^c &= \lim_{x\to x_c^+} U_0^b(x,\eta) =: U_0^{b+}(x_c,\eta),\\ \lim_{\xi\to-\infty} U_0^c &= \lim_{x\to x_c^-} U_0^b(x,\eta) =: U_0^{b-}(x_c,\eta),\end{aligned} \tag{143}$$

where U_0^{b+} denotes the solution which corresponds to the side of the "+" phase and U_0^{b-} the solution which corresponds to the side of the "−" phase. Moreover, recalling (134) and (129) we obtain

$$\partial_\eta U_0^{b+} = \frac{1}{|\gamma_0^b|}\sqrt{2F(U_0^{b+})}, \qquad \text{and} \qquad \partial_\eta U_0^{b-} = -\frac{1}{|\gamma_0^b|}\sqrt{2F(U_0^{b-})}. \tag{144}$$

We then obtain for (142)

$$\begin{aligned}\lim_{R_1,R_2\to\infty}(\text{LHS}) &= \int_0^\infty 2F(U_0^{b+}(x_c,\eta))\,d\eta - \int_0^\infty 2F(U_0^{b-}(x_c,\eta))\,d\eta\\ &= \sqrt{2}|\gamma_0^b|\left(\int_0^1\sqrt{F(t)}\,dt + \int_0^{-1}\sqrt{F(t)}\,dt\right)\\ &= |\gamma_0^b|\left(\frac{2}{3}-\frac{2}{3}\right) \;=\; 0\end{aligned} \tag{145}$$

where we also applied the specific form of $F(u) = \frac{1}{2}(1-u^2)^2$.

Considering the right hand side (RHS) of (141) we first obtain after integrating in η and including the boundary condition (139c)

$$\begin{aligned}(\text{RHS}) &= \left[\int_{-R_1/2}^{R_1/2}\partial_\xi U_0^c\left(\gamma_0^c\gamma_0^{c\prime}\partial_\xi U_0^c + (\gamma_0^c)^2\partial_\eta U_0^c\right)\,d\xi\right]_0^{R_2}\\ &= \underbrace{\int_{-R_1/2}^{R_1/2}\partial_\xi U_0^c\left(\gamma_0^c\gamma_0^{c\prime}\partial_\xi U_0^c + (\gamma_0^c)^2\partial_\eta U_0^c\right)\,d\xi\Big|_{R_2}}_{\text{I}} - \underbrace{\int_{-R_1/2}^{R_1/2}\partial_\xi U_0^c\frac{f_w'(U_0^c)}{\lambda_m}\,d\xi}_{\text{II}}\end{aligned}$$

where (II) in the limit $R_1, R_2 \to \infty$ is

$$\lim_{R_1,R_2\to\infty}(\text{II}) = \frac{1}{\lambda_m}\int_{-1}^1 f_w'(t)\,dt = \frac{1}{\lambda_m}(\gamma_{FS}-\gamma_{VS}). \tag{146}$$

Curvilinear coordinates at R_2

Analysing (I) we continue by transforming into a local coordinate system that is aligned with the tangent and normal direction to the film/vapor interface at $(x_0, 0)$ (see Fig. 10), that is

$$\begin{aligned}\rho &= -\xi\sin\theta_c \;+\; \eta\cos\theta_c\\ \varsigma &= \;\;\xi\cos\theta_c \;+\; \eta\sin\theta_c\end{aligned} \tag{147}$$

and consequently

$$\begin{aligned}\partial_\xi &= -\sin\theta_c\partial_\rho \;+\; \cos\theta_c\partial_\varsigma\\ \partial_\eta &= \;\;\cos\theta_c\partial_\rho \;+\; \sin\theta_c\partial_\varsigma.\end{aligned} \tag{148}$$

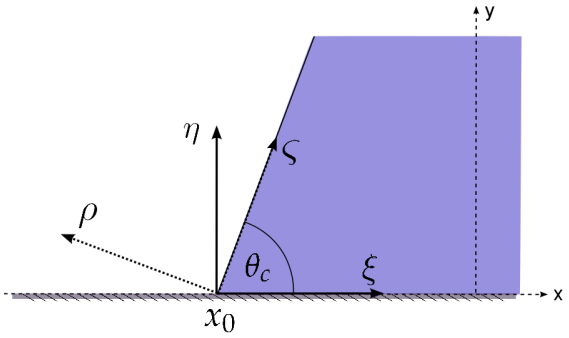

Figure 10: A sketch of the coordinate transformation.

Here $\theta_c \in (0, \pi)$ denotes the contact angle on the right hand side of the thin solid film which has negative sign due to the geometric orientation (see Fig. 10). The transformed integral then reads

$$(\mathrm{I}) = \int_{\frac{R_1}{2}\sin\theta_c + R_2\cos\theta_c}^{-\frac{R_1}{2}\sin\theta_c + R_2\cos\theta_c} S \, d\rho \tag{149}$$

where

$$\begin{aligned} S =& \gamma_0^c \gamma_0^{c\prime} \left(-\sin\theta_c \left(\partial_\rho U_0^c\right)^2 + 2\cos\theta_c \partial_\rho U_0^c \partial_\varsigma U_0^c - \frac{\cos^2\theta_c}{\sin\theta_c} \partial_\varsigma \left(U_0^c\right)^2 \right) \\ &+ \left(\gamma_0^c\right)^2 \left(\cos\theta_c \partial_\rho \left(U_0^c\right)^2 + \left(\sin\theta_c - \frac{\cos^2\theta_c}{\sin\theta_c} \right) \partial_\rho U_0^c \partial_\varsigma U_0^c - \cos\theta_c \partial_\varsigma \left(U_0^c\right)^2 \right). \end{aligned} \tag{150}$$

Realizing that for $\varsigma \to \infty$ the leading order U_0^c hat to mach with the leading order (93) from the previous section, which is constant in ς, reveals $\lim_{\varsigma\to\infty} \partial_\varsigma U_0^c = 0$. Taking the limit $R_1 \to \infty, R_2 \to \infty$ in the following way:

$$\lim_{R_1,R_2\to\infty} (\mathrm{I}) = \lim_{a\to\infty} \lim_{\substack{R_1\to\infty \\ R_2\to\infty \\ |R_1\sin\theta_c + R_2\cos\theta_c| < a}} \int_{\frac{R_1}{2}\sin\theta_c + R_2\cos\theta_c}^{-\frac{R_1}{2}\sin\theta_c + R_2\cos\theta_c} S \, d\rho, \tag{151}$$

which ensures that we don't match "into the substrate", leads to

$$\lim_{R_1,R_2\to\infty} (\mathrm{I}) = -\left(-\gamma_0^c \gamma_0^{c\prime} \sin\theta_c + \left(\gamma_0^c\right)^2 \cos\theta_c \right) \int_{-\infty}^{\infty} \left(\partial_\rho U_0^c\right)^2 \, d\rho \tag{152}$$

where we applied that

$$\begin{aligned} \lim_{\varsigma\to\infty} \gamma_0^c &= \gamma(\mathrm{atan2}\left(\cos\theta_c, -\sin\theta_c\right)) = \gamma_0, \\ \lim_{\varsigma\to\infty} \gamma_0^{c'} &= \gamma'(\mathrm{atan2}\left(\cos\theta_c, -\sin\theta_c\right)) = \gamma_0', \end{aligned} \tag{153}$$

and consequently $\lim_{\varsigma\to\infty} \gamma_0^c$ and $\lim_{\varsigma\to\infty} \gamma_0^{c'}$ are constant in ς and ρ. Moreover, note that θ_0^c and θ_c are related by

$$\theta_0^c = \begin{cases} \theta_c + \frac{\pi}{2} & \text{for } \theta_c \le \frac{\pi}{2} \\ \theta_c - \frac{3\pi}{2} & \text{for } \theta_c > \frac{\pi}{2}. \end{cases} \tag{154}$$

Recalling that S corresponds to the integrand of (I) in (RHS) evaluated at $\eta = R_2$, we obtain that for large R_2 due to matching to (134)

$$\partial_\rho U_0^c = -\frac{1}{\gamma_0}\sqrt{2F(U_0^c)}, \tag{155}$$

which reveals that

$$\begin{aligned}\int_{-\infty}^{\infty} \left(\partial_\rho U_0^c\right)^2 \, d\rho &= -\frac{\sqrt{2}}{\gamma_0^2}\int_{-\infty}^{\infty} \sqrt{F(U_0^c)}\partial_\rho U_0^c \, d\rho \\ &= -\frac{\sqrt{2}}{\gamma_0}\int_1^{-1} \sqrt{F(t)} \, dt \quad = \quad \frac{1}{\gamma_0}\frac{4}{3}.\end{aligned} \tag{156}$$

Young-Herring condition in the anisotropic case

By merging the results for (LHS) and (RHS) in (141) we obtain

$$0 = \frac{4}{3}\left(-\gamma_0{}'(\theta_c)\sin\theta_c + \gamma_0(\theta_c)\cos\theta_c\right) - \frac{1}{\lambda_m}(\gamma_{VS} - \gamma_{FS}) \tag{157}$$

with $\theta_c \in (0, \pi)$, which is, after applying the correct mixing energy λ_m, the Young-Herring contact angle boundary condition as derived in Chapter 2.2.1. Note that since we may derive the contact angle condition on the right hand analogously, the same condition also holds at the right contact point.

Young's equation in the isotropic case

If the surface energy is isotropic, i.e. $\gamma = 1$, then (157) reduces to the Young's equation (48), if we notice that the film/vapor interface energy σ_{FV} in this case is given by the integral of the square of the gradient of the inner solution across the interface layer, that is, by λ_m times the integral in (156), see for example [80]; thus $\sigma_{FV} = 4\lambda_m/3$. Moreover, in the case of weak anisotropy, $\gamma + \gamma'' > 0$, equation (157) has a unique solution θ_c, since then, the right hand side is a strictly monotonically decreasing function of $\theta_c \in (0, \pi)$ as can be seen by taking the derivative with respect to θ_c.

3.4.3 *Balance of flux condition*

For the sake of completeness we also need a balance of flux condition which matches the flux of the boundary layer near Γ_w to the flux in the outer region. To this end let $\mathbf{J}^b$ be the flux in the boundary layer near Γ_w and let $\mathbf{J}^c$ be the flux in the contact line region. Similar as before, consider now a box R of size R_1 in the ξ-direction and R_2 in the η direction (see Fig. 9). The size will later be taken to infinity while still ensuring that it remains within the inner region, that is, $\varepsilon R_1 \ll 1$, $\varepsilon R_2 \ll 1$. By the divergence theorem and the no-flux condition at the wall we have that

$$\int_0^{R_2} \left[\mathbf{J}^c \cdot \mathbf{e}_\xi\right]_{-R_1/2}^{R_1/2} d\eta + \int_{-R_1/2}^{R_1/2} \mathbf{J}^c \cdot \mathbf{e}_\eta \Big|_{R_2} d\xi = 0. \tag{158}$$

On the one hand, the terms in the expansion of $\mathbf{J}^c \cdot \mathbf{e}_\xi|_\infty$ have to match with $\mathbf{J}^b \cdot \mathbf{e}_x$ away from the contact point $(x_c, 0)$, i.e.

$$\mathbf{J}^b \cdot \mathbf{e}_x = m(U^b)\partial_x M^b. \tag{159}$$

Since we may assume that for large R_1 we have $U_0^b \equiv \pm 1$, which implies $m(U_0^b) = 0$ as well as $m'(U_0^b) = 0$, and recalling that $M_0^b = 0$ we obtain that the expansions for $\mathbf{J}^b$ are zero up to at least $O(\epsilon^3)$. On the other hand, the terms in $\mathbf{J}^c \cdot \mathbf{e}_\eta|_\infty$ have to match with those in $\mathbf{J} \cdot \mathbf{e}_y|_0$. According to (65) we know that $\mathbf{J} \cdot \mathbf{e}_y$ in curvilinear coordinates reads

$$\mathbf{J} \cdot \mathbf{e}_y = m(U)\left[n_2\epsilon^{-1}\partial_\rho M(U) - \frac{n_1}{1+\epsilon\rho\kappa}\partial_s M(U)\right], \tag{160}$$

and since $M_0 \equiv 0$ and M_1, M_2 are independent of ρ, the dominant terms of (160) are of $O(\epsilon^2)$

$$\mathbf{J} \cdot \mathbf{e}_y = \epsilon^2 m(U_0)\left(n_2\partial_\rho M_3 - n_1\partial_s M_1\right) + O(\epsilon^3), \tag{161}$$

In total, therefore, the leading order condition that follows from (158) is

$$\begin{aligned} 0 &= \int_{-\infty}^{\infty} m(U_0)\left(n_2\partial_\rho M_3 - n_1\partial_s M_1\right)\Big|_{R_2} d\rho \\ &= C\partial_s\left[(\gamma_0 + \gamma_0'')\kappa\right]\int_{-\infty}^{\infty} m(U_0)d\rho\,, \end{aligned}$$

where C is a constant and we have used (123), (115) and also assumed to pass over in a similar way as in (149) in order to stay inside the box all the time. By virtue of (93), the integral is finite, thus

$$\partial_s\left[(\gamma_0 + \gamma_0'')\kappa\right] = 0 \tag{162}$$

at the contact line. Notice that via (115), this condition is equivalent to requiring the leading order tangential flux (from surface diffusion) along the interface Γ to be zero at the contact line.

3.5 DISCUSSION AND OUTLOOK

Recap of the main result

In the present chapter we have completed the two-dimensional phase-field model as generally derived in Chapter 2.1 with the intend to model the dewetting of a solid film from a solid substrate. The main goal was to establish the connection between the phase-field model and the corresponding sharp-interface model in the limit as $\varepsilon \to 0$, for a mobility where surface diffusion is recovered as the dominant driving mechanism. This requires an asymptotic analysis that incorporates multiple boundary and interfacial layers that occur in the sharp-interface limit as well as techniques of exponential matching, both in the isotropic and the anisotropic case.

Exponential matching away from the solid boundary

We established that by using exponential asymptotic matching the bi-quadratic mobility combined with the polynomial homogeneous free energy density yields the correct limiting model as $\varepsilon \to 0$. We note that this is in contrast to the frequently applied quadratic mobility, which leads to sharp-interface models, where a contribution from a non-linear, porous medium like bulk diffusion enters the driving force at the same order of magnitude as surface diffusion, as it also has previously been shown in [64].

Adjusted matching at the solid boundary

In addition, since the solid dewetting problem considered here includes boundary conditions at a solid substrate, another appropriate matching procedure has to be provided in order to derive the sharp interface limits at this solid boundary. We introduced another inner layer about the boundary Γ_w and presented an asymptotic analysis which refers to a particular geometry allowing to match the inner and outer layers without matching "into the substrate", which is not well-defined. The result is that the sharp interface limits of the boundary conditions at the substrate recover the Young-Herring equation for the contact angle, and Young's equation in the isotropic case.

Outlook

We also note that from liquid dewetting studies it is known that the, typically degenerate, mobility of the governing fourth order parabolic thin film equation does not only control the dewetting rates but also decides the morphology and scale of the contact line instability that arises eventually [3]. In principle, similar scenarios have to be explored here. Moreover, in combination with the anisotropic nature of the solid film, such as for example Si, the evolution of the contact line instability becomes particularly interesting and, according to experimental results [27], depends on the crystalline orientation relative to the contact line. For comparisons to realistic experimental results of dewetting solid films, such as crystalline Si films used for nanopatterning surfaces, the extension of the present phase field model to three space dimensions is desirable.

4

EXISTENCE OF SOLUTIONS TO THE ANISOTROPIC PHASE FIELD MODEL

4.1 EXISTENCE RESULTS FOR RELATED PHASE FIELD MODELS

The Cahn-Hilliard equation with degenerate mobility

Probably one of the most well-known examples for phase separation is the classical Cahn- Hilliard equation in the form

$$\frac{\partial u}{\partial t} = -\operatorname{div} \mathbf{j}, \tag{163a}$$

$$\mathbf{j} = -m(u)\nabla\mu, \tag{163b}$$

$$\mu = F'(u) - \gamma\Delta u, \tag{163c}$$

which originally was introduced by Cahn and Hilliard to study phase separation of binary fluids [16, 17]. Considering appropriate choices for $m(u)$ and $F(u)$ equation (163) can be identified as the isotropic case of the phase field equation (49), as studied in the previous chapter. At least, in order to model motion by surface diffusion, we need to assume that the diffusional mobility $m(u)$ is a non-negative function which vanishes at the pure phases, i.e. $m(u) = 0$ for $u = \pm 1$, as motivated in Section 3.1. On the one hand, this constitutes a mathematical difficulty since the a priori estimates, such as are commonly used in existence results, loose their information at points where the mobility degenerates. On the other hand, a degenerate mobility may be beneficial in order to show that solutions which initially take values in the interval $[-1, 1]$ will do so for all positive time. Note that this is is not generally true for fourth order parabolic equations without degeneracy since there is no comparison principle available.

Existence results for the degenerate Cahn-Hilliard equation

Considering present existence results for Cahn-Hilliard with degenerate mobility (163), the techniques introduced in the papers by Elliott and Garcke [32] and by Bernis and Friedman [4] have proven to be extremely useful. In both papers the general procedure is to replace (163) by a family of regularized problems with smooth solutions u_δ, establish particular a priori bounds and show that the approximate solutions u_δ converge to solutions of the original problem as $\delta \to 0$. In [32], for example, the degenerate mobility $m(u)$ is approximated by a strictly positive mobility $m_\delta(u)$ which satisfies $m_\delta \to m$, as $\delta \to 0$. The resulting parabolic problem is non-degenerate and provides global and smooth solutions u_δ. With the help of appropriate a priori estimates it is then shown that the integral of u_δ in the region where $|u| > 1$ converges to zero as m_δ approaches m, which yields $|u| \leq 1$ in the limit. In fact, it can be shown that solutions to (163) with sufficiently strong degenerated mobility preserve the strict inequalities $|u| < 1$ for all times $t \geq 0$.

The existence proof by Elliott and Garcke

In particular, Elliott and Garcke [32] exploit the dissipation of two particular functionals by solutions to (163) which provides the required regularity estimates. The first is the free energy functional

$$\mathcal{E}(u) := \int_\Omega F(u) + \frac{\gamma}{2}|\nabla u|^2 \, dx. \tag{164}$$

and the second the functional defined by

$$\mathcal{U}(u) := \int_\Omega \Phi(u), \qquad \text{where } \Phi''(u) = \frac{1}{\sqrt{m(u)}}, \tag{165}$$

also referred to as entropy functional. In particular, the functional $\mathcal{U}$ has become a key tool in order to provide the bound $|u| \leq 1$.

Variational alternative by Lisini, Matthes and Savaré

We note that there is an alternative approach to existence, proposed by Lisini, Matthes and Savaré [71], which exploits the variational structure of (163). A major advantage of this new approach is that essential properties of the solution, such as the bound $|u| \leq 1$, are automatically provided by the construction from so-called *minimizing movements* in the energy landscape, where the terminology *minimizing movement* is due to De Giorgi [38]. Observing that (163) is in the shape of a gradient flow for $\mathcal{E}$ with respect to a Wasserstein-like transport metric, weak solutions may be obtained as curves of maximal slope. Unfortunately, the main assumption in [71] is that the mobility is a concave function of u which is not satisfied by the present bi-quadratic choice (51).

The anisotropic Cahn-Hilliard equation

The Cahn-Hilliard equation, even with degenerate mobility, has been studied intensively in the past [2, 4, 32, 71, 91], but little mathematical analysis has been done for the case where the surface energy is anisotropic, i.e.

$$\frac{\partial u}{\partial t} = -\operatorname{div} \mathbf{j}, \tag{166a}$$

$$\mathbf{j} = -m(u)\nabla \mu, \tag{166b}$$

$$\mu = F'(u) - \epsilon^2 \operatorname{div}\left(A(\nabla u)\nabla u\right), \tag{166c}$$

where

$$A(\mathbf{n}) = \begin{bmatrix} \gamma(\theta_{\mathbf{n}})^2 & -\gamma'(\theta_{\mathbf{n}})\gamma(\theta_{\mathbf{n}}) \\ \gamma'(\theta_{\mathbf{n}})\gamma(\theta_{\mathbf{n}}) & \gamma(\theta_{\mathbf{n}})^2 \end{bmatrix} \tag{167}$$

and $\theta_{\mathbf{n}}$ denotes the angle between the x-axis and the vector $\mathbf{n}$. The function $\gamma(\theta)$ is given by

$$\gamma(\theta) = 1 + G\cos(n\theta), \tag{168}$$

where G is a positive constant and n an integer corresponding to the number of orientations in the symmetry. An existence result for a different model which also includes (167) is provided by Burman and Rappaz [12]. They consider an anisotropic phase field model for the isothermal solidification of a binary alloy due to Warren-Boettinger

An anisotropic phase field model considered by Burman and Rappaz

which in the special case of only one concentration can be identified as an anisotropic version of the well-known Allen-Cahn equation

$$\frac{\partial u}{\partial t} = F'(u) - \epsilon^2 \operatorname{div}\left(A(\nabla u)\nabla u\right). \tag{169}$$

Burman and Rappaz [12] show that the behavior of the anisotropic second-order operator is strongly depending on the size of G. In particular, for small values of G the anisotropic free energy functional

$$\mathcal{E}(u) := \int_\Omega F(u) + \epsilon^2 \frac{\gamma(\theta_{\nabla u})^2}{2} |\nabla u|^2 \, dx \tag{170}$$

is convex with respect to ∇u which implies monotonicity and hemicontinuity of the Eulerian operator. Exploiting the literature, see for instance [100], the existence proof is then essentially based on the theory for monotone operators. Note that the physical interpretation of small values of G is that no corners or sharp edges develop on the surface.

Overview of this chapter

Motivated by [12], we will also exploit the properties of the anisotropy operator (167), but since our equation is of fourth order, we additionally need some higher order bounds on $\operatorname{div}(A(\nabla u)\nabla u)$. All necessary properties are collected in Section 4.3.1. In 4.3.3 we prove the existence of approximate solutions to the regularized Cahn-Hilliard equation, i.e. with a regularized mobility which is bounded away from zero. This result is used in Section 4.3.4 to establish the existence of approximate solutions to the degenerate problem, where we derive energy estimates for the approximate solutions, which enable us to pass to the limit in the approximate equation.

Before presenting the existence result, we give a brief overview of selected concepts from the theory of partial differential equations which will be particularly important for the following theory.

4.2 PRELIMINARIES: CONCEPTS FROM THE THEORY OF PARTIAL DIFFERENTIAL EQUATIONS

Recommended literature

There is much standard literature which may be proposed as introduction to the theory of partial differential equations at this point. In view of the basic concepts, such as weak derivatives, partial integration, standard Sobolev spaces or completeness which are assumed as basic knowledge for the following theory, we refer to the books by Evans [34], Robinson [97] and Zeidler [119]. Furthermore, since we will apply some concepts from the calculus of variations as well as the theory of monotone and weakly continuous mappings, we recommend the books by Dacorogna [21] and Roubícek [98]. The aim of this section is to introduce selected definitions, theorems and inequalities which will be very important or frequently used in the subsequent existence

proof. Corresponding proves or the complete theory can be found in the literature mentioned above.

In the following, let H be a real Banach space with norm $\|\cdot\|_H$ and let $|\cdot|$ be the standard (Euclidean) norm on $\mathbb{R}^N$. If H is a Hilbert space, we denote the corresponding scalar product by $(\cdot,\cdot)_H$ and will use the short form $(\cdot,\cdot)$ if equations get to long otherwise.

4.2.1 *Dual spaces and compact embeddings*

The *Dual space* of H is the set of all linear functionals acting on H and it is denoted by H'. A functional $f \in H'$ maps from H to $\mathbb{R}$. Its norm is defined as

$$\|f\|_{H'} := \sup_{x\in H, x\neq 0} \frac{|f(x)|}{\|x\|_H}.$$

Note that the notation $\langle f, x\rangle$ or $\langle f, x\rangle_{H',H}$, the so-called dual pairing, is frequently applied instead of $f(x)$.

Dual spaces of Lebesgue spaces

Considering the particular example of the Lebesgue spaces $L^p(\Omega)$, where Ω is an bounded open and connected subset of $\mathbb{R}^N$, with $p \in (1,\infty)$, the corresponding dual spaces are $(L^p(\Omega))' \simeq L^q(\Omega)$ (where $\simeq$ denotes an isometry, so that the spaces can be identified with each other). The indices are conjugate, i.e. $1/p + 1/q = 1$. In the particular case $p = q = 2$ the dual and the underlying Hilbert space $L^2(\Omega)$ are the same. The Riesz representation theorem generalizes this result.

Lemma 4.2.1 (Riesz representation theorem) *Let H be a Hilbert space with dual H'. Then H' can be identified with H in the following sense: For any $u' \in H'$ there exists a unique element $u \in H$ such that*

$$u'(v) = (u, v)_H \quad \forall v \in H$$

and

$$\|u'\|_{H'} = \|u\|_H.$$

Weak convergence

A sequence $(x_n)_n \subset H$ in a Hilbert space H *converges weakly* to $x \in H$ if it converges in the scalar product with any test function $y \in H$ that is bounded in H, i.e.

$$(x_n, y)_H \to (x, y)_H$$

and the notation

$$x_n \rightharpoonup x$$

is used.

Embeddings

It will be necessary to relate certain spaces to each other in order to establish weak convergence out of boundedness. This is stated in a

lemma which works for three Banach spaces X, Y and Z, where X is *compactly embedded* in Y and Y is *continuously embedded* in Z. Therefore, in order to formulate the actual statement we need to clarify what the particular embeddings mean.

A Banach space X is *continuously embedded* in a Banach space Y and we write

$$X \hookrightarrow Y,$$

if $X \subset Y$ and there exists a constant $C \in \mathbb{R}$ such that the following continuity condition is fulfilled

$$\|u\|_Y \leq C\|u\|_X, \quad \forall u \in X.$$

Compact embeddings are now special continuous embeddings. A Banach space X is *compactly embedded* in a Banach space Y and we write

$$X \hookrightarrow\hookrightarrow Y,$$

if the following two conditions are satisfied

i) X is continuously embedded in Y, i.e. $X \hookrightarrow Y$

ii) for every bounded sequence $(u_n)_n \subset X$ there exists an element $u \in Y$ and a converging subsequence $(v_l)_l \subset (u_k)_k$ such that

$$v_l \to u \quad \text{in } Y.$$

The next theorem provides a compact embedding concerning Sobolev spaces which will prove particularly useful in the following.

Lemma 4.2.2 (Rellich-Kondrachov embedding theorem) *Suppose* $1 \leq p < n$. *Then*

$$W^{1,p}(\Omega) \hookrightarrow\hookrightarrow L^q(\Omega)$$

for each $1 \leq q < p^*$, *where* $p^* = \frac{pn}{n-p}$.

4.2.2 *Spaces involving time*

Solutions of time-dependent partial differential equations can be viewed as trajectories in infinite dimensional phase spaces

$$u : [0, T] \to X, \quad u = u(t),$$

where X is a Banach space, typically L^p or H^k, where H^k denotes the Sobolev space $W^{k,2}$. This approach motivates to define Banach space valued function spaces

L^p spaces involving time

$$L^p(0, T; X)$$

that are Banach spaces themselves. These contain the functions whose X-norm is p-integrable

$$\|u\|_{L^p(0,T;X)} := \left(\int_0^T \|u\|_X^p \, dt \right)^{\frac{1}{p}} < \infty.$$

For $X = L^p(\Omega)$, where $\Omega \subset \mathbb{R}^N$ is bounded subset of $\mathbb{R}^N$, the spaces simplify to

$$L^p(0,T;L^p(\Omega)) = L^p([0,T]\times\Omega).$$

Another common notation is $C([0,T],X)$, which can be used when the functions change continuously in time. In particular, this applies to the next result.

Lemma 4.2.3 *Let X and Y be Banach spaces with $X \hookrightarrow\hookrightarrow Y \hookrightarrow X'$ and let*

$$u \in L^2(0,T;X), \qquad \partial_t \in L^2(0,T;X'),$$

then

$$u \in C([0,T],Y).$$

The next lemma shows that bounded sequences have convergent subsequences in certain cases, similarly as the theorem by Bolzano-Weierstrass which is stated for finite-dimensional spaces.

Lemma 4.2.4 *(Reflexive weak compactness) Let $(u_n)_n$ be a bounded sequence in the reflexive Banach space X. Then there exists a subsequence that converges weakly in X.*

Some notes on reflexivity

Reflexive means that X is isometrically isomorph to X'', the dual of the dual space. Hilbert spaces are always reflexive. Also the Lebesgue spaces $L^p, p \in (1,\infty)$ are reflexive, with dual space L^p, where q is conjugate to p, i.e. $1/p + 1/q = 1$. Although L^1 has the dual L^∞, these spaces are not reflexive.

This result shows that once boundedness of a sequence in a Hilbert space or in one of the L^p spaces is proved, the extraction of a weakly convergent subsequence is possible.

4.2.3 *Some inequalities*

There are certain inequalities which are frequently used in existence theory. The most important ones are repeated here and we refer to the books by Evans [34] and Zeidler [119] reproducing the proofs of the inequalities.

Lemma 4.2.5 (Poincaré's inequality) *Let Ω be a bounded open connected subset of $\mathbb{R}^N$ with a Lipschitz boundary. Then there exists a constant C, only depending on Ω and p, such that for $u \in W^{1,p}(\Omega)$ and $1 \le p \le \infty$ we have*

$$\|u - u_\Omega\|_{L^p(\Omega)} \le C\|\nabla u\|_{L^p(\Omega)},$$

where

$$u_\Omega := \frac{1}{|\Omega|}\int_\Omega u(x)\,dx.$$

In order to establish useful estimates a lot of technical calculations have to be carried out, where the following inequalities will come into use.

Young's inequality

Let $1 < p, q < \infty$ satisfying $\frac{1}{p} + \frac{1}{q} = 1$ and let $a, b \geq 0$. Then *Young's inequality* states that

$$ab \leq \frac{a^p}{p} + \frac{b^q}{q}.$$

Hölder's inequality

It can be used to prove *Hölder's inequality*

$$\int_\Omega |uv| dx \leq \|u\|_{L^p(\Omega)} \|v\|_{L^q(\Omega)},$$

which holds for all $u \in L^p(\Omega)$ and $v \in L^q(\Omega)$, and actually for $p, q \in [1, \infty]$.

Young's inequality with epsilon

Combining Young's inequality with Hölder's inequality and introducing an artificial epsilon, another useful inequality becomes

$$\|uv\|_{L^1(\Omega)} \leq \epsilon \|u\|^p_{L^p(\Omega)} + C(\epsilon) \|v\|^q_{L^q(\Omega)},$$

the so-called *Young's inequality with epsilon*, with the positive constant $C(\epsilon) = \left(\frac{1}{\epsilon p}\right)^{\frac{q}{p}} \frac{1}{q}$.

Now many useful tools from functional analysis are at hand, however, some more basic theory is necessary. The subsection is finished with an existence result for ODEs.

Lemma 4.2.6 (Peano) *Let D be a open subset of $\mathbb{R} \times \mathbb{K}^N$, $N \geq 1$, where $\mathbb{K}$ is either $\mathbb{R}$ or $\mathbb{C}$, and assume that $f : D \to \mathbb{K}^N$ is continuous. Then the initial value problem*

$$u'(t) = f(t, y), \quad u(0) = u_0$$

has a local solution, i.e. there exists an interval I, $0 \in I$, and at least one solution $u : I \to \mathbb{K}^N$ satisfying

$$u'(t) = f(t, u(t)), \quad u(0) = u_0,$$

for all $t \in I$.

4.2.4 *Preliminaries from the calculus of variations*

In order to deal with the strong non-linearity in the fourth order operator, we will use some concepts from the calculus of variations. The main result that we will apply (Theorem 3.23 in [21]) deals with the *weak lower semicontinuity* of a functional

weak lower semicontinuity

$$J(u) := \int_\Omega f(x, u(x), \nabla u(x)) \, dx,$$

meaning that

$$\liminf_{\nu\to\infty} J(u_\nu) \geq J(u),$$

for every sequence $u_\nu \rightharpoonup u$ in $W^{1,p}$.

Convex and Carathéodory functions

Regarding the conditions of the theorem, we recall that a function $f : \mathbb{R}^N \to \mathbb{R} \cup +\infty$ is said to be *convex*, if

$$f(tx + (1-t)y) \leq tf(x) + (1-t)f(y),$$

for every $x, y, \in \mathbb{R}^N$ and every $t \in [0,1]$.

Moreover we will need to verify that $f : \Omega \times \mathbb{R}^m \times \mathbb{R}^M \to \mathbb{R}, f = f(x,u,\xi)$ is a *Carathéodory function*, which entails that

(i) $(u,\xi) \to f(x,u,\xi)$ is continuous for almost every $x \in \Omega$

(ii) $x \to f(x,u,\xi)$ is measurable for every $(u,\xi) \in \mathbb{R}^m \times \mathbb{R}^M$,

due to Definition 3.5 and Remark 3.6 in [21].

The result (Theorem 3.23 in [21]) states, roughly speaking, that the functional I is weakly lower semicontinuous if and only if $\xi \to f(x,u,\xi)$ is *convex*, and the explicit version reads:

Coercivity condition

Lemma 4.2.7 *Let $f : \Omega \times \mathbb{R}^m \times \mathbb{R}^M \to \mathbb{R} \cup \{+\infty\}$ be a Carathéodory function satisfying*

$$f(x,u,\xi) \geq \langle a(x); \xi\rangle + b(x) + c|u|^p \tag{171}$$

for almost every $x \in \Omega$, for every $(u,\xi) \in \mathbb{R}^m \times \mathbb{R}^M$ for some $a \in L^{q'}(\Omega;\mathbb{R}^M)$, $1/q + 1/q' = 1$, $b \in L^1(\Omega), c \in \mathbb{R}$ and where $\langle\cdot;\cdot\rangle$ denotes the scalar product in $\mathbb{R}^M$. Let

$$I(u,\xi) := \int_\Omega f(x,u(x),\xi(x))\,dx.$$

Assume that $\xi \to f(x,u,\xi)$ is convex and that

$$u_\nu \to u \text{ in } L^p(\Omega;\mathbb{R}^m) \quad \text{and } \xi_\nu \rightharpoonup \xi \text{ in } L^q(\Omega;\mathbb{R}^M).$$

Then

$$\liminf_{\nu\to\infty} J(u_\nu,\xi_\nu) \geq J(u,\xi).$$

Gateaux derivative

Finally we note that the *Gateaux derivative* of a functional $F : X \to Y$, where X and Y are Banach spaces, at $u \in X$ in the direction $\Psi \in X$ is defined by

$$d\hat{F}(u,\Psi) := \lim_{t\to 0} \frac{\hat{F}(u+t\Psi) - \hat{F}(u)}{t} = \frac{d}{dt}\hat{F}(u+t\Psi)|_{t=0}$$

if the limit exists. In the special case that $Y = \mathbb{R}$, the Gateaux derivative coincides with the definition of the variational derivative.

4.2.5 *Monotone or weakly continuous mappings*

A powerful approach to non-linear partial differential equations relies on the theory of monotone and weakly continuous mappings. Note that in the following we will write $\langle \cdot, \cdot \rangle$ instead of $\langle \cdot, \cdot \rangle_{H',H}$ for brevity.

Monotone operators

An operator $\mathscr{A} : H \to H'$ is *monotone* if

$$\langle \mathscr{A}(u) - \mathscr{A}(v), u - v \rangle \geq 0,$$

for all $u, v \in H$.

Different continuity modes

Observing that the definitions of the particular modes of continuity differ in the literature, we decided to apply the definitions provided in the book by Roubícek [98], i.e. we say that an operator $\mathscr{A} : H \to H'$ is *hemicontinuous* if the function

$$t \mapsto \langle \mathscr{A}(u + tv), w \rangle \tag{172}$$

is continuous for all $u, v, w \in H$. In other words $\mathscr{A}$ is directionally weakly continuous. In the special case that (172) is only continuous for $v = w$, we say that $\mathscr{A}$ is *radially continuous*.

In view of Lemma 2.16 in [98] and corresponding definition of "demicontinuity" given in [98], we conclude the following lemma.

Lemma 4.2.8 *Radially continuous monotone mappings are also hemicontinuous.*

Monotone mappings with radial continuity properties are a special class of pseudomonotone mappings, and in particular provide the opportunity to easily identify limits by applying the following common trick (see for example Lemma 2.13 in [98]).

Lemma 4.2.9 (Minty's Trick) *Let $\mathscr{A} : H \to H'$ be radially continuous and let*

$$\langle f - \mathscr{A}(v), u - v \rangle \geq, 0$$

for any $v \in H$. Then

$$f = \mathscr{A}(u).$$

4.3 EXISTENCE OF SOLUTIONS TO THE ANISOTROPIC DEGENERATE CAHN-HILLIARD EQUATION

Properties of the anisotropy operator

The main difficulty in the following existence proof, compared to the result in reference [32], resides in the strongly non-linear fourth-order operator. Motivated by [12], we will exploit that the impact of the anisotropy depends on the size of G and that for small values of G the energy functional (170) stays convex with respect to ∇u. This implies

monotonicity and hemicontinuity of $u \mapsto \langle \operatorname{div}(A(\nabla u)\nabla u), \nabla \cdot \rangle$, which will be very useful in situations where we have to identify limits of approximate problems. Furthermore, since the differential equation (166) is of fourth order we will additionally need some higher order bounds on $\operatorname{div}(A(\nabla u)\nabla u)$. These are in particular necessary in order to recover the energy estimates (or a priori estimates) as posed in [32] for the anisotropic case.
In the next section we collect all the crucial properties of the anisotropic operator. Note that the former may also be found in [12].

4.3.1 *Extending the preliminary results of Burman and Rappaz*

NOTATION Throughout this and the following sections of this chapter we assume that Ω is an open, bounded domain in $\mathbb{R}^2$, with a Lipschitz boundary $\partial\Omega$. The $L^2(\Omega)$-scalar product will be denoted by $(\cdot,\cdot)$ and $Q_T = \Omega \times (0,T)$ will denote the space-time domain for some $T > 0$. For brevity we write H^1 instead of $H^1(\Omega)$ in the indices of corresponding norms or scalar products. We omit the differential "dx" at the end of an integral in order to save space.

The results of this section refer to the particular representation (168) of the anisotropic surface energy and the corresponding matrix representation (167) of the anisotropy in the partial differential equation. We recall that G represents the strength of the anisotropy and n corresponds to symmetry type.

Properties of the anisotropic operator

Lemma 4.3.1 *If*

$$G < \frac{1}{n^2 - 1}, \tag{173}$$

then

(i) the functional

$$\hat{E}(\mathbf{v}) := \int_\Omega \frac{\gamma(\theta_{\mathbf{v}})^2}{2} |\mathbf{v}|^2$$

is strictly convex in $\mathbf{v}$, $\forall \mathbf{v} \in [L^2(\Omega)]^2$.

(ii) the Gateaux derivative of the potential

$$\tilde{E}(u) = \int_\Omega \frac{\gamma(\theta_{\nabla u})^2}{2} |\nabla u|^2$$

exists for each $u \in H^1(\Omega)$ *and is given by*

$$\tilde{E}'(u)v = \int_\Omega A(\nabla u)\nabla u \cdot \nabla v$$

(iii) the anisotropic operator satisfies the following upper and lower bounds

$$(1-G)^2 |u|_{H^1}^2 \leq \int_\Omega A(\nabla u)|\nabla u|^2 \, dx \leq (1+G)^2 |u|_{H^1}^2.$$

Proof. See Section 4 in [12]. □

Properties (i) and (ii) turn out to be useful in order to prove the following lemma.

Lemma 4.3.2 *The mapping*

$$u \in V \mapsto \langle A(\nabla u)\nabla u, \nabla \cdot \rangle_{(H^1)',H^1} \in (H^1(\Omega))'$$

is monotone and hemicontinuous.

Proof. From Lemma 4.8 in [100], we know that $u \in H^1(\Omega) \mapsto \langle A(\nabla u)\nabla u, \nabla \cdot \rangle \in (H^1(\Omega))'$ is monotone and radially continuous in the sense of the definition given in Section 4.2.5. Using Lemma 4.2.8 then gives hemicontinuity as well.
□

Higher order bounds for the anisotropic part

Since equation (166) is of fourth order, we additionally need some higher order bounds on $\operatorname{div}(A(\nabla u)\nabla u)$. This requires the assumption that G is sufficiently small such that at least (173) holds true. We will not give a particular bound for G as the determination of a greatest possible value for G is very technical and not necessary for the scope of our work. We only need to know that this bound exists. The second assumption is that $u_{xy}^2 - u_{xx}u_{yy}$ has zero mean value on Ω, i.e.

$$\int_\Omega u_{xy}^2 - u_{xx}u_{yy} = 0. \tag{174}$$

This assumption may look artificial at first sight, but realizing that phase field functions u which are constant on $\partial\Omega$ naturally fulfill (174) according to partial integration, we conclude that assumption (174) is no considerable restriction. In particular the eigenfunctions of the Laplace operator on a rectangular domain with Neumann boundary conditions obviously satisfy (174), which matches the model assumptions proposed in Chapter 2.1, i.e. to we consider a rectangular domain Ω.

The following lemma states the particular bounds on $\operatorname{div}(A(\nabla u)\nabla u)$, which will be of essential importance in the existence proof.

Lemma 4.3.3 *Let $u \in H^2(\Omega)$ and $\operatorname{div}(A(\nabla u)\nabla u) \in L^2(\Omega)$. Assume that $u_{xy}^2 - u_{xx}u_{yy}$ has zero mean value, i.e. (174) is satisfied. Then there exists $0 < G_0 \leq 1/(n^2-1)$ such that for all $G \leq G_0$ there exists a constant $C(n,G) > 0$, only depending on n and G, such that*

$$0 \leq \int_\Omega (\operatorname{div}(A(\nabla u)\nabla u))^2 \leq C(n,G) \int_\Omega \operatorname{div}(A(\nabla u)\nabla u)\Delta u.$$

Calculating the partial derivatives of θ

Proof. Exploiting the particular representation of θ, i.e.

$$\theta(\nabla u) = \operatorname{atan2}\left(u_y, u_x\right)$$

we have

$$\theta_x = \frac{u_{yx}u_x - u_y u_{xx}}{|\nabla u|^2}, \qquad \theta_y = \frac{u_{yy}u_x - u_y u_{xy}}{|\nabla u|^2}.$$

On the one hand, we obtain

$$\nabla\theta \cdot \begin{pmatrix} -u_y \\ u_x \end{pmatrix} = \frac{1}{|\nabla u|^2}\left(-2u_{yx}u_x u_y + u_y^2 u_{xx} + u_{yy}u_x^2\right),$$

where "$\cdot$" denotes the standard Euclidean scalar product of two vectors. Note that we assumed that $u_{xy} = u_{yx}$, which is admissible, since Ω is bounded and hence u may be represented through the linear combination of infinitely differentiable functions, such as the eigenfunctions of the Laplace operator.
On the other hand we have

$$\begin{aligned}
|\nabla\theta|^2|\nabla u|^2 &= \frac{1}{|\nabla u|^2}\left(\left(u_{yx}u_x - u_y u_{xx}\right)^2 + \left(u_{yy}u_x - u_y u_{xy}\right)^2\right) \\
&= \frac{1}{|\nabla u|^2}\left(-2u_{xy}u_x u_y \Delta u + u_{xy}^2|\nabla u|^2 + u_y^2 u_{xx}^2 + u_x^2 u_{yy}^2\right) \\
&= \frac{1}{|\nabla u|^2}\left(-2u_{yx}u_x u_y + u_y^2 u_{xx} + u_{yy}u_x^2\right)\Delta u + u_{xy}^2 - u_{xx}u_{yy},
\end{aligned}$$

which together reveals the relation

$$|\nabla\theta|^2|\nabla u|^2 = \left(\nabla\theta \cdot \begin{pmatrix} -u_y \\ u_x \end{pmatrix}\right)\Delta u + u_{xy}^2 - u_{xx}u_{yy}.$$

Moreover, denoting the angle between $\nabla\theta$ and ∇u by α, we have

$$\begin{aligned}
(\nabla\theta \cdot \nabla u) &= \cos(\alpha)\ |\nabla\theta||\nabla u|, \\
\left(\nabla\theta \cdot \begin{pmatrix} -u_y \\ u_x \end{pmatrix}\right) &= \cos(\frac{\pi}{2} - \alpha)\ |\nabla\theta||\nabla u| = \sin(\alpha)\ |\nabla\theta||\nabla u|,
\end{aligned} \tag{175}$$

which gives

$$\left(|\nabla\theta||\nabla u|\right)^2 = \sin(\alpha)\Delta u\ |\nabla\theta||\nabla u| + u_{xy}^2 - u_{xx}u_{yy}$$

and consequently

$$\left(|\nabla\theta||\nabla u|\right)_{1,2} = \frac{1}{2}\sin(\alpha)\Delta u \pm \sqrt{\frac{1}{4}\sin^2(\alpha)(\Delta u)^2 + u_{xy}^2 - u_{xx}u_{yy}}.$$

Observing that $|\nabla\theta||\nabla u|$ is positive and real and $x \in \mathbb{R}^2 \to |x|$ is a surjective mapping we may conclude that only

$$|\nabla\theta||\nabla u| = \frac{1}{2}\sin(\alpha)\Delta u + \sqrt{\frac{1}{4}\sin^2(\alpha)(\Delta u)^2 + u_{xy}^2 - u_{xx}u_{yy}} \tag{176}$$

is a reasonable solution.
Consider now $\operatorname{div}(A(\nabla u)\nabla u)$ and apply the representation (175)

$$\begin{aligned}\operatorname{div}(A(\nabla u)\nabla u) &= \operatorname{div}(\gamma^2\nabla u) + \operatorname{div}\left(\gamma\gamma'\begin{pmatrix}-u_y\\ u_x\end{pmatrix}\right)\\ &= \gamma^2\Delta u + 2\gamma\gamma'\,(\nabla\theta\cdot\nabla u) + ((\gamma')^2+\gamma\gamma'')\left(\nabla\theta\cdot\begin{pmatrix}-u_y\\ u_x\end{pmatrix}\right)\\ &= \gamma^2\Delta u + \Bigg(\underbrace{2\gamma\gamma'\cos(\alpha) + ((\gamma')^2+\gamma\gamma'')\sin(\alpha)}_{=:c_1(\alpha,\theta,G)}\Bigg)\,|\nabla\theta||\nabla u|\end{aligned}$$

where $c_1(\alpha,\theta,G)$ is uniformly bounded and satisfies

$$\begin{aligned}\gamma^2 + c_1(\alpha,\theta,G)\sin\alpha &= \gamma^2 + 2\gamma\gamma'\cos(\alpha)\sin(\alpha) + ((\gamma')^2+\gamma\gamma'')\sin^2(\alpha)\\ &= \underbrace{(\gamma\cos(\alpha)+\gamma'\sin(\alpha))^2}_{\geq 0} + (\gamma\underbrace{(\gamma+\gamma'')}_{>0})\,\underbrace{\sin^2(\alpha)}_{\geq 0}.\end{aligned} \tag{177}$$

Consequently we have

$$\gamma^2 + \frac{c_1}{2}(\alpha,\theta,G)\sin\alpha \geq \frac{\gamma^2}{2} > 0, \tag{178}$$

which we keep in mind for the following estimates.

Representation for $\operatorname{div}(A(\nabla u)\nabla u)$

Exploiting (176) and applying short forms, i.e. c_1 for $c_1(\alpha,\theta,G)$ and c_2 for $c_2(\alpha,\theta,G)$, we then have

$$\begin{aligned}\operatorname{div}(A(\nabla u)\nabla u) = &\left(\gamma^2 + \frac{c_1}{2}\sin(\alpha)\right)\Delta u\\ &+ c_1\sqrt{\frac{1}{4}\sin^2(\alpha)(\Delta u)^2 + u_{xy}^2 - u_{xx}u_{yy}}.\end{aligned} \tag{179}$$

Multiplying (179) with $\Delta u \in H^1(\Omega)$ and integrating over Ω we have

$$\begin{aligned}\int_\Omega \operatorname{div}(A(\nabla u)\nabla u)\,\Delta u &= \int_\Omega \left(\gamma^2 + \frac{c_1}{2}\sin(\alpha)\right)(\Delta u)^2\\ &\quad + \int_\Omega c_1\Delta u\sqrt{\frac{1}{4}\sin^2(\alpha)(\Delta u)^2 + u_{xy}^2 - u_{xx}u_{yy}}\\ &\geq \int_\Omega \left(\gamma^2 + \frac{c_1}{2}\sin(\alpha)\right)(\Delta u)^2\\ &\quad - \int_\Omega |c_1\Delta u|\sqrt{\frac{1}{4}\sin^2(\alpha)(\Delta u)^2 + u_{xy}^2 - u_{xx}u_{yy}}.\end{aligned} \tag{180}$$

Concerning the last integral we may deduce by applying Young's inequality with $\epsilon_Y > 0$

$$\begin{aligned}\int_\Omega |c_1\Delta u|\sqrt{\frac{1}{4}\sin^2(\alpha)(\Delta u)^2 + u_{xy}^2 - u_{xx}u_{yy}} &\leq \epsilon_Y\int_\Omega |c_1\Delta u|^2\\ &\quad + \frac{1}{4\epsilon_Y}\int_\Omega \frac{1}{4}\sin^2(\alpha)(\Delta u)^2 + u_{xy}^2 - u_{xx}u_{yy}\\ &\leq \left(\epsilon_Y C_1 + \frac{1}{8\epsilon_Y}\right)\int_\Omega |\Delta u|^2,\end{aligned} \tag{181}$$

where $C_1 := \max_{\alpha,\theta,G} c_1^2$ and we exploited that $u_{xy}^2 - u_{xx}u_{yy}$ has zero mean value.

Choosing ϵ in Young's inequality

Introducing the function

$$Y(\epsilon_Y) := \epsilon_Y C_1 + \frac{1}{8\epsilon_Y},$$

and calculating the derivative with respect to ϵ_Y

$$Y'(\epsilon_Y) := C_1 - \frac{1}{8\epsilon_Y^2},$$

reveals that Y has a minimum at $1/4\sqrt{C_1}$ and

$$Y\left(\frac{1}{4\sqrt{C_1}}\right) = \frac{3}{4}\sqrt{C_1} =: \epsilon_G > 0,$$

so that we can choose at least $\epsilon_Y = \epsilon_G$ in (181). Then, considering C_1 and exploiting the particular representation of γ, i.e. (168), we have

$$\begin{aligned}\sqrt{C_1} &= \max_{\alpha,\theta,G} \left(2\gamma\gamma'\cos(\alpha) + ((\gamma')^2 + \gamma\gamma'')\sin(\alpha)\right)\\ &\leq |2\gamma\gamma'| + (\gamma')^2 + |\gamma\gamma''|\\ &\leq Gn((2+n) + Gn),\end{aligned}$$

which basically reveals that C_1 tends to zero for sufficiently small G. On the other hand, (178) implies boundedness from below of $\gamma^2 + \frac{c_1}{2}\sin(\alpha)$ by a positive constant. Now, going back to (180), we are in the position to deduce that for G sufficiently small we may choose ϵ_G such that

$$0 < \epsilon_G \leq \left(\gamma^2 + \frac{c_1}{2}\sin(\alpha)\right)$$

for all α, θ and consequently

$$\int_\Omega \operatorname{div}\left(A(\nabla u)\nabla u\right)\Delta u \geq \int_\Omega \left(\gamma^2 + \frac{c_1}{2}\sin(\alpha)\right)(\Delta u)^2 - \epsilon_G \int_\Omega (\Delta u)^2 \geq 0. \tag{182}$$

We now consider the right hand side of the inequality in Lemma 4.3.3. Multiplying (179) with $\operatorname{div}(A(\nabla u)\nabla u)$ and integrating over Ω we obtain

$$\begin{aligned}0 &\leq \int_\Omega \left(\operatorname{div}\left(A(\nabla u)\nabla u\right)\right)^2\\ &= \int_\Omega \left(\gamma^2 + \frac{c_1}{2}\sin(\alpha)\right)\operatorname{div}(A(\nabla u)\nabla u)\Delta u\\ &\quad + \int_\Omega \operatorname{div}(A(\nabla u)\nabla u)c_1\sqrt{\frac{1}{4}\sin^2(\alpha)(\Delta u)^2 + u_{xy}^2 - u_{xx}u_{yy}}\\ &\leq \int_\Omega \left(\gamma^2 + \frac{c_1}{2}\sin(\alpha)\right)\operatorname{div}(A(\nabla u)\nabla u)\Delta u\\ &\quad + \epsilon_Y \int_\Omega |\operatorname{div}(A(\nabla u)\nabla u)c_1|^2 + \frac{1}{4\epsilon_Y}\int_\Omega \frac{1}{4}\sin^2(\alpha)(\Delta u)^2,\end{aligned} \tag{183}$$

where we again exploited that $u_{xy}^2 - u_{xx}u_{yy}$ has zero mean value. Choosing $\epsilon_Y = 1/(C_1+1)$ and observing that from (182) we know that there exists a constant $C > 0$ such that

$$\int_\Omega |\Delta u|^2 \leq C \int_\Omega \operatorname{div}(A(\nabla u)\nabla u)\Delta u,$$

we obtain from (183)

$$\begin{aligned} 0 &\leq \int_\Omega \left(\operatorname{div}\left(A(\nabla u)\nabla u\right)\right)^2 \\ &\leq \int_\Omega C \operatorname{div}(A(\nabla u)\nabla u)\Delta u + \frac{C_1}{C_1+1}\int_\Omega |\operatorname{div}(A(\nabla u)\nabla u)|^2. \end{aligned}$$

Note that $C > 0$ is now a different constant which we still denote the same to simplify matters. Finally we conclude that

$$\frac{1}{C_1+1}\int_\Omega \left(\operatorname{div}\left(A(\nabla u)\nabla u\right)\right)^2 \leq \int_\Omega C \operatorname{div}(A(\nabla u)\nabla u)\Delta u,$$

which completes the proof. □

We are now in a position to attempt an existence result.

4.3.2 *Existence theorem*

Problem assumptions

In this section we formulate the existence result which will be proved in the following. The result refers to the anisotropic Cahn-Hilliard equation (166) on a rectangular open subset $\Omega \subset \mathbb{R}^2$ with boundary conditions

$$\mathbf{n}_\Omega \cdot \nabla u = 0, \tag{184a}$$
$$m(u)\mathbf{n}_\Omega \cdot \nabla \mu = 0, \tag{184b}$$

on $\partial\Omega$, where $\mathbf{n}_\Omega$ is the unit outward pointing normal vector onto Ω. Note that $A(\mathbf{n})$ is the anisotropy matrix defined by (167). We recall that we consider the polynomial homogeneous free energy (50) and the bi-quadratic degenerated mobility (51). The energy of the system is hence given by (170) and in order to derive appropriate energy estimates similar as in the proof by Elliott and Garcke [32] we introduce the function

$$\Phi : (-1,1) \to \mathbb{R}_0^+,$$

defined by

$$\Phi''(u) = \frac{1}{\sqrt{m(u)}}, \quad \Phi'(0) = 0, \quad \text{and } \Phi(0) = 0.$$

The following theorem states the existence of a weak solution to the anisotropic Cahn-Hilliard equation with doubly degenerated mobility on an arbitrary interval $[0,T]$, for some $T \in \mathbb{R}^+$.

Theorem 4.3.4 *Suppose that (174) holds true and that G is sufficiently small, according to Lemma 4.3.3. Let $u_0 \in H^1(\Omega)$ with $|u_0| \leq 1$ a.e. and*

$$\int_\Omega (F(u_0) + \Phi(u_0)) \leq C, \qquad C \in \mathbb{R}^+.$$

Then there exists a pair of functions (u, μ) such that
$u \in L^\infty(0,T;H^1(\Omega)) \cap C([0,T];L^2(\Omega))$,
$u_t \in L^2(0,T;(H^1(\Omega))')$,
$u(0) = u_0$,
$\mu \in L^2(0,T;H^1(\Omega))$
which satisfies (166) in the following weak sense:

$$\int_0^T \langle \xi(t), u_t(t) \rangle_{H^1,(H^1)'} = -\int_{\Omega_T} m(u)\nabla\mu \cdot \nabla\xi \tag{185}$$

for all $\xi \in L^2(0,T;H^1(\Omega))$ and

$$\int_\Omega \mu\phi = \int_\Omega F'(u)\phi + \int_\Omega \epsilon^2 A(\nabla u)\nabla u \cdot \nabla\phi \tag{186}$$

for all $\phi \in H^1(\Omega)$ which fulfill $\mathbf{n}_\Omega \nabla\phi = 0$ on $\partial\Omega \times (0,T)$ and almost all $t \in [0,T]$.

Outline of the proof

In order to prove Theorem 4.3.4, we first show in Section 4.3.3 the existence of a solution to (166) with a mobility which is bounded away from zero. This result is used in Section 4.3.4 to establish the existence of approximate solutions to the degenerate problem. We derive energy estimates for the approximate solutions which enable us to pass to the limit in the approximate equation to get the existence of a weak solution as stated.

4.3.3 *The regularized problem*

Regularizing the mobility

In this section we study the anisotropic Cahn-Hilliard equation (166) with the regularized mobility $m_\delta(u)$ defined by

$$m_\delta(u) := \begin{cases} m(-1+\delta) & \text{for} \quad u \leq -1+\delta, \\ m(u) & \text{for} \quad u < 1-\delta, \\ m(1-\delta) & \text{for} \quad u \geq 1-\delta, \end{cases}$$

where $\delta \ll 1$ and we define $\Phi_\delta(u)$ such that

$$\Phi_\delta''(u) = \frac{1}{\sqrt{m_\delta(u)}}, \quad \Phi_\delta'(0) = 0, \quad \text{and } \Phi_\delta(0) = 0, \tag{187}$$

and point out that $\Phi_\delta(u) = \Phi(u)$ when $|u| \leq 1-\delta$. In a similar way we define $\Psi_\delta(u)$ such that

$$\Psi_\delta''(u) = \frac{1}{m_\delta(u)}, \quad \Psi_\delta'(0) = 0, \quad \text{and } \Psi_\delta(0) = 0, \tag{188}$$

which will prove usefull in order to derive appropriate bounds for the anisotropy operator.

We consider the anisotropic Cahn-Hilliard equation in the form

$$u_t = \nabla \cdot m_\delta(u)\nabla\mu, \tag{189}$$
$$\mu = F'(u) - \epsilon^2 \operatorname{div}(A(\nabla u)\nabla u) \tag{190}$$

with Neumann and no-flux boundary conditions

$$\mathbf{n}_\Omega \nabla u = 0, \quad \text{and} \quad m_\delta(u)\mathbf{n}_\Omega \nabla\mu = 0,$$

on $\partial\Omega \times (0,T)$ and observe that $m_\delta \in C(\mathbb{R}, \mathbb{R}^+)$ and there exist $m_1, M_1 > 0$ such that

$$m_1 \leq |m_\delta(u)| \leq M_1$$

for all $u \in \mathbb{R}$.

The following Theorem states the existence of weak solutions to the regularized problem. Note that for this result we do not need the additional assumptions yet, i.e. (174) and the more restrictive bound on G.

Theorem 4.3.5 *Suppose $u_0 \in H^1(\Omega)$ and that the anisotropy operator is weakly anisotropic, i.e. (173) is satisfied. Then there exists a pair of functions (u,μ) such that*
$u \in L^\infty(0,T;H^1(\Omega)) \cap C([0,T];L^2(\Omega))$,
$u_t \in L^2(0,T;(H^1(\Omega))')$,
$u(0) = u_0$,
$\mu \in L^2(0,T;H^1(\Omega))$
which satisfies (189) and (190) in the following weak sense:

$$\int_0^T \langle \xi(t), u_t(t)\rangle_{H^1,(H^1)'} = -\int_{\Omega_T} m_\delta(u)\nabla\mu \cdot \nabla\xi \tag{191}$$

for all $\xi \in L^2(0,T;H^1(\Omega))$ and

$$\int_\Omega \mu\phi = \int_\Omega F'(u)\phi + \int_\Omega \epsilon^2 A(\nabla u)\nabla u \cdot \nabla\phi \tag{192}$$

for all $\phi \in H^1(\Omega)$ and almost all $t \in [0,T]$.

The following proof and its structure is inspired by Elliott and Garcke [32]. However, the particular steps are more challenging due to the anisotropic operator.

Proof. In the first step of the proof we apply a Galerkin approxima- *Galerkin approximation*

tion. Let $\{\phi_i\}_{i\in\mathbb{N}}$ be the eigenfunctions of the Laplace operator with Neumann boundary conditions which is an orthogonal Basis of $H^1(\Omega)$. We suppose that the ϕ_i are normalized in the $L^2(\Omega)$ scalar product, i.e. $(\phi_i,\phi_j)_{L^2(\Omega)} = \delta_{ij}$ and that without loss of generality the first eigenfunction ϕ_1 corresponds to the eigenvalue $\lambda_1 = 0$, i.e. $\Delta\phi_1 = 0$. Consider the following Galerkin ansatz for u and μ

$$u^N(t,x) = \sum_{i=1}^N c_i^N(t)\phi_i(x), \quad \mu^N(t,x) = \sum_{i=1}^N d_i^N(t)\phi_i(x) \tag{193}$$

$$\int_\Omega \partial_t u^N \phi_j = -\int_\Omega m_\delta(u^N)\nabla\mu^N\cdot\nabla\phi_j \quad \text{for } j=1,..,N, \tag{194}$$

$$\int_\Omega \mu^N\phi_j = \int_\Omega \epsilon^2 A(\nabla u^N)\nabla u^N\cdot\nabla\phi_j + \int_\Omega F'(u^N)\phi_j \quad \text{for } j=1,..,N, \tag{195}$$

$$u^N(0) = \sum_{i=1}^N (u_0,\phi_i)_{L^2(\Omega)}\phi_i, \tag{196}$$

which leads to an initial value problem for a system of ordinary differential equations for $(c_1,..,c_N)$

$$\partial_t c_j^N = -\sum_{k=1}^N d_k^N \int_\Omega m_\delta\left(\sum_{i=1}^N c_i^N(t)\phi_i(x)\right)\nabla\phi_k\cdot\nabla\phi_j \tag{197}$$

$$\begin{aligned} d_j^N = &\int_\Omega \epsilon^2 A\left(\sum_{i=1}^N c_i^N(t)\nabla\phi_i(x)\right)\sum_{k=1}^N c_k^N(t)\nabla\phi_k(x)\cdot\nabla\phi_j \\ &+\int_\Omega F'\left(\sum_{i=1}^N c_i^N(t)\phi_i(x)\right)\phi_j \end{aligned} \tag{198}$$

$$c_j^N(0) = (u_0,\phi_j)_{L^2(\Omega)} \tag{199}$$

ODE system with continuous right hand side

which has to hold for $j = 1,...,N$. In what follows we will elucidate that d_j^N continuously depends on $c_1,...,c_N$ for every $j = 1,...,N$ which implies that the right hand side of (197) continuously depends on $c_1,...,c_N$ and the initial value problem (197)-(199) admits a local solution (see Lemma 4.2.6). Recalling that the mapping

$$u\in H^1(\Omega)\mapsto \langle A(\nabla u)\nabla u,\nabla\cdot\,\rangle\in (H^1(\Omega))'$$

is hemicontinuous implies that

$$t\in\mathbb{R}\mapsto \langle A(\nabla(u+tv))\nabla(u+tv),\nabla w\rangle$$

is continuous for all $u,v,w\in H^1(\Omega)$. We then conclude that

$$c_k\mapsto \left\langle A\left(\left(u_{\neq k}^N + c_k\nabla\phi_k\right)\right)\left(u_{\neq k}^N c_i^N(t)\nabla\phi_i(x) + c_k\nabla\phi_k\right),\nabla\phi_j\right\rangle,$$

where

$$u_{\neq k}^N = \sum_{i=1,i\neq k}^N c_i^N(t)\nabla\phi_i(x),$$

is continuous for every c_k, which reveals continuity of the right hand side of (197).

Energy estimates

In the next step we provide some inequalities which allow us to derive the necessary a priori estimates. Consider the time derivative of the energy $\mathcal{E}$

$$\begin{aligned}\frac{d}{dt}\mathcal{E}(t) &= \frac{d}{dt}\int_\Omega \left(F(u^N) + \epsilon^2\frac{\gamma(\theta_{\nabla u^N})^2}{2}|\nabla u^N|^2\right)\\ &= \int_\Omega F'(u^N)\partial_t u^N + \epsilon^2\left(\gamma\gamma'\theta_t\,|\nabla u|^2 + \gamma^2\nabla u^N\nabla u_t^N\right)\\ &= \int_\Omega F'(u^N)u_t^N + \epsilon^2\left(\gamma\gamma'\begin{pmatrix}-\partial_y u^N\\ \partial_x u^N\end{pmatrix} + \gamma^2\nabla u^N\right)\cdot\nabla u_t^N\\ &= \int_\Omega \mu^N\partial_t u^N \quad = -\int_\Omega m_\delta(u^N)|\nabla\mu^N|^2,\end{aligned}$$

where we exploited the particular representation of θ, i.e. (3). Integrating over $[0,t]$ then reveals

$$\begin{aligned}&\int_\Omega \epsilon^2\frac{\gamma(\theta_{\nabla u^N(t)})^2}{2}|\nabla u^N(t)|^2 + \int_\Omega F(u^N(t)) + \int_{\Omega_t} m_\delta(u^N)|\nabla\mu^N|^2\\ &\qquad = \int_\Omega \epsilon^2\frac{\gamma(\theta_{\nabla u^N(0)})^2}{2}|\nabla u^N(0)|^2 + \int_\Omega F(u^N(0)) \le C.\end{aligned} \tag{200}$$

From (194) with $j=1$ we deduce that $\partial_t\int_\Omega u^N = 0$ and since γ is bounded uniformly we obtain from Poincaré 's inequality

$$\operatorname{ess\,sup}_{0<t<T}\|u^N(t)\|_{H^1(\Omega)} \le C, \tag{201}$$

which implies that $c_1^N,...,c_N^N$ are bounded uniformly and therefore a global solution to (197)-(199) exists.

A priori estimates

We now derive the necessary a priori estimates which imply convergence of subsequences. Denote by Π_N the projection of $L^2(\Omega)$ onto $span\{\phi_1,...,\phi_N\}$. This reveals

$$\begin{aligned}\left|\int_{\Omega_T}\partial_t u^N\phi\right| &= \left|\int_{\Omega_T}\partial_t u^N\nabla\Pi_N\phi\right|\\ &= \left|\int_{\Omega_T} m_\delta(u^N)\nabla\mu^N\nabla\Pi_N\phi\right|\\ &= \left(\int_{\Omega_T}\left|m_\delta(u^N)\nabla\mu^N\right|^2\right)^{\frac12}\left(\int_{\Omega_T}|\nabla\Pi_N\phi|^2\right)^{\frac12}\\ &\le B_1\left(\int_{\Omega_T} m_\delta(u^N)\left|\nabla\mu^N\right|^2\right)^{\frac12}\|\nabla\phi\|_{L^2(\Omega_T)}\\ &\le C\|\nabla\phi\|_{L^2(\Omega_T)}\end{aligned}$$

for all $\phi\in L^2(0,T;H^1(\Omega))$. Note that we exploited (200) for the last inequality.

We are now in the position to deduce that there exist subsequences (which we still denote by u^N) such that

$$\begin{aligned}
u^N &\overset{*}{\rightharpoonup} u && \text{weak} - * && \text{in} && L^\infty(0,T;H^1(\Omega)),\\
u^N &\to u && \text{strongly} && \text{in} && C([0,T];L^2(\Omega)),\\
\partial_t u^N &\rightharpoonup \partial_t u && \text{weakly} && \text{in} && L^2(0,T;(H^1(\Omega))'), \text{ and}\\
u^N &\to u && \text{strongly} && \text{in} && L^2(0,T;L^p(\Omega)) \text{ and a.e. in } \Omega_T,
\end{aligned}$$

where $p < \frac{2n}{n-2}$. It remains to show the convergence of μ^N. To this end we first show that

$$A(\nabla u^N)\nabla u^N \rightharpoonup A(\nabla u)\nabla u \quad \text{in } \left[L^2(\Omega)\right]^2. \tag{202}$$

Since

$$\begin{aligned}
&(A(\theta_\xi)\xi)^T \cdot (A(\theta_\xi)\xi)\\
&= \begin{pmatrix} \gamma^2(\theta_\xi)\xi_1 - \gamma'(\theta_\xi)\gamma(\theta_\xi)\xi_2 \\ \gamma'(\theta_\xi)\gamma(\theta_\xi)\xi_1 + \gamma^2(\theta_\xi)\xi_2 \end{pmatrix}^t \cdot \begin{pmatrix} \gamma^2(\theta_\xi)\xi_1 - \gamma'(\theta_\xi)\gamma(\theta_\xi)\xi_2 \\ \gamma'(\theta_\xi)\gamma(\theta_\xi)\xi_1 + \gamma^2(\theta_\xi)\xi_2 \end{pmatrix}\\
&= \gamma^2(\theta_\xi)(\gamma^2(\theta_\xi) + (\gamma'(\theta_\xi))^2)(\xi_1^2 + \xi_2^2)\\
&\leq C(n,G)|\xi|^2
\end{aligned} \tag{203}$$

we obtain as a direct consequence

$$\int_\Omega |A(\nabla u^N)\nabla u^N|^2 \leq C(n,G)\int_\Omega |\nabla u^N|^2. \tag{204}$$

Due to (201), the right hand side in the last inequality is uniformly bounded and hence $A(\nabla u^N)\nabla u^N$ is uniformly bounded in $L^2(\Omega)$. Knowing this we deduce that there exists $\chi \in \left[L^2(\Omega)\right]^2$ such that

$$A(\nabla u^N)\nabla u^N \rightharpoonup \chi \quad \text{in } \left[L^2(\Omega)\right]^2. \tag{205}$$

Minty's Trick

The next step in order to show (202) is to identify χ as $A(\nabla u)\nabla u$. Our ansatz is to use Minty's Trick (see Lemma 4.2.9), i.e. we have to show

$$\langle \chi - A(\nabla v)\nabla v, \nabla u - \nabla v\rangle \geq 0 \quad \text{for all } v \in H^1(\Omega). \tag{206}$$

By adding and subtracting elements we obtain

$$\begin{aligned}
&\langle \chi - A(\nabla v)\nabla v, \nabla u - \nabla v\rangle \\
&= \left\langle \chi - A(\nabla u^N)\nabla u^N + A(\nabla u^N)\nabla u^N - A(\nabla v)\nabla v, \nabla u - \nabla v \right\rangle \\
&= \left\langle \chi - A(\nabla u^N)\nabla u^N, \nabla u - \nabla v \right\rangle \\
&\quad + \left\langle A(\nabla u^N)\nabla u^N - A(\nabla v)\nabla v, \nabla u - \nabla v \right\rangle \\
&= \left\langle \chi - A(\nabla u^N)\nabla u^N, \nabla u - \nabla v \right\rangle \\
&\quad + \left\langle A(\nabla u^N)\nabla u^N - A(\nabla v)\nabla v, \nabla u - \nabla u^N + \nabla u^N - \nabla v \right\rangle \\
&= \left\langle \chi - A(\nabla u^N)\nabla u^N, \nabla u - \nabla v \right\rangle \\
&\quad + \left\langle A(\nabla u^N)\nabla u^N - A(\nabla v)\nabla v, \nabla u - \nabla u^N \right\rangle \\
&\quad + \left\langle A(\nabla u^N)\nabla u^N - A(\nabla v)\nabla v, \nabla u^N - \nabla v \right\rangle \\
&\geq \left\langle \chi - A(\nabla u^N)\nabla u^N, \nabla u - \nabla v \right\rangle \\
&\quad + \left\langle A(\nabla u^N)\nabla u^N - A(\nabla v)\nabla v, \nabla u - \nabla u^N \right\rangle, \qquad (207)
\end{aligned}$$

where the last inequality holds because of the monotonicity property. Taking the limit we observe that the right hand side goes to zero and hence

$$(\chi - A(\nabla v)\nabla v, \nabla u - \nabla v) \geq 0. \qquad (208)$$

From this we deduce that

$$\chi = A(\nabla u)\nabla u. \qquad (209)$$

Then, exploiting (204) together with the uniform boundedness of $F'(u^N(t))$ for $t \in [0, T)$, we first obtain that $\int_\Omega \mu^N(t) \leq C$ and consequently, including (200), Poincaré 's inequality leads to

$$\|\mu^N\|_{L^2(0,T;H^1(\Omega))} \leq C.$$

Note that in order to apply (200) in Poincaré 's inequality it is necessary to assume that $m_\delta > 0$. Since we already verified the weak convergence $A(\nabla u^N)\nabla u^N \rightharpoonup A(\nabla u)\nabla u$ in $\left[L^2(\Omega)\right]^2$ we obtain

$$\mu^N \rightharpoonup \mu \quad \text{in} \quad L^2(0, T; H^1(\Omega)).$$

With the convergence properties proved so far we can pass to the limit in (194) and (195) in a standard fashion [70] and obtain that (u, μ) satisfies (191) and (192). Finally the strong convergence of u^N in $C([0, T]; L^2(\Omega))$ and $u^N(0) \to u_0$ in $L^2(\Omega)$ proves Theorem 4.3.5. □

4.3.4 *The degenerate problem*

This section finally provides the proof of Theorem 4.3.4, exploiting the existence of approximate solutions which we have established in the previous section.

Defining approximate solutions

Proof. From Theorem 4.3.5 we know that there exists a weak solution to the equation

$$\begin{aligned} u_t &= \nabla \cdot m_\delta(u)\nabla\mu && \text{in } \Omega_T, \\ \mu &= F'(u) - \epsilon^2 \operatorname{div}(A(\nabla u)\nabla u) && \text{in } \Omega_T, \\ \nabla u \cdot \mathbf{n}_\Omega = 0 \quad &\text{and} \quad \nabla\mu \cdot \mathbf{n}_\Omega = 0 && \text{on } \partial\Omega \times (0,T) \end{aligned}$$

and we denote this solution by (u_δ, μ_δ).

Lemma 4.3.6 *The weak solution satisfies*

$$\nabla(\operatorname{div}(A(\nabla u_\delta)\nabla u_\delta)) \in L^2(\Omega_T).$$

Proof. We first show $\operatorname{div}(A(\nabla u_\delta)\nabla u_\delta) \in L^2(\Omega_T)$. From the definition of the weak solution we have

$$\int_\Omega (F'(u_\delta) - \mu)\psi + \epsilon^2 A(\nabla u_\delta)\nabla u_\delta \cdot \nabla\psi = 0, \tag{210}$$

for every $\psi \in H^1(\Omega)$. We then have

$$\begin{aligned} \left| \int_\Omega \epsilon^2 A(\nabla u_\delta)\nabla u_\delta \cdot \nabla\psi \right| &\le \int_\Omega |(\mu - F'(u_\delta))\psi| \\ &\le C \, \|\psi\|_{L^2(\Omega)}, \end{aligned}$$

which implies that

$$\psi \mapsto \epsilon^2 A(\nabla u_\delta)\nabla u_\delta \cdot \nabla\psi, \qquad \psi \in C_c^\infty(\Omega) \tag{211}$$

Exploiting the Riesz representation theorem

is a linear and continuous functional on $C_c^\infty(\Omega)$ with respect to the L^2-norm. Since $C_c^\infty(\Omega)$ is dense in $L^2(\Omega)$, this functional can be extended uniquely to a linear and continuous functional on $L^2(\Omega)$. From the Riesz representation theorem we then obtain existence of a unique function $v \in L^2(\Omega)$, such that v corresponds to the weak divergence of $A(\nabla u_\delta)\nabla u_\delta$ and consequently

$$\operatorname{div}(A(\nabla u_\delta)\nabla u_\delta) \in L^2(\Omega). \tag{212}$$

We may now apply the identity $\mu_\delta = F'(u_\delta) - \epsilon^2 \operatorname{div}(A(\nabla u_\delta)\nabla u_\delta)$ and since $\nabla F'(u_\delta) = F''(u_\delta)\nabla u_\delta \in \left[L^2(\Omega_T)\right]^2$ and $\nabla\mu_\delta \in \left[L^2(\Omega_T)\right]^2$ we obtain that also $\nabla(\operatorname{div}(A(\nabla u_\delta)\nabla u_\delta)) \in \left[L^2(\Omega_T)\right]^2$.
□

Therefore we can apply the weak form

$$\int_0^T \langle \zeta, \partial_t u_\delta \rangle_{H^1,(H^1)'} = -\int_{\Omega_T} m_\delta(u_\delta)\nabla\Big(F'(u_\delta) - \epsilon^2 \operatorname{div}\left(A(\nabla u_\delta)\nabla u_\delta\right)\Big)\cdot\nabla\zeta, \tag{213}$$

for all $\zeta \in L^2(0,T;H^1(\Omega))$.
In the next step, we prove the essential energy estimates.

Lemma 4.3.7 *There exists a δ_0 such that for all $0 < \delta \leq \delta_0$ the following estimates hold with a constant C independent of δ:* *Energy estimates*

$$\begin{aligned}
&(a) \quad \operatorname{ess\,sup}_{0<t<T} \int_{\Omega_t} m_\delta(u_\delta)|\nabla\mu_\delta|^2 \\
&\qquad\qquad + \int_\Omega F(u_\delta) + \frac{\epsilon^2}{2}\gamma(\theta_{\nabla u_\delta(t)})^2|\nabla u_\delta(t)|^2 \leq C \\
&(b) \quad \operatorname{ess\,sup}_{0<t<T} \int_\Omega \Phi_\delta(u_\delta(t)) \leq C \\
&(c) \quad \operatorname{ess\,sup}_{0<t<T} \int_{\Omega_T} |\operatorname{div}\left(A(\nabla u_\delta)\nabla u_\delta\right)|^2 \leq C \\
&(d) \quad \operatorname{ess\,sup}_{0<t<T} \int_\Omega (|u_\delta| - 1)_+^2 \leq C\delta^2 \\
&(e) \quad \int_{\Omega_T} |\mathbf{J}_\delta|^2 \leq C, \quad \textit{where} \quad \mathbf{J}_\delta := m_\delta(u_\delta)\nabla\mu_\delta.
\end{aligned}$$

Proof. Consider the functional *(a) Indicating lower semicontinuity*

$$I(u,\xi,\nu) := \int_\Omega \epsilon^2 \frac{\gamma(\theta_\xi)^2}{2}|\xi|^2 + \int_\Omega F(u) + \int_{\Omega_t} m_\delta(u)|\nu|^2. \tag{214}$$

From (200) we know that for the Galerkin approximations $(u_\delta^N, \mu_\delta^N)$ of (u_δ, μ_δ) we have that

$$I(u_\delta^N, \nabla u_\delta^N, \nabla\mu_\delta^N) \leq C,$$

for all $N \in \mathbb{N}$. Moreover we know that

$$\begin{aligned}
u_\delta^N &\rightharpoonup u_\delta \quad \text{in} \quad H^1(\Omega) \\
\mu_\delta^N &\rightharpoonup \mu_\delta \quad \text{in} \quad H^1(\Omega)
\end{aligned}$$

for all $t \in [0,T]$ and since $H^1(\Omega)$ is compactly embedded in $L^2(\Omega)$ (Rellich Kondrachov Theorem) the weak convergence $u_\delta^N \to u_\delta$ in $H^1(\Omega)$ implies

$$u_\delta^N \to u_\delta \quad \text{in} \quad L^2(\Omega).$$

If we now show that I is weakly lower semicontinuous, i.e.

$$I(u_\delta, \nabla u_\delta, \nabla\mu_\delta) \leq \liminf_{N\to\infty} I(u_\delta^N, \nabla u_\delta^N, \nabla\mu_\delta^N),$$

we could deduce that $I(u_\delta, \nabla u_\delta, \nabla\mu_\delta) \leq C$, which implies (a). In what follows we will show that the conditions for Lemma 4.2.7 in the preliminary section are satisfied which provides lower semicontinuity

of $I(u,\xi,\nu)$. Note that we will consider the variable ξ in Lemma 4.2.7 as playing the role of (ξ,ν) and $\mathbb{R}^4 = \mathbb{R}^2 \times \mathbb{R}^2$.
We now introduce the function

$$f(x,u,\xi,\nu) := F(u) + \frac{\epsilon^2}{2}\gamma(\theta_\xi)^2|\xi|^2 + \int_0^t m_\delta(u)|\nu|^2,$$

which is a Carathéodory function in the sense of the definition given in Section 4.2.4. Moreover we find constants $\alpha_1 > 0$ and $\alpha_2 \in \mathbb{R}$ such that f satisfies the coercivity condition

$$f(x,u,\xi,\nu) \geq \alpha_1(|\xi|^2 + |\nu|^2) + \alpha_2|u|,$$

and from Lemma 4.3.1 we also have that $\xi \to f(x,u,\xi,\nu)$ is convex. Since clearly also $\nu \to f(x,u,\xi,\nu)$ is convex we are in the position to apply Lemma 4.2.7 and deduce that $I(u,\xi,\nu)$ is weakly lower semi-continuous, which proves (a).

(b) Exploiting the auxiliary function Φ_δ

To prove (b), we consider the function $\Phi_\delta(u_\delta)$ defined by (187). Since $\Phi''_\delta(u_\delta)$ is bounded uniformly in t, we have $\Phi'_\delta(u_\delta) \in L^2(0,T;H^1(\Omega))$ and therefore $\Phi'_\delta(u_\delta)$ is an admissible test function. On the one hand, we have that

$$\int_0^t \langle \Phi'_\delta(u_\delta), \partial_t u_\delta \rangle_{H^1,(H^1)'} = \int_\Omega \Phi_\delta(u_\delta(t)) - \int_\Omega \Phi_\delta(u_0)$$

is true for almost all $t \in [0,T]$. On the other hand, we have

$$\begin{aligned}
\int_0^t \langle \Phi'_\delta(u_\delta), \partial_t u_\delta \rangle_{H^1,(H^1)'} &= \int_{\Omega_t} -m_\delta(u_\delta)\nabla\mu_\delta \cdot \nabla\Phi'_\delta(u_\delta) \\
&= \int_{\Omega_t} -m_\delta(u_\delta)\nabla\mu_\delta\Phi''_\delta(u_\delta)\cdot\nabla u_\delta \\
&= \int_{\Omega_t} -\sqrt{m_\delta(u_\delta)}\nabla\mu_\delta\cdot\nabla u_\delta \\
&\leq \left(\int_{\Omega_t} m_\delta(u_\delta(t))|\nabla\mu_\delta|^2\right)^{1/2}\left(\int_{\Omega_t}|\nabla u_\delta|^2\right)^{1/2},
\end{aligned} \tag{215}$$

where the right hand side is bounded due to (a). It follows that there exists a constant C which is independent of δ such that

$$\int_\Omega \Phi_\delta(u_\delta(t)) \leq C + \int_\Omega \Phi_\delta(u_0),$$

which proves (b).

(c) Exploiting the auxiliary function Ψ_δ

Consider now Ψ_δ defined by (188). Similar as in (215) we obtain

$$\begin{aligned}
\int_\Omega \Psi_\delta(u_\delta(t)) - \int_\Omega \Psi_\delta(u_0) &= \int_{\Omega_t} -m_\delta(u_\delta)\nabla\mu_\delta\Psi''_\delta(u_\delta)\cdot\nabla u_\delta \\
&= \int_{\Omega_t} -\epsilon^2\,\mathrm{div}(A(\nabla u_\delta)\nabla u_\delta)\Delta u_\delta - F''(u_\delta)|\nabla u_\delta|^2,
\end{aligned}$$

which again implies that there exists a constant C which is independent of δ such that

$$\int_\Omega \Psi_\delta(u_\delta(t)) + \int_{\Omega_t} \epsilon^2 \operatorname{div}(A(\nabla u_\delta)\nabla u_\delta)\Delta u_\delta + F''(u_\delta)|\nabla u_\delta|^2 \leq C + \int_\Omega \Psi_\delta(u_0).$$

Realizing that Ψ_δ and F'' are both convex functions which are bounded from below and taking Lemma 4.3.3 into account, we conclude that there exists another constant, which is independent of δ such that

$$\int_\Omega |\operatorname{div}(A(\nabla u)\nabla u)|^2 \leq C + \int_\Omega \Psi_\delta(u_0),$$

which proves (c).

(d) Popular trick exploiting Φ

We will now use the bound for $\int_\Omega \Phi_\delta(u_\delta)$ to derive a bound for $\int_\Omega (|u_\delta| - 1)_+^2$. If $z > 1$ and $\delta < 1$, then we have

$$\begin{aligned}\Phi_\delta(z) &= \underbrace{\Phi(1-\delta)}_{\geq 0} + \underbrace{\Phi'(1-\delta)}_{\geq 0}\underbrace{(z-(1-\delta))}_{\geq 0} + \frac{1}{2}\Phi''(1-\delta)(z-(1-\delta))^2 \\ &\geq \frac{1}{2}\Phi''(1-\delta)(z-1)^2 = \frac{1}{2}\frac{1}{\sqrt{m(1-\delta)}}(z-1)^2 \\ &= \frac{1}{2}\frac{1}{1-(1-\delta)^2}(z-1)^2 \geq C^{-1}\delta^{-2}(z-1)^2.\end{aligned}$$

It follows that $(z-1)^2 \leq C\delta^2\Phi_\delta(z)$. Similarly we obtain $(-z-1)^2 \leq C\delta^2\Phi_\delta(z)$ for $z < -1$. This implies

$$\int_\Omega (|u_\delta| - 1)_+^2 \leq C\delta^2 \int_\Omega \Phi_\delta(u_\delta) \leq C\delta^2,$$

which proves (d).

Assertion (e) follows easily from (a), and this finishes the proof of Lemma 4.3.7. □

According to the bounds of Lemma 4.3.7 together with standard compactness properties, we obtain that there exists a function u such that

$$\begin{aligned}\partial_t u_\delta &\rightharpoonup \partial_t u && \text{in} && L^2(0,T;(H^1(\Omega))') \\ \mathbf{J}_\delta &\rightharpoonup \mathbf{J} && \text{in} && \left[L^2(\Omega_T)\right]^2.\end{aligned}$$

Minty's Trick

Moreover by the boundedness of $\operatorname{div}(A(\nabla u_\delta)\nabla u_\delta)$ in $L^2(\Omega_T)$ we have that

$$A(\nabla u_\delta)\nabla u_\delta \rightharpoonup \chi \qquad \text{in } \left[H^1(\Omega)\right]^2,$$

for some function $\chi \in \left[H^1(\Omega)\right]^2$. Similar as in (206), we can identify χ as $A(\nabla u_\delta)\nabla u_\delta$ by applying Minty's Trick. Adding and subtracting elements analogously as in (207), but with u and u_δ instead of u and u^N, we obtain that for all $v \in H^1(\Omega)$

$$\begin{aligned}\langle \chi - A(\nabla v)\nabla v, \nabla u - \nabla v\rangle \geq \langle \chi - A(\nabla u_\delta)\nabla u_\delta, \nabla u - \nabla v\rangle \\ + \langle A(\nabla u_\delta)\nabla u_\delta - A(\nabla v)\nabla v, \nabla u - \nabla u_\delta\rangle,\end{aligned}$$

and passing to the limit $\delta \to 0$ reveals

$$\langle \chi - A(\nabla v)\nabla v, \nabla u - \nabla v\rangle \geq 0 \quad \text{for all } v \in H^1(\Omega). \tag{216}$$

We are now in the position to apply Minty's Trick (Lemma 4.2.9) and deduce that

$$\chi = A(\nabla u)\nabla u. \tag{217}$$

Rellich Kondrachov Theorem

Since $H^1(\Omega)$ is compactly embedded in $L^2(\Omega)$ the weak convergence $A(\nabla u_\delta)\nabla u_\delta \rightharpoonup A(\nabla u)\nabla u$ in $\left[H^1(\Omega)\right]^2$ implies

$$A(\nabla u_\delta)\nabla u_\delta \to A(\nabla u)\nabla u \qquad \text{in } \left[L^2(\Omega)\right]^2. \tag{218}$$

Passing to the limit in

$$\int_\Omega (|u_\delta| - 1)_+^2 \leq C\delta^2$$

yields $|u| \leq 1$ a.e. in Ω_T.

Convergence of the limit equation

It remains to show that u fulfills the limit equation. The weak convergence of $\partial_t u_\delta$ and $\mathbf{J}_\delta$ gives in the limit

$$\int_0^T \langle \xi, \partial_t u\rangle_{H^1,(H^1)'} = \int_{\Omega_T} \mathbf{J}\cdot\nabla\xi,$$

for all $\xi \in L^2(0,T;H^1(\Omega))$. Now we have to identify $\mathbf{J}$. Therefore, we want to pass to the limit in the equation

$$\int_{\Omega_T} \mathbf{J}_\delta \cdot \mathbf{j} = \int_{\Omega_T} m_\delta(u_\delta)\nabla(-\epsilon^2 \operatorname{div}(A(\nabla u_\delta)\nabla u_\delta) + F'(u_\delta))\mathbf{j}, \tag{219}$$

where $\mathbf{j} \in L^2(0,T;H^1(\Omega,\mathbb{R}^n)) \cap L^\infty(\Omega_T,\mathbb{R}^n)$ with $\mathbf{j}\cdot\mathbf{n}_\Omega = 0$ on $\partial\Omega \times (0,T)$. The left hand side converges to $\int_{\Omega_T}\mathbf{J}\cdot\mathbf{n}$. Since $\nabla \operatorname{div}(A(\nabla u_\delta)\nabla u_\delta)$ may not have a limit in $L^2(\Omega_T)$, we integrate the first term on the right-hand side of (219) by parts to get

$$\begin{aligned}&\int_{\Omega_T} m_\delta(u_\delta)\nabla(-\epsilon^2 \operatorname{div}(A(\nabla u_\delta)\nabla u_\delta))\mathbf{j} \\ &\qquad = \int_{\Omega_T} \epsilon^2 \operatorname{div}(A(\nabla u_\delta)\nabla u_\delta) m_\delta(u_\delta)\nabla\mathbf{j} \\ &\qquad\quad + \int_{\Omega_T} \epsilon^2 \operatorname{div}(A(\nabla u_\delta)\nabla u_\delta) m_\delta'(u_\delta)\nabla u_\delta\cdot\mathbf{j} \\ &\qquad =: \mathrm{I} + \mathrm{II}.\end{aligned} \tag{220}$$

Using the fact that for all $z \in \mathbb{R}$

$$|m_\delta(z) - m(z)| \leq \sup_{1-\delta \leq |y| \leq 1} |m(y)| \to 0 \quad \text{as } \delta \to 0,$$

it follows that $m_\delta \to m$ uniformly.
Hence we have

$$m_\delta(u_\delta) \to m(u) \quad \text{a.e. in } \Omega_T.$$

Exploiting that $\operatorname{div}(A(\nabla u_\delta)\nabla u_\delta)$ is uniformly bounded in $L^2(\Omega_T)$, we may deduce that there exists $\rho \in L^2(\Omega_T)$ such that

$$\operatorname{div}(A(\nabla u_\delta)\nabla u_\delta) \rightharpoonup \rho \qquad \text{in } L^2(\Omega_T). \tag{221}$$

From the definition of the weak divergence and the already established convergence (218), we then have that for any test function $\Psi \in C_c^\infty(\Omega_T)$

$$\begin{aligned} \int_{\Omega_T} \operatorname{div}(A(\nabla u_\delta)\nabla u_\delta)\Psi &= -\int_{\Omega_T} A(\nabla u_\delta)\nabla u_\delta \cdot \nabla \Psi \\ &\to -\int_{\Omega_T} A(\nabla u)\nabla u \cdot \nabla \Psi \\ &= \int_{\Omega_T} \operatorname{div}(A(\nabla u)\nabla u)\Psi. \end{aligned} \tag{222}$$

Since the weak divergence is unique we immediately obtain

$$\operatorname{div}(A(\nabla u)\nabla u) = \rho. \tag{223}$$

Recalling that M_δ is uniformly bounded, we conclude

$$\int_{\Omega_T} \epsilon^2 \operatorname{div}(A(\nabla u_\delta)\nabla u_\delta) m_\delta(u_\delta)\nabla \mathfrak{j} \to \int_{\Omega_T} \epsilon^2 \operatorname{div}(A(\nabla u)\nabla u) m_\delta(u)\nabla \mathfrak{j},$$

as $\delta \to 0$, which equals the convergence of I in (220) . Now we pass to the limit in II. As for m, we have $m'_\delta \to m'$ uniformly, which gives

$$m'_\delta(u_\delta) \to m'(u_\delta) \quad \text{a.e. in } \Omega_T.$$

By using

$$A(\nabla u_\delta)\nabla u_\delta \to A(\nabla u_\delta)\nabla u_\delta \quad \text{in } L^2(\Omega_T) \quad \text{and a.e. in } \Omega_T,$$

and the fact that m'_δ is uniformly bounded a generalized version of the Lebesgue convergence theorem yields

$$m'_\delta(u_\delta)\nabla u_\delta \to m'(u)\nabla u \quad \text{in } L^2(\Omega).$$

Hence

$$\begin{aligned} \int_{\Omega_T} \epsilon^2 \operatorname{div}(A(\nabla u_\delta)\nabla u_\delta) m'_\delta(u_\delta)\nabla u_\delta \cdot \mathfrak{j} \\ \to \int_{\Omega_T} \epsilon^2 \operatorname{div}(A(\nabla u)\nabla u) m'_\delta(u)\nabla u_\delta \cdot \mathfrak{j}, \end{aligned}$$

as $\delta \to 0$, where we used the fact that $\mathfrak{j} \in L^\infty(\Omega_T)$.
This shows that u solves the Cahn-Hilliard equation in the sense of Theorem 4.3.4. □

4.4 DISCUSSION AND OUTLOOK

Summary of results

We have proved the existence of weak solutions to the anisotropic Cahn-Hilliard equation (166) with degenerate mobility under the assumption that the strength of the anisotropy is sufficiently small (see Lemma 4.3.3). The main difficulties arise in establishing the estimates of Lemma 4.3.7, in particular in view of the degenerate mobility and the non-linear anisotropy function. The limitation to sufficiently weak anisotropy enables to apply Lemma 4.3.3 given in the preliminary results of Section 4.3.1 at this point, which turns out to be of essential importance for the present existence proof. In addition to existence, we show that solutions $|u|$ are bounded by one without having a maximum principle.

Open questions

There are still many open questions. The most important is whether the assumptions of Lemma 4.3.3 may be relaxed in order to obtain existence of solution in a more general case. In particular, the existence of solutions on different, not necessarily rectangular, domains would be desirable, which appears to be intuitively possible.

Uniqueness

Furthermore , it would be interesting to know if there exists a unique solution. We note that already in the isotropic case, studied by Elliott and Garcke [32], this remains an open question. Since so far no uniqueness result for fourth order degenerate parabolic equations has been established, a corresponding existence result for the present problem is less obvious.

Behavior of solutions

Besides studying the question of uniqueness we are also interested in the qualitative behavior of solutions, for example as $|u| \to 1$. Just as in the isotropic case we expect that for the present degenerate mobility the sets $\{u = -1\}$ and $\{u = 1\}$ develop an interior which implies a free boundary problem for $\partial\{u = -1\}$ and $\partial\{u = -1\}$, respectively. In addition, it would be interesting to study the asymptotic behavior of solutions in the case as $t \to \infty$.

5 NUMERICAL SIMULATION OF THE SOLID STATE DEWETTING PROBLEM

5.1 THE PROCESS OF DEVELOPING THE NUMERICAL ALGORITHM

Obvious numerical challenges

The different mathematical models for solid state dewetting are in general complicated and can only be solved analytically in very special cases. Numerical simulations are therefore of particular importance. However, the corresponding numerical algorithms have to deal with a variety of numerical challenges such as the strong nonlinearity, anisotropy, coupling of geometry and evolutionary differential equations and numerical discretization. In addition, the rigorous mathematical understanding of anisotropic interface motion is far from being complete, which makes it even more challenging to provide and improve a numerical algorithm.

Different numerical approaches

Over the last decades, many different numerical methods have been developed for both the sharp interface and phase field model. On the one hand, the simulation of the sharp interface via interface tracking methods [24, 26, 114] appears to be the most efficient but has a severe drawback when it comes to topological changes. On the other hand the phase field framework can naturally handle this challenge and finite difference as well as finite element methods have been successfully applied to simulate anisotropic interface motion. In [94], for example, an anisotropic viscous Cahn-Hilliard model is implemented by adaptive finite elements in three space dimensions. In particular cases, the results are compared with the simulation of sharp interface models. An example for a successful finite difference implementation is given by [113], where the method is applied for a regularized, strongly anisotropic Cahn-Hilliard equation in two and three space dimensions. However, both examples do not incorporate boundary conditions at a substrate. For more examples and other aspects of thin film simulation we refer to the recent reviews [33, 73] and in particular [67], where of some the finite element based numerical methods for simulating the motion of interfaces are reviewed.

Developing the numerical code

The numerical algorithm presented in this chapter has a long history of development and besides the above mentioned obvious numerical challenges, additional less than obvious difficulties just became apparent during the process of developing the numerical code. This gave us the opportunity to steadily built our knowledge about applying particular methods and implementing the present non-linear structures. The result is a semi-implicit time-stepping method, applying the finite element method and providing a diffuse boundary

approximation, which significantly simplifies the implementation of the anisotropic boundary conditions at the substrate. However, since the process of developing the numerical code has provided us with valuable insights into the different numerical methods applied to the solid state dewetting problem, we would like to briefly document the history of developing the numerical algorithm.

The numerical approach by Jiang et al.

Our first numerical approach was inspired by Jiang et al. [52], who consider an isotropic solid state dewetting problem, similar to the isotropic version of (49) - (49c), but with mobility $m(u) = 1 - u^2$. The idea, presented in [52], of combining finite differences with spectral methods seemed particularly suitable for the present kind of problem at first sight, since it fits well with the present boundary conditions. On the one hand, the choice of a pseudospectral representation in the space direction where the problem contains periodic boundary conditions is advantageous since it considerably speeds up the calculation of partial derivatives compared to the finite difference method (see [107]). On the other hand, the space direction where the problem contains rather complicated non-linear boundary conditions can be implemented directly by the finite difference method. Furthermore, Jiang et al. [52] apply a stabilizing method in order to improve the time-step constraint. The method, called convexity- splitting, adds stabilizing terms to the scheme such that the time-discretization reads

Considering convexity-splitting

$$\begin{cases} \frac{u^{n+1}-u^n}{\tau} & = A\epsilon^2\Delta^2(u^n - u^{n+1}) + S\Delta(u^{n+1} - u^n) + \nabla \cdot (m(u^n)\nabla\mu^n) \\ \mu^n & = (u^n)^3 - u^n - \epsilon^2\Delta u^n, \end{cases} \tag{224}$$

where u^n and μ^n are the approximations of u and μ at the time $t = n\tau$. The constants A and S are stabilizing coefficients and the idea of adding stabilizing terms to the Cahn-Hilliard equation with a non constant mobility was motivated in [120], where the isotropic Cahn-Hilliard equation with periodic boundary conditions in each direction is considered. However, there is an apparent error in the accuracy, especially near equilibrium and when time steps are too big, which is also documented in [52]. This effect becomes even stronger if choosing the higher degenerated mobility $m(u) = (1 - u^2)^2$, as we have observed in our first attempt, and consequently refused on the application of a convexity-splitting.

First numerical approach

Our first (serious) numerical approach was based on a combination of finite differences and the cosine pseudospectral method, similar as in [52], but without a stabilization method. In addition, we included an anisotropic surface energy and anisotropic boundary conditions at the substrate. Evaluating the corresponding simulations, we made different negative observations, such as the incorrect calculation of anisotropies via the spectral method if the mesh grid is too fine or loss in mass due to finite differences in particular in combination with the free boundary. The former observation may be explained by the

so-called aliasing effect, which typically occurs in the application of pseudospectral methods if picking "bad interpolants", i.e. with highly pitched sines and cosines in the expansions. The second observation is probably due to a simple consistency error. Furthermore, without a stabilization method, the numerical code turned out to require very small time-steps.

The diffuse domain method

In view of the anisotropic boundary conditions (49b) at Γ_w, we realized that the correct numerical implementation is a non-trivial issue due to the third order derivatives and nonlineratities. Inspired by Lowengrub et al. [67, 68], we found an alternative approach which allows a much easier handling. The original idea of the so-called diffuse domain method, which was first introduced by [60], refers to the approximation of a partial differential equation by introducing a phase field function. This phase field function is an approximation of the characteristic function of the domain such that the sharp interface of the original problem is replaced by a narrow diffuse interface layer. In this context the diffuse domain method describes the construction of a phase field out of a sharp interface model. In our case the application is slightly different since we already originate from a phase field model. Here we will apply the diffuse domain approach to the "sharp" boundary Γ_w and replace it with a diffuse layer. This leads to homogeneous boundary condition at the extended domain boundary which is much easier to implement numerically and also more interesting from a mathematical point of view. It also seems natural to consider also a diffuse domain boundary in a model which already considers a diffuse interface inside the domain.

Overview of this chapter

The chapter is organized as follows. We first derive the representation of the problem on the extended domain considering a diffuse boundary approximation at Γ_w. We use the method of matched asymptotic expansions to show that solutions of the re-formulated equations converge to those of the original equations. Next, we generate the discrete problem and give a solution algorithm according to the finite element space. A demonstration of the numerical code is presented for various dewetting scenarios. Since the initial motivation for choosing the phase field representation was to simulate pinch off scenarios, we will demonstrate how the simulation naturally handles this case. Moreover as the question of how the mobility influences the evolution has been addressed in the introduction of Chapter 3, we compare the results to the simulation with mobility $m(u) = 1 - u^2$. Note that the the numerical results shown in this Chapter represent a first evaluation of the current numerical code, since it was completed shortly before the submission of this work. Consequently, there are many other interesting questions which should be studied numerically, motivated in the last section of this chapter.

5.2 THE DIFFUSE BOUNDARY APPROXIMATION

Reformulation on an extended domain

We now reformulate the problem on an extended domain Ω_1 with diffuse boundary Γ_w. The idea of replacing the original domain with a sharp boundary by a domain with a diffuse boundary was introduced in [60] and has already been applied in several works [67, 68]. However, the situation in our case is slightly different, since we already originate from a phase field model which considers diffuse interfaces. This implies that the application of the method requires a reformulation of the total free energy. We start by introducing a boundary layer at Γ_w with thickness $\epsilon_y \ll 1$ and use a surface delta function for the wall energy density (47) such that we can formally rewrite the total free energy (1) on Ω_1 in one integral

$$W^\epsilon = \int_{\Omega_1} f_{FV} + \delta_{\Gamma_w} f_w \; d\Omega_1, \tag{225}$$

where δ_{Γ_w} satisfies

$$\int_{\Omega_1} h\delta_{\Gamma_w} \, d\Omega_1 \approx \int_{\Gamma_w} h \, d\Gamma, \tag{226}$$

for any smooth function h. Calculating the first variation of the free energy functional thus leads to the chemical potential

$$\mu = F'(u) + \delta_{\Gamma_w} \epsilon \frac{f_w'}{\lambda_m} - \epsilon^2 \nabla \cdot \left(\gamma\gamma' \begin{pmatrix} -u_y \\ u_x \end{pmatrix} + \gamma^2 \nabla u \right), \tag{227}$$

which entails that the natural boundary conditions for the approximate problem are simple homogeneous Neumann boundary conditions

$$\frac{\partial u}{\partial y} = 0 \tag{228a}$$

$$\frac{\partial \mu}{\partial y} = 0, \tag{228b}$$

at $y = 0$. Note that these are easy to handle from a numerical point of view. It remains to show that the present model recovers the original equation (49) subject to the boundary conditions (49b) and (49c).

5.2.1 *Asymptotic analysis*

Matched asymptotic expansions at the diffuse boundary

We now provide a justification of the diffuse boundary approximation by using the method of matched asymptotic expansions where the outer region is inside the domain and away from Γ_w and the inner region is near Γ_w, respectively. Note that the functions are expanded in powers of the diffuse interface thickness ϵ_y, while ϵ, the parameter for the interface thickness, is held constant. Moreover, for the Dirac delta function we chose the common representation

$$\delta_{\Gamma_w}(y) = \delta_{\epsilon_y}(y) = \epsilon_y^{-1} \psi\left(\frac{y}{\epsilon_y}\right), \tag{229}$$

where $\psi \in C^\infty(\mathbb{R})$, $\psi(y) \geq 0$ for all $y \in \mathbb{R}$, satisfies

$$\int_0^\infty \psi(y)\, dy = 1 \tag{230}$$

and

$$\lim_{\epsilon_y \to 0} \int_{\mathbb{R}\setminus[0,\epsilon_y]} \delta_{\epsilon_y}(y)\, dy = 0. \tag{231}$$

Outer problem

Observing that δ_Γ vanishes in the outer region for ϵ_y sufficiently small we immediately obtain

$$\mu = F'(u) - \epsilon^2 \nabla \cdot \left(\gamma\gamma' \begin{pmatrix} -\partial_y u \\ \partial_x u \end{pmatrix} + \gamma^2 \nabla u \right), \tag{232}$$

such that the original equation (49) is recovered.

However since the outer expansions for $u(x,y)$ will be needed for matching in the following, we define them as

$$u(x,y) = u_0(x,y) \quad + \epsilon_y u_1(x,y) \quad + \ldots \tag{233}$$

and continue with the inner problem.

Inner problem

We first introduce the inner variable near Γ_w via

Stretched coordinates near Γ_w

$$\eta = \frac{y}{\epsilon_y}, \tag{234}$$

and expand the inner solution $U(x,\eta) = u(x,y)$ in orders of ϵ_y

$$U(x,\eta) = U_0(x,\eta) \quad + \epsilon_y U_1(x,\eta) \quad + \ldots. \tag{235}$$

Moreover we will need the inner expansions for θ and γ

$$\begin{aligned} \theta &= \theta_0 \quad &+ \epsilon_y \theta_1 \quad &+ \ldots \\ \gamma &= \gamma(\theta_0) \quad &+ \epsilon_y \gamma'(\theta_0) \quad &+ \ldots. \end{aligned} \tag{236}$$

From (227) we then obtain to order $O(\epsilon_y^{-2})$

Order $O(\epsilon^{-2})$

$$\partial_\eta \left(\gamma(\theta_0) \partial_\eta U_0 \right) = 0, \tag{237}$$

implying that $\gamma(\theta_0)\partial_\eta U_0$ is constant in η, i.e. $\gamma(\theta_0)\partial_\eta U_0 = c(x)$. Since the leading order boundary condition at $\eta = 0$ is

$$\partial_\eta U_0 = 0, \tag{238}$$

we find $c(x) = 0$ and $\gamma(\theta_0)$ is not constantly zero in the inner layer, we immediately obtain $c(x) = 0$.
Proceeding to order $O(\epsilon_y^{-1})$, we have

Order $O(\epsilon^{-1})$

$$0 = \epsilon \frac{f_w'(U_0)}{\lambda_m}\psi(\eta) - \epsilon^2 \left(\partial_\eta \left(\gamma(\theta_0)\gamma'(\theta_0)\partial_x U_0 + \gamma(\theta_0)^2 \partial_\eta U_1\right)\right). \tag{239}$$

with boundary conditions

$$\begin{aligned} \partial_\eta U_1 &= 0, \\ \partial_\eta \left(\gamma(\theta_0)\gamma'(\theta_0)\partial_x U_0 + \gamma(\theta_0)^2 \partial_\eta U_1\right) &= 0, \end{aligned} \tag{240}$$

at $\eta = 0$. Integrating (239) in η over $[0, \infty)$ then gives

$$\begin{aligned} 0 &= \int_0^\infty \epsilon \frac{f_w'(U_0)}{\lambda_m}\psi(\eta) - \epsilon^2 \left(\partial_\eta \left(\gamma(\theta_0)\gamma'(\theta_0)\partial_x U_0 + \gamma(\theta_0)^2 \partial_\eta U_1\right)\right) \\ &= \epsilon \frac{f_w'(U_0)}{\lambda_m} - \lim_{\eta\to\infty} \left(\epsilon^2 \left(\gamma(\theta_0)\gamma'(\theta_0)\partial_x U_0 + \gamma(\theta_0)^2 \partial_\eta U_1\right)\right). \end{aligned} \tag{241}$$

Matching

Taking the matching conditions

$$\begin{aligned} \lim_{\eta\to\infty} \partial_\eta U_1 &= \lim_{y\to 0} \partial_y u_0 \\ \lim_{\eta\to\infty} \partial_x U_0 &= \lim_{y\to 0} \partial_x u_0 \end{aligned} \tag{242}$$

into account we end up with

$$\frac{f_w'(u)}{\lambda_m} - \epsilon \left(\gamma(\theta_0)\gamma'(\theta_0)\partial_x u_0 + \gamma(\theta_0)^2 \partial_\eta u_0\right) = 0, \tag{243}$$

which recovers the boundary condition (49b). Note, when comparing to the signs in (49b), that $\mathbf{n}_\Omega$ is the outward pointing normal vector onto Ω, such that $\mathbf{n}_\Omega = (0, -1)^T$.

5.3 NUMERICAL ALGORITHM

Finite element method

As elucidated in the introductory Section 5.1, we tried different numerical methods, involving the finite difference and spectral method, in order to implement the present problem. In the end the finite element method (FEM) has proven to be the most suitable for our purpose and a significant advantage over the previously applied methods is that the discrete problem can be generated in a relatively simple and systematic way by exploiting the representation in the finite element space.

In this section we will generate the discrete problem and give a solution algorithm according to the finite element space, whereas we will not give particular algorithms for the corresponding subproblems, such as the generation of the shape functions or the initial mesh, as these are somehow basic knowledge of the finite element method. For a detailed introduction and possible solution for the different subproblems we refer to Chapter 4 in [39].

5.3.1 *Generation of the discrete problem*

Model assumptions

We now present a finite element algorithm for the anisotropic phase field model (49), providing the present diffuse boundary approximation, i.e. we consider the modified chemical potential (227) and homogeneous Neumann boundary conditions (228) for u and μ on $\partial\Omega$. We assume an anisotropic surface energy of the form

$$\gamma(\theta) = 1 + G_s \cos(n\theta), \tag{244}$$

where G_s represents the strength of the anisotropy and $n > 1$ is the order of the rotational symmetry. Since the scope of our study is restricted to weak anisotropy, i.e. $\gamma'' + \gamma > 0$, we consider

$$0 \leq G_s < \frac{1}{n^2 - 1}. \tag{245}$$

Choosing a surface delta function

Furthermore, we apply the following representation for the surface delta function

$$\delta_{\Gamma_w} = \frac{\sqrt{2}}{\epsilon_y \sqrt{\pi}} \exp\left(-\frac{y^2}{2\epsilon_y^2}\right), \tag{246}$$

where δ_{Γ_w} has approximately width $\epsilon_y/2$ on $[0, \infty)$, achieves its maximum at $y = 0$ and satisfies the condition

$$\int_0^\infty \frac{\sqrt{2}}{\epsilon_y \sqrt{\pi}} \exp\left(-\frac{y^2}{2\epsilon_y^2}\right) dy = 1. \tag{247}$$

To simplify matters we let $\epsilon_y = \epsilon$. Note that the asymptotic analysis of the previous section assumed that $\epsilon_y \ll \epsilon$ and the derivation of the asymptotic limits in the case in which $\epsilon_y = \epsilon$ appears to be more difficult. However this differentiation does not make a difference for the numerical algorithm, since both ϵ are held fixed during the simulation.

Weak formulation

We start from the weak formulation. Note that the standard weak formulation, see equation (213) in Section 4.3.4, is based on the space $H^2(\Omega)$ thus any standard conforming finite element method must use elements in $C^1(\Omega)$, which are complicated to construct. Consequently, it is preferable to transform the fourth-order problem into a system of two second-order problems. Exploiting the matrix representation (167) for a better overview, the weak formulation reads:

Find a pair $(u, \mu) \in \left[H^1(\Omega)\right]^2$ such that

$$\int_\Omega \partial_t u v + \int_\Omega m(u) \nabla \mu \cdot \nabla v = 0\,, \tag{248a}$$

$$\int_\Omega \mu w - \int_\Omega \epsilon^2 \left(A(\nabla u) \nabla u\right) \cdot \nabla w = \int_\Omega N(u) w, \tag{248b}$$

for all $v, w \in H^1(\Omega)$, where

$$N(u) := 2\left(u^3 - u\right) + G(y)(u^2 - 1), \tag{249}$$

and $G(y)(u^2-1)$ represents the diffuse boundary approximation, i.e.

$$\delta_{\Gamma_w}\epsilon\frac{f_w'}{\lambda_m} = \delta_{\Gamma_w}\frac{\epsilon}{\lambda_m}\frac{3}{4}(u^2-1)(\gamma_{VS}-\gamma_{FS}), \tag{250}$$

where, according to the sharp interface limits which we derived in Chapter 3, we apply $\lambda_m \equiv 3/4$ in order to recover the Young-Herring contact angle boundary condition. $G(y)$ then becomes

$$G(y) = \frac{\sqrt{2}}{\sqrt{\pi}}\ \exp\left(-\frac{y^2}{2\epsilon^2}\right)(\gamma_{VS}-\gamma_{FS}). \tag{251}$$

The boundary conditions are homogeneous Neumann boundary conditions for u and μ on $\partial\Omega$. Note that we already exploited these boundary conditions in the derivation of (248).

Galerkin approximation in space

We first apply a Galerkin approximation in space, i.e. we assume that $V_h \subset H^1(\Omega)$ is a finite dimensional subspace of $H^1(\Omega)$ with basis $\{\phi_i\}_{i\in\mathbb{N}}$ such that every $u_h, \mu_h \in V_h$ may be represented as linear combination of this basis

$$\begin{aligned} u_h(t,x) &= \sum_{j=1}^{\dim V_h} \alpha_j(t)\phi_j(x) \\ \mu_h(x) &= \sum_{j=1}^{\dim V_h} \beta_j\phi_j(x). \end{aligned} \tag{252}$$

The Galerkin approximation of (248) then reads:

Find a pair $(u_h, \mu_h) \in [V_h]^2$ such that

$$\sum_{j=1}^{\dim V_h}\left(\partial_t\alpha_j\ \left(\phi_j,\phi_i\right)_{L^2(\Omega)} + \beta_j\int_\Omega m(u_h)\nabla\phi_j\cdot\nabla\phi_i\right) = 0\,,$$

$$\sum_{j=1}^{\dim V_h}\left(\beta_j\left(\phi_j,\phi_i\right)_{L^2(\Omega)} - \epsilon^2\alpha_j\int_\Omega\left(A(\nabla u_h)\nabla\phi_j\right)\cdot\nabla\phi_i\right) = \int_\Omega N(u_h)\phi_i,$$

for all $\phi_i, i \in \{1,..,\dim V_h\}$.

Finite differences in time

Then we discretize the time via

$$\partial_t u_h \ \approx\ \frac{u_h^{n+1}-u_h^n}{\tau},$$

where τ is the time-step size and u_h^n denotes the approximation of u_h at the time $t = ndt$. Introducing the bilinear forms

$$b^*(u,v) := \int_\Omega m(u^*)\nabla u\cdot\nabla v,$$

and

$$a^*(u,v) := \int_\Omega\left(A(\nabla u^*)\nabla u\right)\cdot\nabla v,$$

for $u, v \in H^1(\Omega)$, where $u^* = u_h^n$, the discrete problem becomes

$$\sum_{j=1}^{\dim V_h} \left(\alpha_j^{n+1} \ (\phi_j, \phi_i)_{L^2(\Omega)} + \tau \beta_j b^*(\phi_j, \phi_i) \right) = \sum_{j=1}^{\dim V_h} \alpha_j^n \ (\phi_j, \phi_i)_{L^2(\Omega)},$$
$$\sum_{j=1}^{\dim V_h} \left(\beta_j^{n+1} \, (\phi_j, \phi_i)_{L^2(\Omega)} - \epsilon^2 \alpha_j^{n+1} a^*(\phi_j, \phi_i) \right) = \int_\Omega N(u_h^n) \phi_i,$$

for all $\phi_i, i \in \{1, .., \dim V_h\}$. The solution algorithm may then be rewritten in the following block matrix form *Solution algorithm*

$$\begin{bmatrix} M & \tau \ B^* \\ -\varepsilon^2 \ A^* & M \end{bmatrix} \begin{pmatrix} \alpha^{n+1} \\ \beta \end{pmatrix} = \begin{pmatrix} \alpha^n \\ N(u_h^n) \end{pmatrix},$$

where

$$M = (m_{j,i}), \quad m_{j,i} := (\phi_j, \phi_i)_{L^2(\Omega)},$$

is the so-called mass matrix,

$$B^* = (b_{j,i}^*), \quad b_{j,i}^* := \left(b^*(\phi_j, \phi_i) \right),$$
$$A^* = (a_{j,i}^*), \quad a_{j,i}^* := \left(a^*(\phi_j, \phi_i) \right),$$

and

$$\alpha^n = (\alpha_1^n, .., \alpha_{\dim V_h}^n)^T, \quad \beta = (\beta_1, .., \beta_{\dim V_h})^T.$$

.

In each time-step we then solve the linear system

$$\begin{pmatrix} \alpha^{n+1} \\ \beta \end{pmatrix} = \begin{bmatrix} M & \tau \ B^* \\ -\varepsilon^2 \ A^* & M \end{bmatrix}^{-1} \begin{pmatrix} \alpha^n \\ N(u_h^n) \end{pmatrix}. \tag{256}$$

Note that since the matrices A^* and B^* depend on the current solution at each time-step, these have to be generated before applying the algorithm.

5.3.2 *Notes on the implementation in MATLAB*

As a discrete basis we implement standard piecewise linear finite elements. We choose the grid width according to the size of ϵ. In particular, in order to achieve a good resolution we choose $dx = dy \approx \epsilon/5$. Moreover we observed good stability properties for the time-step size $\tau \approx C\varepsilon^2$.

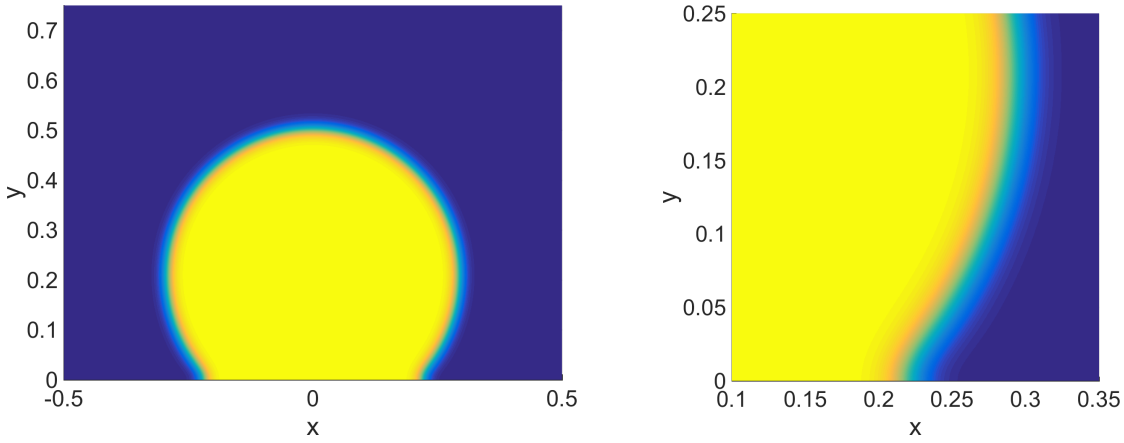

Figure 11: Surface plots from top view of the isotropic equilibrium state for $\varepsilon = 0.015$ and $\theta_c = 3\pi/4$, where $dx = dy = 0.0025$ and $\tau = 10^{-4}$ a) left: The general shape appears to not be influenced by the diffuse boundary approximation. b) right: zoom (of a)) into the region about the substrate. It is clearly visible that the solution satisfies homogeneous Neumann boundary conditions at $y = 0$, where θ_c is approximated within a diffuse region of thickness $\epsilon/2$.

5.4 RESULTS AND DISCUSSION

5.4.1 *The diffuse boundary approximation*

Diffuse boundary test

We first address the question of how the diffuse boundary approximation influences the solution. Our first simulation considers an isotropic equilibrium shape where $\varepsilon = 0.015$ and $\theta_c = 3\pi/4$. Accordingly we choose $dx = dy = 0.0025$ and $\tau = 10^{-4}$ The result is displayed in Fig. 11 as surface plot from top view. The picture on the left hand side shows that shape of the equilibrium state appears to not be disturbed by the diffuse boundary approximation. The picture on the right hand side shows a zoom into the region about the substrate. It is clearly visible that the approximate solution satisfies homogeneous Neumann boundary conditions at the numerical boundary at $y = 0$ and θ_c is approximated within a diffuse region of thickness $\epsilon/2$.

Since it is not immediately clear how and at which point the contact angle in this diffuse domain framework should be evaluated, we decided to compare different approximations to the exact equilibrium state instead. The exact equilibrium state in this case is a truncated circle, and the comparison is shown in Fig. 12. The parameters are exactly the same as in Fig. 11 except for ϵ. We tested $\varepsilon = 0.015$, $\varepsilon = 0.03$ and $\varepsilon = 0.45$ and documented the influence on the corresponding approximate solutions. In the domain away from the substrate the approximate solutions appear to be located slightly more towards the inside of the exact solution for bigger values of ϵ. However this difference is small compared to the size of ϵ, as shown in Fig. 12 a). The approximation of the equilibrium contact angle is shown in Fig. 12 b). We suggest the convergence towards the exact equilibrium contact

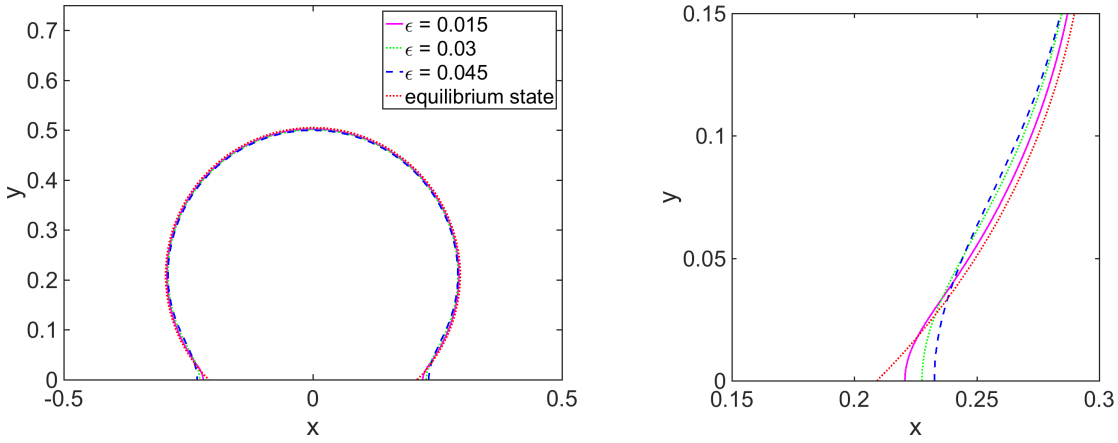

Figure 12: Contour plots of the isotropic equilibrium state for $\varepsilon = 0.015$, $\varepsilon = 0.03$ and $\varepsilon = 0.45$ in comparison to the analytic equilibrium state. As in the previous simulation we chose $\theta_c = 3\pi/4$, $dx = dy = 0.0025$ and $\tau = 10^{-4}$ a) left: The solutions for bigger values of ϵ appear to be located slightly more towards the inside of the exact solution in the domain away from the substrate. However this difference is small compared to the size of ϵ. b) right: zoom (of a)) into the region about the substrate. The Figure suggests the convergence towards the exact equilibrium contact angle θ_c as $\epsilon \to 0$.

angle θ_c as $\epsilon \to 0$.

Note that in the following we will cut-off the diffuse boundary layer at $y = 0$ and shift the whole system down about $\epsilon/2$ in order to better compare to existing results in the literature.

5.4.2 *Different mobilities*

We next address the question of how the mobility influences the evolution. As motivated in the introductory section of Chapter 3, the frequently applied mobility $m(u) = 1 - u^2$ does not lead to motion by pure surface diffusion in the sharp interface limit of the present model. Instead, the sharp interface limits which we derived in Chapter 3 show that the mobility (51), i.e. $m(u) = (1 - u^2)^2$ turns out to recover this physical process correctly. In the following we will document the difference of these two particular mobilities in corresponding simulations.

Comparison to the result by Jiang et. al

We start with a comparison motivated by a simulation given in [52]. Considering the isotropic case of (49)- (49c), Jiang et. al simulate the evolution of a retracting solid film with mobility $m(u) = 1 - u^2$, as shown in Fig. 4 in [52]. In order to compare to this result, we chose a similar setting, i.e. we confine ourselves to the isotropic case, define an initial state which is a rectangle, located in $[0.5, 0.5] \times [0, 2]$ of a $[0.7, 0.7] \times [0, 0.7]$ computational domain, chose $\epsilon = 0.01$ and the Young contact angle $\theta_c = 3\pi/4$. The mesh size is $dx = dy = 0.002$ and

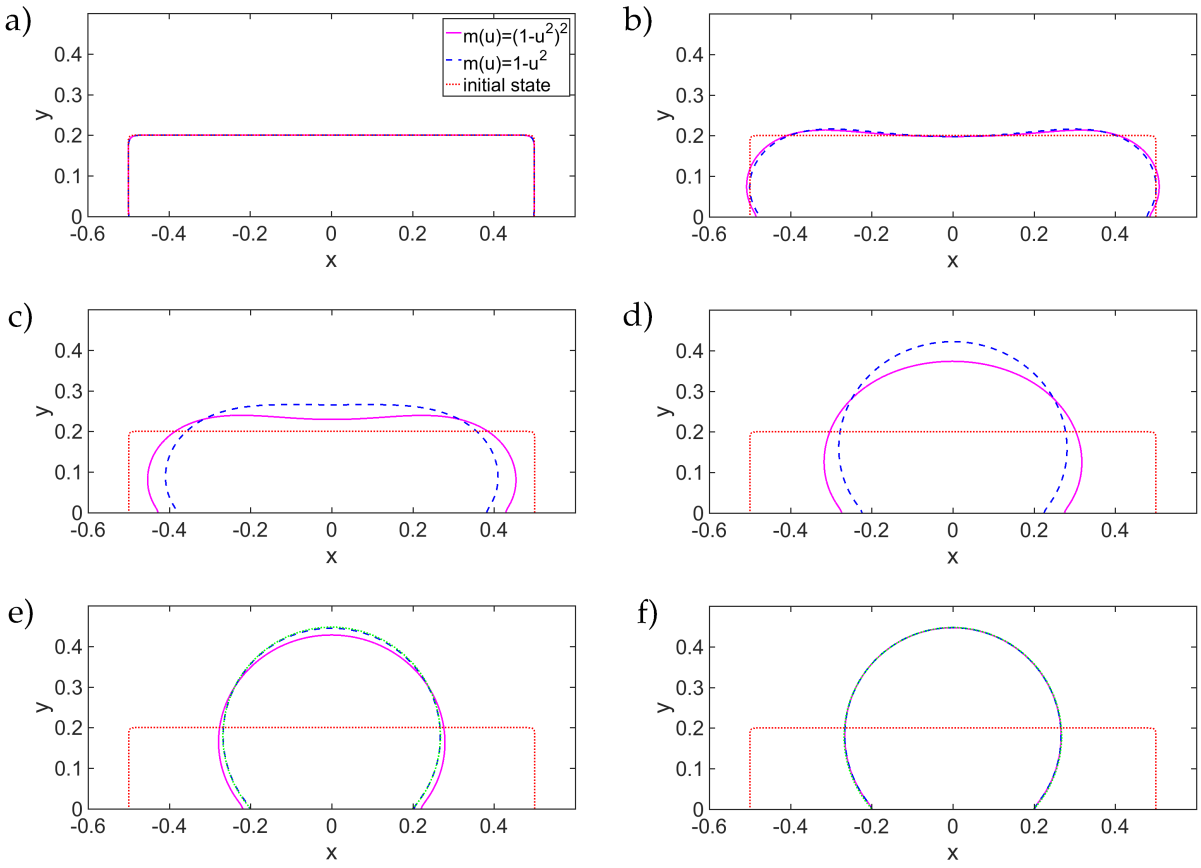

Figure 13: Numerical result showing the evolution of two thin films with different mobility where $\varepsilon = 0.01$ at a) $t = 0$, b) $t = 1$, c) $t = 10$, d) $t = 50$, e) $t = 100$, f) $t = 150$. In c) it is clearly visible how the film corresponding to the mobility $m(u) = (1-u^2)^2$ (pink solid line) forms a little valley in the middle whereas the film corresponding to the mobility $m(u) = 1-u^2$ (blue dashed line) moves upwards at $x = 0$. In e) and f) the corresponding equilibrium shape, which is a truncated circle, is displayed (green dotted line), which shows, that the film corresponding to the mobility $m(u) = 1-u^2$ achieves its equilibrium much faster.

the time step is fixed as $\tau = 5 \cdot 10^{-5}$. The equilibrium shape of the thin film island is again a predictable truncated circle.

The simulation, see Fig. 13, shows how the film which corresponds to the mobility $m(u) = 1-u^2$ evolves clearly faster than the film corresponding to $m(u) = (1-u^2)^2$. In particular the film with $m(u) = (1-u^2)^2$ achieves its equilibrium at approximately $t = 100$, see Fig. 13 e), whereas the film corresponding to $m(u) = 1-u^2$ needs significantly longer. Furthermore the evolution corresponding to $m(u) = 1-u^2$ is in good qualitative agreement with the simulation given in Fig. 4 in the reference [52], which suggests the correctness of the numerical algorithm.

Pinch-off and mobility

Observing that the evolution corresponding to the model with $m(u) = (1-u^2)^2$ is not only slower in general but also differs quali-

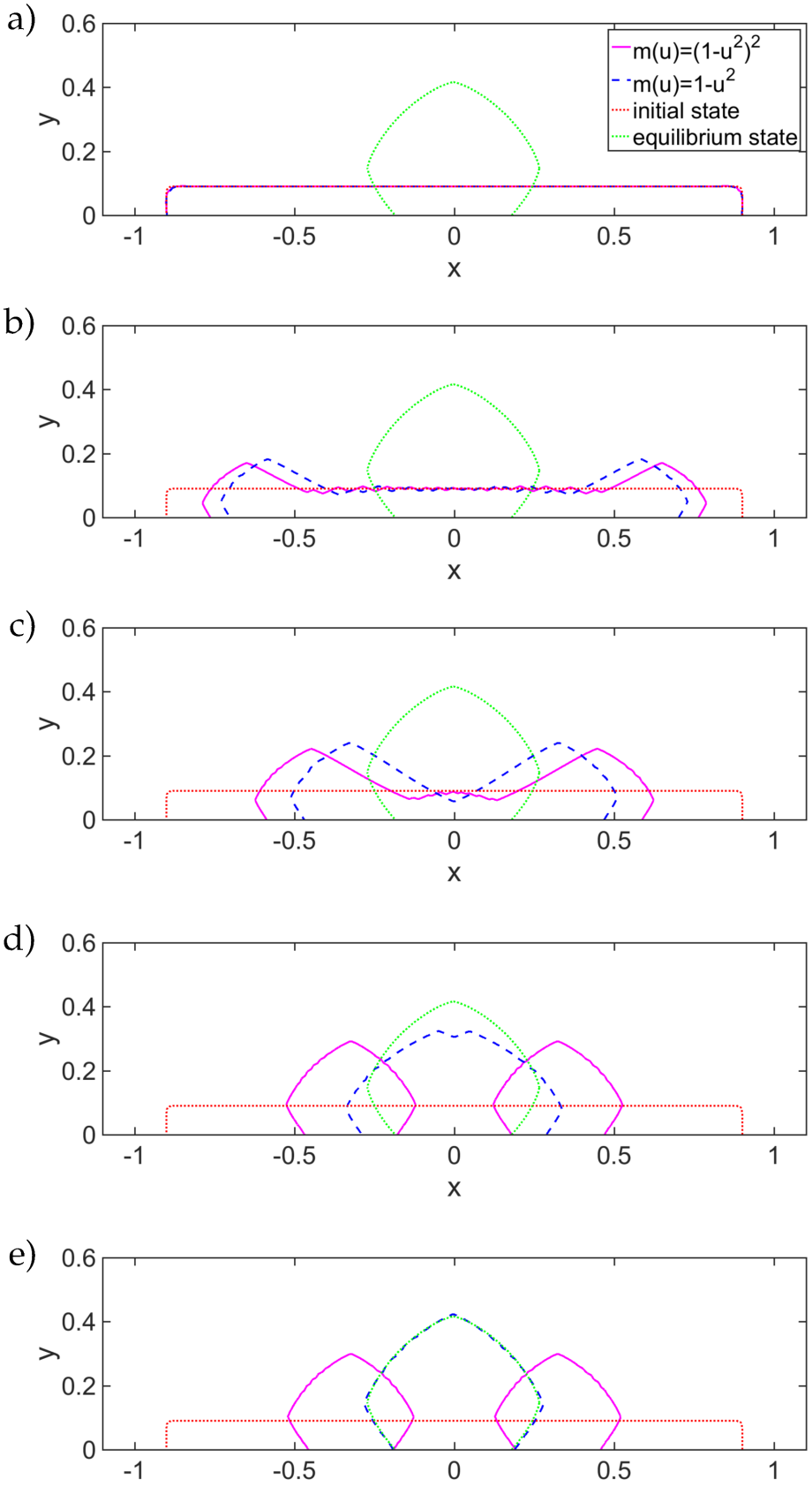

Figure 14: Numerical comparison between the evolution with mobility $m(u) = (1-u^2)^2$ and $m(u) = 1-u^2$ where $\varepsilon = 0.02$, $dx = dy = 0.002$ and $\tau = 0.001$ at a) $t = 0$, b) $t = 1$, c) $t = 5$, d) $t = 10$ and e) $t = 20$. The mobility $m(u) = 1-u^2$ leads to the formation of one single crystal whereas the mobility $m(u) = (1-u^2)^2$ results in film pinch-off.

tatively in view of the valley which forms in the middle of the film, see Fig. 13 c), the question naturally arises as to whether there is a critical film length at which the faster film contracts to a single droplet whereas the slower film pinches off. The answer is yes, as shown in Figure 14. Here we simulated a fourfold anisotropic surface energy with strength $G = 0.05$. The other parameters are $\theta_c = 3\pi/4$, $\varepsilon = 0.02$, $dx = dy = 0.002$ and $\tau = 0.001$. As expected the film corresponding to $m(u) = 1 - u^2$ forms a single equilibrium crystal, whereas the film corresponding to $m(u) = (1 - u^2)^2$ pinches off. The Figure shows in addition the exact equilibrium shape, which may be determined by the Winterbottom construction [112]. A closer look at Fig. 14 e) reveals that the analytical equilibrium shape is a little bit "smoother" than the numerical solution. This observation was also made in [110] and the explanation therein is, that in the anisotropic surface energy case, more grid points are required to capture the faceting morphology. In the reference the problem is solved by choosing more "marker" points and this may also be the solution in our case.

5.4.3 *Different anisotropies*

Pinch-off with different anisotropies

In our last simulation we consider two different anisotropies regarding their pinch-off behavior. Fig. 15 shows two films, with fourfold ($n = 4$) and sixfold ($n = 6$) symmetry, respectively. Note that the film corresponding to $n = 4$ is the same as shown in Fig. 14 and the parameters are $\varepsilon = 0.02$, $dx = dy = 0.002$ and $\tau = 0.001$. The sixfold symmetry leads to the formation of one single crystal, whereas the fourfold symmetry results in film pinch-off. This can be explained by the fact that the sixfold anisotropy, in the present orientation, prefers flat surfaces in x-direction, which prevents the formation of a valley in the middle of the flat film. However, the fourfold symmetry prefers to develop corners in the y- direction, which supports that the film touches the substrate and pinches off.

5.5 OUTLOOK

As already mentioned in the introductory Section 5.1, the numerical results shown in this Chapter present a first evaluation of the current numerical code since it was completed shortly before the submission of this work. The present simulations serve as motivation and imply many other interesting questions, which we would like to study numerically in the near future.

Further mobility tests

To begin with , there is the question if a scenario as shown in Fig. 14 may be repeated in the isotropic case. We already tried different film lengths in this situation, but the critical film length in the isotropic case appears to be significantly larger than in the fourfold anisotropy case. However, we expect that this critical film length exists.

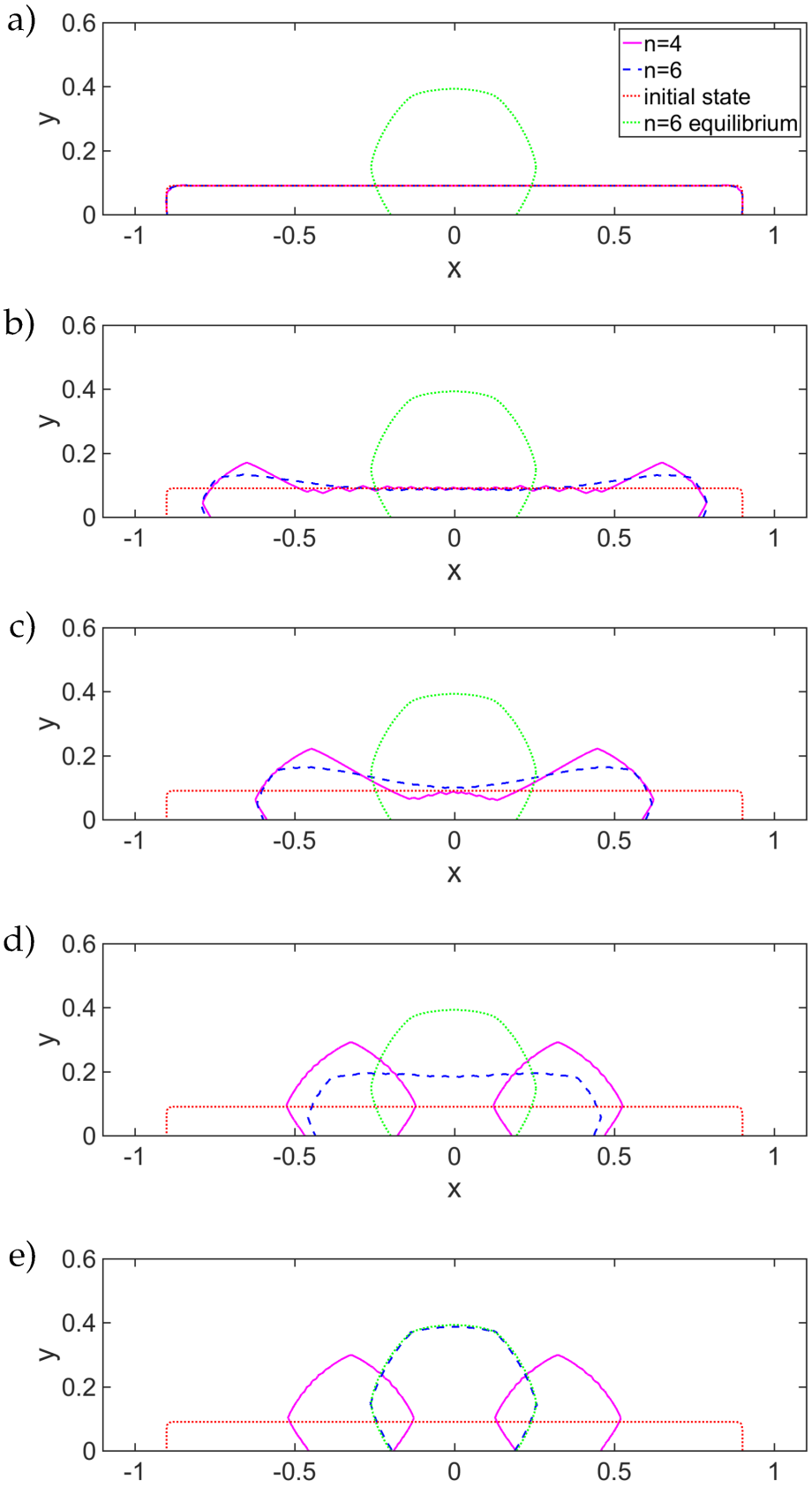

Figure 15: Numerical comparison between the evolution of two films with fourfold ($n = 4$) and sixfold ($n = 6$) symmetry, where $\varepsilon = 0.02$, $dx = dy = 0.002$ and $\tau = 0.001$. The displayed times are a) $t = 0$, b) $t = 1$, c) $t = 5$, d) $t = 10$ and e) $t = 30$. The sixfold symmetry leads to the formation of one single crystal, whereas the fourfold symmetry results in film pinch-off.

The next interesting aspect is the question of how the anisotropy influences film pinch-off. To this end, various film lengths and anisotropies should be simulated. Furthermore, the influence of the contact angle could be investigated.

Sharp interface comparison

In view of the anisotropic case, the convergence towards the exact solution in view of ϵ and the grid size should be studied. Then it would be interesting to compare to simulations of the corresponding sharp interface model, in particular in view of the mobility, and moreover to evaluate the characteristic variables such as dewetting rate or pinch-off time and compare to the known values from the sharp interface representation, at least in the isotropic case.

Extension to 3D

Finally an extension of the model and corresponding numerical results in 3D are conceivable, which also offers the possibility to analytically study further characteristic phenomena, such as fingering instabilities or pinch-off in 3D.

Part III

THE THIN FILM MODEL

6 LINEAR STABILITY ANALYSIS

6.1 AN INTRODUCTION TO LINEAR STABILITY ANALYSIS

The basic idea and classical applications

Linear stability analysis is one of the most important tools to predict pattern formation in many phenomena in nature and technological processes. Historically, this theory has been developed to explain some of the most fundamental instabilities in hydrodynamics and other fields, such as Rayleigh-Bénard convection or vortices in Taylor-Couette flow, to name only two examples. The basic idea is to assume that the emergence of a pattern is initiated by infinitesimally small perturbations of a typically uniform base state, which then evolve according to a linearized system of model equations. If the shape of the base state is constant in time, the coefficients of the linearized problem are time-independent and the general solution can be constructed, in principle, from the knowledge of the spectrum of the operator that describes the linearized model. If the spectrum extends into the right half of the complex plane, some components of a generic perturbation (arising in practice as noise, for example) will grow, typically exponentially, thus driving the system into a new state. Moreover, the part of the spectrum with the largest real part will eventually dominate the evolving features and e.g. determine the wavelength of periodic patterns. This approach is commonly called normal modes analysis and has shown to be an accurate method for a vast range of stability problems.

Transient growth

However, this concept has to be reconsidered for problems where the corresponding eigenvalue problem has non-orthogonal eigenfunctions i.e. the linearized operator is non-normal. In this case, even if all of the corresponding eigenvalues, or growth rates, are negative, perturbations may still be amplified arbitrarily large. This is known as transient growth and has been established as a mechanism that can give sufficiently large amplitude corrugations to destabilize the system by exciting non-linear effects [14, 41, 45]. In fact, it was shown in [108] that transient growth can be investigated within the framework of pseudo-spectra of the corresponding linear system. Since then, these ideas have been put to fruitful use in many (in)stability problems, e.g. in fingering problems for thin films [6, 47] or in Rayleigh-Bénard-Marangoni convection [25].

Non constant base states

Furthermore, for many stability problems the corresponding base states are not constant and the normal modes analysis fails for that reason. To still get information on the dominant wavelength of the instability, amplifications of the initial condition can be computed

numerically by solving the linearized system directly, i.e. as an initial value problem, in some cases combined with an optimal control approach to find the perturbation that leads to the largest amplification and therefore dominates the features of the instability [25, 29, 111]. This essentially takes up the idea of transient growth for non-normal operators, see also [102]. Although, in principle, it is possible to numerically proceed in this way, it is desirable to recover the type of insight into the mathematical structure of the instability that is usually provided by spectral analysis for time-independent base states.

"Frozen mode" stability analysis

In the literature, a frequently used approach for time-dependent stability problems is the quasi-stationary or so-called "frozen-mode" approximation where the time-dependence appearing in the coefficients of the linearized system is treated as a parameter. For each value of this parameter, the eigenvalues are inspected with respect to their position in the complex plane. This has been described in a series of articles in [1, 66] for a receding free film problem or [72] for evaporating the solutal Marangoni instability. Difficulties arise if the system changes significantly during the evolution of the perturbation, for example, if the frozen mode analysis has unstable modes at the beginning which become stable later on. More generally, the problem with this approach is that it completely ignores the influence of the changing base state on the history of the perturbation.

Methods exploiting multiple scales

An alternative to this quasi-stationary approach is provided if the base state changes slowly compared to the time scale of the linearized system. Then a multiple scale method can be used to incorporate the change into an approximation of the evolution of the perturbation. In this direction a recent paper by Hennessy et al. [44] develops an extension of the multiple-scale method for a parabolic convection-diffusion equation with slowly and non-periodically changing coefficients and a slowly moving boundary that has been derived from a model for Bénard-Marangoni convection in a liquid layer of a volatile solvent and a non-volatile polymer. There, the connection between the eigenvalues of the momentary system and the amplification of an initial perturbation was derived via a multiple-scale method making use of the time-scale separation between the fast diffusive time scale which is relevant for the perturbation and the slow change of the concentration and thickness of the layer in the base state. The derivation included higher corrections in order to assess the validity of the asymptotic expansion. Alternatively, an asymptotic approximation via a WKB ansatz has been given in [43] and for the case of Rayleigh-Bénard convection with time dependent heating a similar approach was investigated in [69].

Linear stability for thin film problems

The aim of this chapter is to introduce a linear stability analysis for a family of thin film problems which includes the multiscale aspects that arise from the time dependence of the base states. This method represents an improvement compared to the standard procedure and

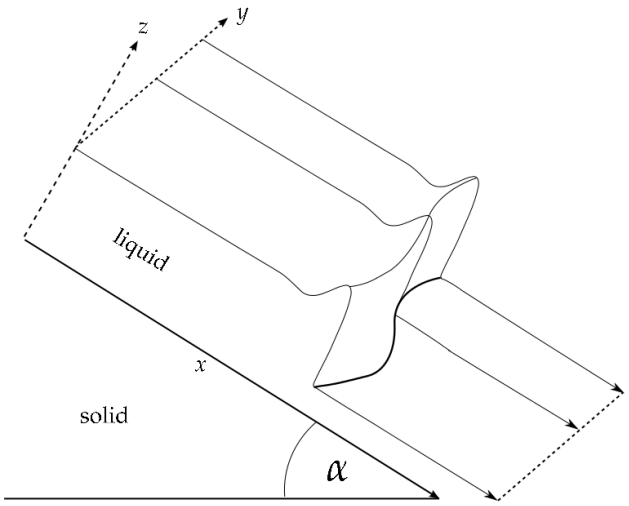

Figure 16: A sketch of a liquid film spreading down an inclined plane with a sinusoidal perturbation in the spanwise (y-) direction.

as such it is advantageous to recall the main steps of the classical stability analysis. This motivates the following section which demonstrates the standard method on the base of an example.

6.1.1 *The classical linear stability analysis- An example*

Fingering instabilities of a driven liquid film

We consider the instability of the profile for a liquid film spreading down an inclined plane. As experimentally studied by Huppert [48], the flow front develops a series of small amplitude waves of characteristic constant wavelength across the slope. The amplitude of the waves increases in time as the maxima travel faster than the minima, while the wavelength of the instability remains unaltered. These fingering instabilities have already been studied in several papers, for instance in [109] or [6], and offer a good example in order to demonstrate the procedure of the classical linear stability analysis.

Model formulation

We assume that the fluid flows down the plane in the x direction, the profile is parameterized by a height $h(x, y, t)$ in the z direction, and the fingers occur as an instability in the y direction (see Figure 16). In the presence of both gravity and surface tension, the height profile, $h(x, y)$, is obtained from the solution of the height-averaged continuity equation

$$\partial_t h + \partial_x(h^3) + \nabla \cdot \left(h^3 \nabla \Delta h - D(\alpha) h^3 \nabla h\right) = 0, \tag{257}$$

where α is the inclination angle, $D(\alpha) = \cot(\alpha) \times (3Ca)^{1/3}$ and Ca is the capillary number. The far field conditions after nondimensionalization read

$$h \to 1, \quad \text{as } x \to -\infty \qquad \text{and} \quad h \to b, \quad \text{as } x \to \infty. \tag{258}$$

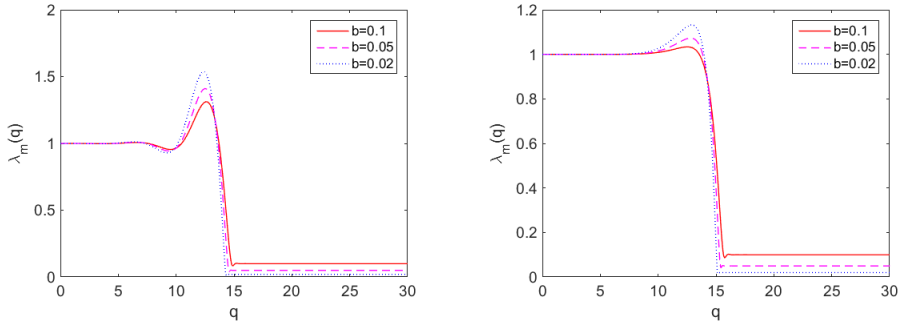

Figure 17: Base state profiles for $b = 0.1$, $b = 0.05$ and $b = 0.02$. The first graph shows the case $D = 0$ and the second $D = 2.5$. Note that the height of the bump becomes smaller for larger values of D or b.

Following the model proposed by Troian et al. [109] we assume that there exists a thin film of height b ahead of the contact line, which relieves the singularities due to the no slip boundary conditions. A justification of this assumption can be found in [6].

The base state

Step 1: Solve the equation for the base state

The base state before the instability [109] is a so-called traveling wave solution $h_b(x - Vt)$, which is constant in the y-direction, moves with constant velocity V in x-direction and satisfies

$$-Vh_b + h_b^3 + h_b^3 \partial_{xxx} h_b - D(\alpha) h_b^3 \partial_x h_b = d, \tag{259}$$

where d is a constant of integration. Evaluating (259) over $(-\infty, x]$ and including the matching conditions (258) uniquely fixes V and d to be

$$V = \frac{1 - b^3}{1 - b}, \qquad \text{and} \quad d = -b\frac{1 - b^2}{1 - b}. \tag{260}$$

Numerical evaluation

Given b and D, the equation for the base state (259) can be solved and provides the shape of the traveling wave. The resulting system is discretized in space using standard centered finite differences on an equidistant grid (with a typical grid spacing $\Delta x = 0.1$) with a (fully implicit) Euler scheme. Figure 17 shows the profiles for different values of b and D. The evaluation shows that the height of the bump strongly depends on b and D. In the following we will see that the length scale of the instability is given by the characteristic width of this bump.

Linear stability analysis

Step 2: Consider a moving reference frame

We now present the traditional approach to hydrodynamic stabilit,y which is via a linearization of the equation about the base state followed by an eigenvalue analysis of the linearized problem. The first step is to reformulate the problem in a reference frame moving with

the speed of the traveling wave, i.e. we transform to $\tilde{x} = x - Vt$, so that after dropping the tilde, equation (257) reads

$$\partial_t h - V\partial_x h + \partial_x(h^3) + \nabla \cdot \left(h^3 \nabla \Delta h - D(\alpha) h^3 \nabla h\right) = 0. \tag{261}$$

Step 3: Introduce linear perturbations..

Then we introduce linear perturbations to the base state, i.e. we consider the ansatz

$$h(x, y, t) = h_b(x) + \epsilon h_1(x, y, t), \tag{262}$$

with $0 < \epsilon \ll 1$ and a perturbation $h_1(x, y, t)$, with normalized initial height. Applying (262) in (261) and considering only the $O(\epsilon)$ contribution reveals the linear stability problem

$$\begin{aligned} 0 =& \partial_t h_1 - V\partial_x h_1 + \partial_x(3h_b^2 h_1) + \nabla \cdot \left(h_b^3 \left(\nabla \Delta h_1 - D(\alpha) \nabla h_1\right)\right) \\ &+ \partial_x \left(3h_b^2 h_1 \left(\partial_{xxx} h_b - D(\alpha)\partial_x h_b\right)\right). \end{aligned} \tag{263}$$

..and transform into Fourier space

Transformation of the y-direction into Fourier space

$$h_1(x, y, t) = \int_{-\infty}^{\infty} \hat{h}_1(x, t; q) \, \exp(iqy) \, dq, \tag{264}$$

enables to consider equation (263) for each wavenumber q

$$\begin{aligned} 0 =& \partial_t \hat{h}_1 - V\partial_x \hat{h}_1 + \partial_x(3h_b^2 \hat{h}_1) + \partial_x \left(h_b^3 \left(\partial_{xxx} - D(\alpha)\partial_x\right) \hat{h}_1\right) \\ &- q^2 \left(\partial_x \left(h_b^3 \partial_x \hat{h}_1\right) + h_b^3 \left(\partial_{xx} - D(\alpha)\right) \hat{h}_1\right) + q^4 h_b^3 \hat{h}_1 \\ &+ \partial_x \left(3h_b^2 \hat{h}_1 \left(\partial_{xxx} h_b - D(\alpha)\partial_x h_b\right)\right). \end{aligned} \tag{265}$$

Furthermore we need to provide an initial perturbation for each wavenumber q, which we define as

$$\hat{h}_1(x, t_0; q) =: \hat{h}_{1,t_0}(x, q). \tag{266}$$

Step 4: Separate the variables and solve the eigenvalue problem

The next step is to separate the variables, i.e. for each fixed wavenumber q we apply the ansatz

$$\hat{h}_1(x, t; q) = \Psi(x; q) T(t). \tag{267}$$

Without loss of generality we may assume that $\hat{h}_1 \neq 0$. Applying (267) in (265) and dividing by $\Psi(x)T(t)$ then reveals

$$\begin{aligned} \frac{\partial_t T}{T} =& \frac{V\partial_x \Psi - \partial_x(3h_b^2 \Psi) - \partial_x \left(h_b^3 \left(\partial_{xxx} - D(\alpha)\partial_x\right) \Psi\right)}{\Psi} \\ &+ \frac{q^2 \left(\partial_x \left(h_b^3 \partial_x \Psi\right) - h_b^3 \left(\partial_{xx} - D(\alpha)\right) \Psi\right) - q^4 h_b^3 \Psi}{\Psi} \\ &- \frac{\partial_x \left(3h_b^2 \Psi \left(\partial_{xxx} h_b - D(\alpha)\partial_x h_b\right)\right)}{\Psi}. \end{aligned} \tag{268}$$

Observing that the left hand side is independent of x and the right hand side is independent of t, we conclude that there exists $\lambda \in \mathbb{C}$ such that

$$\partial_t T = -\lambda T \quad \text{(P1)}, \qquad \text{and} \qquad \mathcal{L}_q \Psi = \lambda \Psi \quad \text{(P2)}, \tag{269}$$

where $\mathcal{L}_q$ is the linear operator

$$\begin{aligned}\mathcal{L}_q\Psi =& V\partial_x\Psi - \partial_x(3h_b^2\Psi) - \partial_x\left(h_b^3\left(\partial_{xxx} - D(\alpha)\partial_x\right)\Psi\right)\\ &+ q^2\left(\partial_x\left(h_b^3\partial_x\Psi\right) - h_b^3\left(\partial_{xx} - D(\alpha)\right)\Psi\right) - q^4h_b^3\Psi\\ &- \partial_x\left(3h_b^2\Psi\left(\partial_{xxx}h_b - D(\alpha)\partial_x h_b\right)\right).\end{aligned} \tag{270}$$

Realizing that (P1) has the solution

$$T(t) = T_0\exp(\lambda t), \tag{271}$$

where λ is an eigenvalue of the linear operator $\mathcal{L}_q$, and (P2) is solved by a superposition of the eigenfunctions Ψ_λ of $\mathcal{L}_q$, the solution (267) becomes

$$\hat{h}_1(x,t;q) = \sum_\lambda a_\lambda(q)\exp(\lambda t)\Psi_\lambda(x;q), \tag{272}$$

where the coefficients $a_\lambda(q)$ correspond to the coefficients of the initial perturbation for each wavenumber q

$$\hat{h}_{1,t_0}(x,q) = \sum_\lambda a_\lambda(q)\Psi_\lambda(x;q). \tag{273}$$

Note that we assumed that the initial perturbation $\hat{h}_{1,t_0}$ may be represented by a superposition of eigenfunctions of the linear operator $\mathcal{L}_q$, which is reasonable since we are interested in perturbations which are amplified the most and these are clearly found among the eigenfunctions of the linear operator $\mathcal{L}_q$. Furthermore, we would like to note that, depending on the properties of the operator $\mathcal{L}_q$, the sum over λ may be infinite or even not discrete, i.e. an integral.
Rearranging the entire solution (264), we obtain

$$h_1(x,y,t) = \int_{-\infty}^{\infty}\sum_\lambda a_\lambda(q)\exp(\lambda t + iqy)\Psi_\lambda(x;q)\ dq. \tag{274}$$

Step 5: Evaluate the dispersion relation

Considering the evolution of this solution it becomes clear that the eigenfunctions corresponding to the eigenvalue with maximal real part will be amplified at most and in fact exponentially in time. Moreover for each wavenumber q there exists an eigenvalue $\lambda_M(q)$ of $\mathcal{L}_q$ which has maximal real part and the function $\lambda_M : \mathbb{R}^+ \to \mathbb{R}$ is called dispersion relation. This function is the characteristic variable which is typically evaluated in a linear stability analysis.
The eigenvalues $\lambda_M(q)$ as a function of q are then determined by solving the full linear PDE (265) for each q. Choosing a generic initial condition and considering

$$\frac{d}{dt}\ln\left[\|\hat{h}_1(\cdot,t;q)\|_\infty\right] = \lambda_M(q), \tag{275}$$

after a sufficient long time provides the exponential growth or decay rate. The numerical scheme is a standard implicit finite-difference scheme, see e.g. [5], where the only difficulty is that considering small

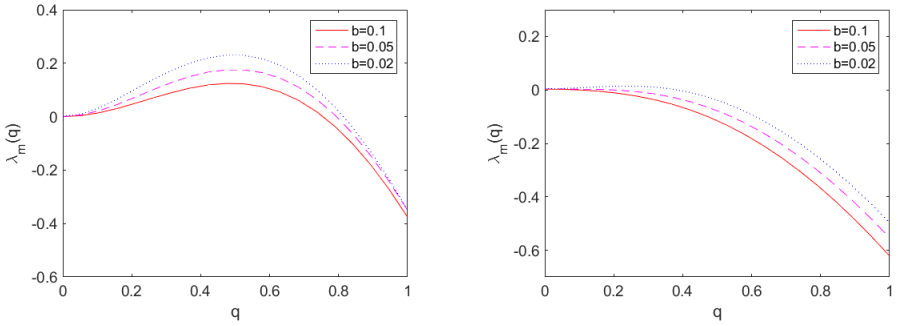

Figure 18: Dispersion relation for $b = 0.1$, $b = 0.05$ and $b = 0.02$. The first graph shows the case $D = 0$ and the second $D = 2.5$.

values of b requires to use a non-uniform mesh with refinement at the apparent contact line in order to completely resolve the unperturbed profile h_b. Figure 18 shows $\lambda_M(q)$ for different values of b and for $D = 0$ and $D = 2.5$. In both cases, the dominant wavelengths turn out to be less stable for smaller values of D or b which is in qualitative agreement with the results given in [109] and [6].

6.1.2 *Long wave analysis*

In addition to the evaluation of the dispersion relation $\lambda_M(q)$ from the linearized PDE (265), the analysis of the stability problem can be continued in view of a long wave asymptotic analysis. Realizing that the wavelength l_λ is inversely proportional to the wavenumber q, i.e. $l_\lambda \propto 1/q$, this suggests asymptotic expansions in view of the small parameter q

$$\begin{aligned} \hat{h}_1 &= \hat{h}_{1,0} &&+ q^2\hat{h}_{1,1} &&+ O(q^4) \\ \lambda_M(q) &= \lambda_M(0) &&+ q^2\lambda_M(q^2) &&+ O(q^4). \end{aligned} \tag{276}$$

Note that we have chosen quadratic expansions in q because only quadratic orders of q appear in (265). Moreover, the numerical evaluation, see Fig. 18, suggests quadratic behavior of λ_M in q near $q = 0$. The leading order problem of (265) then becomes

Translational mode to leading order

$$\begin{aligned} \lambda_M(0)\hat{h}_{1,0} = &- V\partial_x\hat{h}_{1,0} + \partial_x(3h_b^2\hat{h}_{1,0}) + \partial_x\left(h_b^3\left(\partial_{xxx} - D(\alpha)\partial_x\right)\hat{h}_{1,0}\right) \\ &+ \partial_x\left(3h_b^2\hat{h}_{1,0}\left(\partial_{xxx}h_b - D(\alpha)\partial_x h_b\right)\right). \end{aligned} \tag{277}$$

From the far field conditions (258) we conclude that $\lambda_M(0) = 0$ and recalling (259) reveals

$$\hat{h}_{1,0} = \partial_x h_b. \tag{278}$$

Note that (278) implies that $\hat{h}_{1,0}$ is as well as h_b constant in the y-direction and the corresponding particular instability is called translational mode.

Proceeding to $O(q^2)$ we find

$$\begin{aligned}\lambda_M(q^2)\partial_x h_b = &- V\partial_x\hat{h}_{1,1} + \partial_x(3h_b^2\hat{h}_{1,1}) + \partial_x\left(h_b^3\left(\partial_{xxx} - D(\alpha)\partial_x\right)\hat{h}_{1,1}\right)\\ &- q^2\left(\partial_x\left(h_b^3\partial_{xx}h_b\right) + h_b^3\left(\partial_{xx} - D(\alpha)\right)\partial_x h_b\right)\\ &+ \partial_x\left(3h_b^2\hat{h}_{1,1}\left(\partial_{xxx}h_b - D(\alpha)\partial_x h_b\right)\right).\end{aligned} \tag{279}$$

Integrating in x over $(-\infty,\infty)$ and exploiting the far field conditions then leads to

$$\begin{aligned}\lambda_M(q^2)(b-1) &= \int_{-\infty}^{\infty} h_b^3\left(\partial_{xxx}h_b - D(\alpha)\partial_x h_b\right)\\ &= \int_{-\infty}^{\infty} d + Vh_b - h_b^3\\ &= \int_{-\infty}^{\infty} -b - b^2 + (1+b+b^2)h_b - h_b^3\\ &= \int_{-\infty}^{\infty} -(h_0-1)(h_0-b)(h_0+1+b),\end{aligned} \tag{280}$$

where again we exploited (259) and furthermore the identities

$$d = -b - b^2, \quad \text{and} \quad V = 1 + b + b^2.$$

Characterization of λ_M for long wavelengths

At this point we conclude from the long wave analysis that

$$\lambda_M(\beta) \;=\; \frac{\beta^2}{1-b}\int_{-\infty}^{\infty}(h_0-1)(h_0-b)(h_0+1+b) \;+\; O(q^4), \tag{281}$$

where the main message is, that if the base state h_b satisfies $h_b \leq 1$, then $\lambda_M(\beta) \leq 0$ at long wavelengths which implies linear stability of the dewetting front. Otherwise, in order to observe a positive dispersion relation $\lambda_M(\beta)$, the base state h_b must be greater than one on a sufficiently large subset of $\mathbb{R}$, such that the positive part of the integral (281) cancels out the negative part. Consequently the size of the bump of h_b significantly influences the type and strength of the instability, at least for long wavelengths.

6.1.3 *Why the classical stability analysis fails in the case of non-constant base states*

What if the base state evolves in time?

The previous section has demonstrated how the size and shape of the base state may significantly influence the instability, at least for long wavelengths, as concluded from (281). Now imagine that the base state evolves in time and perhaps even provides a growing bump. This would imply that also the dispersion relation would evolve in time and each "frozen" base state would have a different dominant wavenumber. Even if the evolution of the base state occurs on a much slower time-scale than the characteristic instability, the history of the instability should not be neglected.

6.2 A NEW APPROACH FOR THE STABILITY ANALYSIS IN THIN FILM EQUATIONS

The thin film equations

We are now in the position to proceed to the main part of this chapter, which is the stability analysis of unsteady, non-uniform base states. In particular we will present a linear stability analysis for the family of thin film problems characterized by degenerate or non-degenerate parabolic equations

$$h_t + \nabla \cdot (h^n \nabla \Delta h) = 0, \tag{282}$$

with $0 \leq n < 3$, where we will present detailed analytical and numerical results for the cases $n = 0$ and $n = 2$, or $3/2 < n < 3$ respectively, wherever possible. In general, this class of problems arises from mass conserving free boundary problems for the thin film height h. When an extended film is deposited onto a partially wettable substrate and then retracts after an initial rupture event has created a hole, the growing rim of the hole develops undulations along its spanwise direction [9, 10, 31, 96]. The value of n here depends on the condition imposed at the liquid-solid substrate.

Characterization of the evolution

The critical case $n = 3$

It is well known that modeling the contact line is a very difficult topic. For $n = 3$, for example, stress singularities near the contact line have to be taken into account due to the no-slip boundary condition. This case already occurred in the introductory example, see Section 6.1.1, and was resolved via a method proposed by [109], thus via including a thin film ahead of the contact line, referred to as precursor, which is much smaller than the typical height of the film. This technique also applies to other values of n, where the precursor film commonly represents the characteristic microscopic physics in a particular experiment [6, 58, 86].

$n < 3$, moving boundaries

For large slip, which arises at the liquid/solid boundary as a manifestation of the non-Newtonian flow properties in shearing polymer films, the value is $n = 2$ [86]. For this value of n, and in fact for all non-negative $n < 3$, imposing a fixed contact angle and a no-flux condition at $h = 0$ leads to a problem formulation that is consistent with a moving contact line [35, 57]. For $n = 2$, undulations evolve into a characteristic finger–like pattern [84].

The case $n = 0$, solid state dewetting

Rims of retracting solid films are susceptible to a similar instability which occurs in various practical applications. It can, for instance, be observed when thin silicon films are annealed and lead to the formation of fingering instabilities in the $\langle 100 \rangle$ oriented front [65]. The fingers break down and form nanoislands at regular intervals, a process that is used in the fabrication of advanced nanodevices [51, 61]. Formation of protrusions and pinch-off are also observed in experiments with gold films [53]. For interfaces of solids subject to surface diffusion [18, 55, 76, 81, 114], the material flux arises from gradients of the curvature-dependent chemical potential, leading to a

fourth order, non-linear equation for the evolution of the solid surface. Despite the different transport mechanism – surface diffusion [81] – the mathematical model governing the evolution of the height h again leads to a differential equation of form (282) but with $n = 0$. At the contact line, a fixed contact angle and no flux are commonly imposed as boundary conditions.

The "frozen mode" stability analysis for this class of equations

Since the thickness of the flat film into which the rim moves is assumed to be constant, while the rim itself grows, the time dependence cannot be removed by a single choice of self-similar coordinates. Thus, the linearization leads to a problem with time-dependent coefficients which have been approached by different authors. In [55], the linear stability of a rim in a solid film retracting under surface diffusion is addressed by a "frozen mode" analysis where the time dependence of the coefficients in the linearized problems is treated as a parameter.

WKB stability analysis

Another approach was pursued in [84] for liquid dewetting, where the initial value problem resulting from the linearization was solved numerically to track the amplification of a perturbation. On the other hand, for long times, the leading order outer problem for the rim admits a traveling wave solution [35, 58], since the inflation of the rim is slow once it has become large compared to the unperturbed film. If this growth is neglected, the traveling wave solution can be treated as stationary in a suitably chosen co-moving frame of reference and a normal-mode ansatz is possible again. Using scaling arguments to take into account the evolving base state, the amplification of a perturbation was inferred from the resulting spectrum [58, 85]. A related approach was followed for a model of anisotropic solid dewetting in [27].

In this study we will develop a systematic WKB analysis to determine the evolution of a perturbation which appears at a moving contact line. The presented method applies to the class of thin film equations (282), where $0 \leq n < 3$, commonly known to model thin films with large slip lengths or solid films where surface diffusion is dominant. For these problems our approximation remains valid on the long time scale of the changing system, and is used to derive in particular the wave number of the most amplified perturbation. This wave number is different from the most growing one in a frozen-mode approach and is rapidly attained once the base state has entered an approximately self-similar scaling. Moreover the asymptotic solution for the dispersion relation in the long wave limit reveals that the dependence of the growth rate on the wave number is linear, whereas in many other capillary instability problems it is quadratic, such as in the introductory example given in Section 6.1.1.

Overview of this chapter

This main part of the present chapter is organized as follows. After formulating the free boundary problem for (282) in Section 6.3, we introduce the long-time asymptotics for the base state in Section 6.4. Detailed analytical and numerical results, referring to this and the

following subsections, are presented for the cases $n = 0$ and $n = 2$, or $3/2 < n < 3$ respectively, wherever possible. In Section 6.5, a WKB approximation for the associated linearized problem is developed and used to determine the most amplified mode and its wavenumber. Finally, we summarize our results in Section 5.

6.3 MODEL FORMULATION

We consider an evolution problem for the film profile $z = h(x, y, t)$, given for $t > 0$ by the PDE (282) on the time-dependent domain $\Omega = \{(x, y);\, s(y, t) < x < \infty,\ -\infty < y < \infty\}$ and by appropriate conditions at the free boundary and in the far field, namely

$$h = 0\,, \qquad x = s(y,t) \tag{283a}$$

$$\nabla h \cdot \mathbf{n}_s = \theta\,, \qquad x = s(y,t) \tag{283b}$$

$$h^n \left(\nabla \Delta h \cdot \mathbf{n}_s\right) = 0\,, \qquad x = s(y,t) \tag{283c}$$

$$\lim_{x\to\infty} h = 1. \tag{283d}$$

The first three equations represent, respectively, the presence of a contact-line with fixed slope θ and no flux at $x = s(y, t)$, and the last condition prescribes that we have a flat film at $x \to \infty$, with a thickness that has been scaled to one. Here,

$$\mathbf{n}_s = (1, -\partial_y s)/\left(1 + (\partial_y s)^2\right)^{1/2}$$

is the normalized normal vector along $x = s(y, t)$ in the (x, y)- plane pointing into Ω, as sketched in Figure 19. The initial conditions

$$h(x, y, 0) = h_i(x, y), \quad s(y, 0) = s_i(y), \tag{284}$$

are assumed to be chosen consistent with (283). We note that the interval $0 \le n < 3$ subdivides into essentially three separate cases, $n = 0$, $0 < n \le 3/2$, and $3/2 < n < 3$. The first one is instructive, because the PDE is linear and therefore the analytic results can be carried out much further. Whereas it has a simple asymptotic structure, the rim profile pinches off after a finite time. While for $n > 3/2$ this does not happen, the film profile decomposes into different asymptotic scaling regimes that need to be matched. The intermediate case combines both features and is not pursued here further since it does not add to the discussion of the stability analysis.

Distinction between the different cases concerning n

6.4 BASE STATE

We consider a time-dependent base state $h_b = h_b(x, t)$ which is constant in the y-direction and has a straight contact line $s_b = s_b(t)$. We transform to a coordinate system moving with the contact line via

Step 1: Solve the equation for the base state

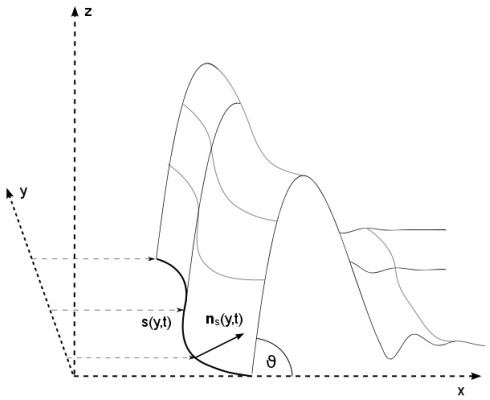

Figure 19: A sketch of a retracting rim with a sinusoidal perturbation in the spanwise (y-) direction.

$h_b(x,t) = \tilde{h}_b(\tilde{x},t)$, $\tilde{x} = x - s_b(t)$, so that after dropping the tilde, we have

$$\partial_t h_b - \dot{s}_b\,\partial_x h_b + \partial_x\left(h_b^n\,\partial_{xxx} h_b\right) = 0\,, \quad \text{for } x \geq 0, \tag{285a}$$

$$h_b = 0\,, \quad \partial_x h_b = \theta\,, \quad h_b^n\,\partial_{xxx} h_b = 0\,, \quad \text{at } x = 0, \tag{285b}$$

$$\lim_{x\to\infty} h_b = 1\,. \tag{285c}$$

Notice that due to mass conservation, h_b satisfies

$$\int_0^\infty h_b(x,t) - h_b(x,0)\; dx = s_b(t). \tag{286}$$

Notes on the numerical evaluation

In fact, an equivalent formulation of (285) that we use as the basis for the numerical discretization is achieved by replacing the third condition in (285b) by (286). The domain is truncated at $x = L_\infty$, where L_∞ is chosen large enough so that the growing rim structure is accommodated up to the desired time, typically much larger than 100. The resulting system is discretized in space using standard centered finite differences on an equidistant grid (with a typical grid spacing $\Delta x = 0.1$), and a trapezoidal rule for (286), and in time with a (fully implicit) Euler scheme. The latter is combined with step doubling and extrapolation for higher accuracy and time step control. For the initial conditions, we used a smoothed Heaviside profile

$$s_b(0) = 0, \qquad h_b(x,0) = \begin{cases} 1 - \theta(x-1)^2/2 & \text{for } 0 \leq x \leq 1, \\ 1 & \text{for } x \geq 1. \end{cases} \tag{287}$$

Long time solution

Slow time-scale τ for the evolving basestate

Consistent with the analysis in [35, 57, 76, 86], the numerical solutions show that for long times, $t \to \infty$, the position of the contact line s_b and

the maximum height of the rim evolve according to a power law, see figs. 20(b) and 21(b). We briefly summarize and adapt the previous results to the case studied here and compare with the numerical results.

To capture the long time behavior analytically, we introduce a second time-scale $\tau = \delta t$, where $\delta \ll 1$, and consider the limit $\delta \to 0$ with τ fixed. The observed power law behavior suggests rescaling s_b by $\delta^{-\sigma}$, where the exponent $\sigma > 0$ needs to be determined. Mass conservation (286) and the assumption that height and width of the rim rescale identically then motivates the choices

$$s_b(t) = \delta^{-\sigma} S_b(\tau)\,, \quad x = \delta^{-\sigma/2} X, \quad h_b = \delta^{-\sigma/2} H_b. \tag{288}$$

Inserting these scalings into (285a) reveals that only the second and third terms can be balanced (the scaling of the term with the time derivative always being much smaller than the other two), and this balance implies $\sigma = 2/(5-n)$. Thus, the rescaled equations read

Rescaled system for the base state

$$\delta^{1/(5-n)} \partial_\tau H_b - \dot{S}_b\, \partial_X H_b + \partial_X \left(H_b^n \partial_{XXX} H_b \right) = 0\,, \quad \text{for } X \geq 0, \tag{289a}$$

$$H_b = 0, \quad \partial_X H_b = \theta, \quad H_b^n \partial_{XXX} H_b = 0\,, \quad \text{at } X = 0, \tag{289b}$$

$$\lim_{X \to \infty} H_b = \delta^{1/(5-n)}\,, \tag{289c}$$

where we remark that the dot over S_b now denotes derivatives with respect to τ. Next, we expand

$$H_b(X, \tau; \delta) = H_{b,0}(X, \tau) + O(\delta^{1/(5-n)}), \quad S_b(\tau; \delta) = S_{b,0}(\tau) + O(\delta^{1/(5-n)}). \tag{290}$$

The leading order problem is given by (289a) and (289b) after dropping the $\delta^{1/(5-n)}$ term that appears in the ODE. Integrating and using the leading order boundary conditions

$$H_{b,0} = 0, \quad \partial_X H_b = \theta, \quad H_{b,0}^n \partial_{XXX} H_{b,0} = 0, \quad \text{at } X = 0, \tag{291}$$

then yields

$$H_{b,0}^{n-1} \partial_{XXX} H_{b,0} = \dot{S}_{b,0}\,. \tag{292}$$

Notice that θ and $\dot{S}_{b,0}$ can be removed from (291) and (292) by rescaling

$$X = \theta^{n/(3-n)} \frac{\xi}{\dot{S}_{b,0}^{1/(3-n)}}, \qquad H_{b,0} = \theta^{3/(3-n)} \frac{\phi_b}{\dot{S}_{b,0}^{1/(3-n)}}. \tag{293}$$

Case $\boldsymbol{n = 0}$

In this case, we simply can use the leading order version of the condition (289c) in the far field,

Base state for $n = 0$

$$\lim_{X \to \infty} H_{b,0} = 0, \tag{294}$$

The boundary value problem (291), (292) and (294) is linear and has the solution

$$H_{b,0}(X,\tau) = \frac{2}{\sqrt{3}}\frac{\theta}{\dot{S}_{b,0}^{1/3}} \exp\left(-\frac{\dot{S}_{b,0}^{1/3}X}{2}\right) \sin\left(\frac{\sqrt{3}}{2}\dot{S}_{b,0}^{1/3}X\right), \tag{295}$$

Moreover, to leading order, we obtain from (286)

$$\int_0^\infty H_{b,0}\, dx = S_{b,0}. \tag{296}$$

Inserting the solution for $H_{b,0}$ yields a differential equation for $S_{b,0}$,

$$S_{b,0}^3\, \dot{S}_{b,0}^2 = M\theta^3, \tag{297}$$

where

$$M \equiv \left(\int_0^\infty \phi_b\, d\xi\right)^3, \tag{298}$$

and assuming that $S_{b,0}(0) = 0$ gives the solution

$$S_{b,0} = (5/2)^{2/5}\, \theta^{3/5}\tau^{2/5}. \tag{299}$$

Written in the original variables, we have for large t

$$s_b \sim (5/2)^{2/5}\, \theta^{3/5}t^{2/5} = 1.44\, \theta^{3/5}t^{2/5}. \tag{300a}$$

Furthermore, for the maximum of the base state $\max_x h_b$ and the value of $x = x_m(t)$ where it is achieved, we obtain

$$\max_x h_b(x,t) \sim (2/5)^{-1/5}\, \mathrm{e}^{-ß/\sqrt{27}\backslash 4/5}\, \mathrm{t}^{1/5} = 0.656^{\backslash 4/5}\, \mathrm{t}^{1/5} \tag{300b}$$

$$x_m(t) \sim \frac{\pi}{\sqrt{27}}\, 2^{4/5}\, 5^{1/5}\, \theta^{-1/5}\, t^{1/5} = 1.45\, \theta^{-1/5}\, t^{1/5}. \tag{300c}$$

Numerical evaluation

The numerical profiles for H_b are shown in fig. 20(a). The film quickly forms a capillary rim that grows for large times in an approximately self-similar fashion, except in the far-field which is constant, with approximately the same scaling factor for the height and the width so it maintains a fixed contact angle. Notice that at some stage, the first local minimum to the right of the rim touches zero. For the simulations shown here, with $\theta = 1$, this happens around $t = t_r \equiv 2.25 \times 10^5$, with $\max_h = 7.96$. Physically, this means that the diffusing film ruptures and sheds material that collects into an equilibrium shape while the dewetting by surface diffusion resumes with a new contact line. Nevertheless, the mathematical formulation does allow for solutions that are negative and in order to understand the long time asymptotic structure, it is convenient to investigate these solutions beyond t_r. Since the rupture occurs for large t, we can expect the asymptotic solutions to yield reasonable approximations even for a range of $t < t_r$. Indeed, all three asymptotic approximations (300a), (300b), (300c) agree well with the numerical results for sufficiently large t, as can be seen in fig. 20(b).

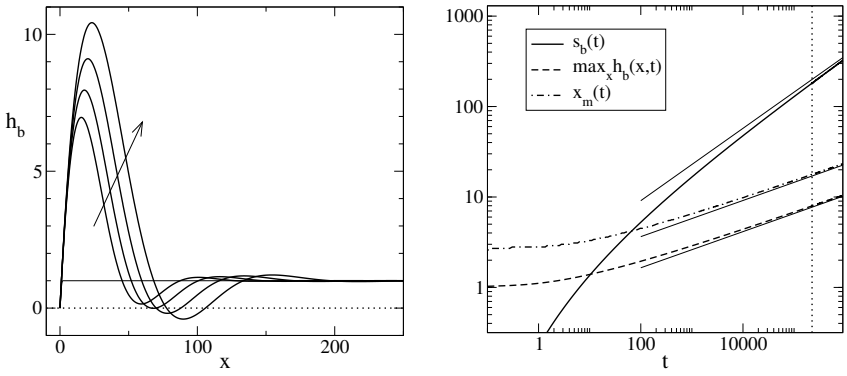

Figure 20: (a,left) Profiles of the base state for $\theta = 1$ at different times, obtained by solving (285) numerically (using (286) instead of the third boundary condition in (285b)), for $\theta = 1$ and $n = 0$. The initial data (287) is shown by a thin solid line, later times by thicker solid lines, for $t = t_r/2$, $t = t_r$, $2t_r$, $4t_r$, where $t_r \equiv 2.25 \times 10^5$ is the time at which the first minimum of the profile to the right of the rim hits zero. All profiles are shown in a co-moving frame of reference with the contact line fixed at the origin. (b,right) Evolution of the contact line, s_b, the maximum value $\max_x h$ and the position x_m where the maximum is achieved. The thin straight lines are the asymptotic results (300). The thin dotted vertical line indicates the rupture time $t = t_r$. Figure published in [28].

Case $n > 3/2$

Base states for $3/2 < n < 3$

Note that in this case, the rim decomposes into different scalings where the rim takes on the role of the outer solution and needs to be matched to further layers on the right. The details of this matching depend on n and are quite intricate in general [57]. For $n = 2$, there is just one inner layer and the matching approach for this particular value of n has been presented in [35, 86]. However the procedure can be generalized to $3/2 < n < 3$, which is carried out in the following.

Matching conditions for $3/2 < n < 3$

Let $w_b(t)$ be the width of the moving rim in (285) and let $w_b(t) = \delta^{-1/(5-n)} W_b(\tau)$ be the corresponding rescaled variable, according to the assumption that width and height of the rim scale identically. We define the boundary layer by

$$x = \delta^{-1/(5-n)} W_b(\tau) + \delta^{-\mu} \chi \,, \tag{301}$$

with χ being the inner variable, where the scaling exponent μ remains to be determined. Apply (288) for s_b while in the inner region h_b is not rescaled and consequently the far-field condition remains

$$\lim_{x \to \infty} h_b = 1 \,. \tag{302}$$

Applying (301) in (285a) we obtain

$$\delta\partial_\tau h_b - \delta^{(3-n)/(5-n)+\mu}\dot{S}_b\partial_\chi h_b - \delta^{(4-n)/(5-n)+\mu}\dot{W}_b\partial_\chi h_b + \delta^{4\mu}\partial_\chi\left(h_b^n\partial_{\chi\chi\chi}h_b\right) = 0 \tag{303}$$

suggesting the dominant balance $\mu = (3-n)/(3(5-n))$. Expanding S_b as in (290) and h_b, W_b analogously, i.e.

$$\begin{aligned} h_b(\chi,\tau;\delta) &= h_{b,0}(\chi,\tau) &&+ O(\delta^{1/(5-n)}),\\ W_b(\tau;\delta) &= W_{b,0}(\tau) &&+ O(\delta^{1/(5-n)}), \end{aligned} \tag{304}$$

yields the leading order problem

$$-\dot{S}_{b,0}\partial_\chi h_{b,0} + \partial_\chi\left(h_{b,0}^n\partial_{\chi\chi\chi}h_{b,0}\right). \tag{305}$$

Integrating once and rescaling $\chi = \xi/\dot{S}_{b,0}^{1/3}$ yields

$$(h_{b,0}-1) + h_{b,0}^n\partial_{\xi\xi\xi}h_{b,0} = 0 \tag{306}$$

with solution

$$h_{b,0}(\xi) \sim \left(\frac{n^3}{3(3-n)(2n-3)}\left(-\xi\right)^3\right)^{1/n}, \quad \text{for } \xi \to -\infty, \tag{307}$$

(in accordance with King and Bowen [57]). Hence in outer coordinates we obtain the matching condition

Matching condition in outer coordinates

$$H_{b,0}(X,\tau) \sim \left(\frac{n^3}{3(3-n)(2n-3)}\right)^{1/n}\dot{S}_{b,0}^{1/n}\left(W_{b,0}(\tau)-X\right)^{3/n} \tag{308}$$

for $X \to W_{b,0}(\tau) > 0$. Note that $W_{b,0}$ also denotes the leading order expression for the matching point in between the outer rim and undisturbed film to the right hand side.

Here, conservation of mass, according to (286), turns to leading order into

$$\int_0^{W_{b,0}(\tau)} H_{b,0}\,dx = S_{b,0}, \tag{309}$$

Inserting the scalings (293), we obtain

$$\phi_{b,0}^{n-1}\partial_{\xi\xi\xi}\phi_{b,0} = 1, \tag{310a}$$

for $0 \le \xi < d_b$, and

$$\phi_{b,0} = 0, \quad \partial_\xi\phi_{b,0} = 1, \quad \phi_{b,0}^n\partial_{\xi\xi\xi}\phi_{b,0} = 0, \qquad \text{at } \xi = 0, \tag{310b}$$

$$\phi_{b,0} \sim \left(\frac{n^3}{3(3-n)(2n-3)}\right)^{1/n}\left(d_b-\xi\right)^{3/n}, \qquad \text{for } \xi \to d_b, \tag{310c}$$

where d_b arises from rescaling $W_{b,0}(\tau)$,

$$W_{b,0}(\tau) = \theta^{n/(3-n)}\frac{d_b}{\dot{S}_{b,0}^{1/(3-n)}}. \tag{311}$$

Moreover we obtain from (309) the differential equation

$$S_{b,0}^{(3-n)}\,\dot{S}_{b,0}^{2} = M\theta^{(3+n)}, \tag{312}$$

where M is given by

$$M = \left(\int_0^{d_b} \phi_{b,0}\,d\xi\right)^{3-n}. \tag{313}$$

The differential equation (312) for $\dot{S}_{b,0}$ with $S_{b,0}(0) = 0$ has the solution

$$S_{b,0} = \left(\frac{5-n}{2}\right)^{2/(5-n)} M^{1/(5-n)}\theta^{(3+n)/(5-n)}\tau^{2/(5-n)}. \tag{314}$$

Numerical evaluation

In general, (310) has to be solved numerically. For $n = 2$, the order can be reduced by one integration and this gives $d_b = 1/2$ in the process [35, 86]; numerically, one finds $M = 2.72 \times 10^{-2}$, see [86], and from this,

$$s_b \sim 0.394\,\theta^{5/3}\,t^{2/3} \tag{315a}$$

for large t, where we have converted back to the original variables. Moreover, for the maximum of the base state $\max_x h_b$ and the value of $x = x_m(t)$ where it is achieved, we obtain

$$\begin{aligned}\max_x h_b(x,t) &\sim (2/3)^{-1/3}M^{-1/3}\max_\xi \phi_b\,\theta^{4/3}\,t^{1/3}\\ &= 0.331\,\theta^{4/3}\,t^{1/3} \qquad (315b)\\ x_m(t) &\sim (2/3)^{-1/3}M^{-1/3}\xi_m\,\theta^{1/3}\,t^{1/3}\\ &= 0.765\,\theta^{1/3}\,t^{1/3}, \qquad (315c)\end{aligned}$$

where $\max_\xi \phi_b = 0.870 \times 10^{-1}$ and $\xi_m = 0.201$ were obtained from the numerical solution for (310) computed in [86]. The agreement between asymptotical and numerical results is excellent. Notice that the first dip following the maximum in the profiles remains shallow even as the rims grow, thus showing no indication of a rupture. This is consistent with predictions that rupture does not occur for $n > 3/2$, see [35, 57].

6.5 LINEAR STABILITY

6.5.1 *Formulation*

Step 2: Consider a moving reference frame

We first shift the full problem (282) into the reference frame moving with the contact line of the base state $s_b(t)$ by using the same change of variables as for the base state equation, that is, $h(x,y,t) = \tilde{h}(\tilde{x},\tilde{y},t)$, $\tilde{x} = x - s_b(t)$, and $y = \tilde{y}$. After dropping the tildes, the PDE becomes

$$\partial_t h - \dot{s}_b\,\partial_x h + \nabla\cdot(h^n\nabla\Delta h) = 0,$$

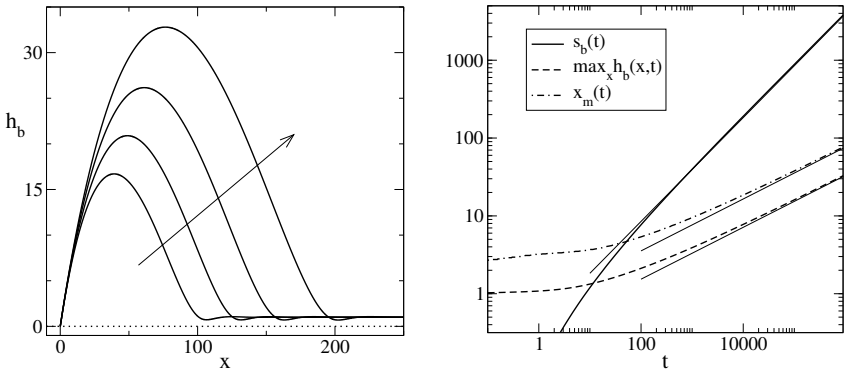

Figure 21: (a,left) Profiles of the base state for $\theta = 1$ at different times, obtained by solving (285) numerically (using (286) instead of the third boundary condition in (285b)), for $\theta = 1$ and $n = 2$. The initial data (287) is shown by a thin solid line, later times by thicker solid lines, for $t = t_{ref}/2$, $t = t_{ref}$, $2t_{ref}$, $4t_{ref}$, where $t_{ref} \equiv 2.25 \times 10^5$. All profiles are shown in a co-moving frame of reference with the contact line fixed at the origin. (b,right) Evolution of the contact line, s_b, the maximum value $\max_x h$ and the position x_m where the maximum is achieved. The thin straight lines are the asymptotic results (315), respectively. Figure published in [28].

while the boundary and far-field conditions remain unchanged. We introduce perturbations of the base state h_b and s_b of the form

Step 3: Introduce linear perturbations..

$$h(x,y,t) = h_b(x,t) + \varepsilon\, h_1(x,y,t), \qquad s(y,t) = \varepsilon\, s_1(y,t), \tag{316}$$

with $0 < \varepsilon \ll 1$ and Fourier transform,

.. and transform into Fourier space

$$\begin{aligned} h_1(x,y,t) &= \int_{-\infty}^{\infty} \hat{h}_1(x,t;q)\, \exp(iqy)\, dq, \\ s_1(y,t) &= \int_{-\infty}^{\infty} \hat{s}_1(t;q)\, \exp(iqy)\, dq. \end{aligned} \tag{317}$$

In this way we obtain, to $O(\varepsilon)$,

$$\partial_t \hat{h}_1 - \hat{\mathcal{L}}\,\hat{h}_1 = 0\,, \qquad \text{for } x \geq 0, \tag{318a}$$

$$\hat{h}_1 = -\theta \hat{s}_1\,, \quad \partial_x \hat{h}_1 = -\hat{s}_1 \partial_{xx} h_b\,, \qquad \text{at } x = 0, \tag{318b}$$

$$\begin{aligned} &h_b^n \left(\partial_{xxx}\hat{h}_1 - q^2 \partial_x \hat{h}_1\right) \\ &+ n h_b^{n-1}\, \partial_{xxx} h_b\, \hat{h}_1 - \dot{s}_b \hat{h}_1 = 0\,, \end{aligned} \qquad \text{at } x = 0, \tag{318c}$$

$$\lim_{x\to\infty} \hat{h}_1 = 0\,, \tag{318d}$$

where

$$\begin{aligned} \hat{\mathcal{L}}\,\hat{h}_1 \;\equiv\; & \dot{s}_b \partial_x \hat{h}_1 - \partial_x \left[h_b^n (\partial_{xxx}\hat{h}_1 - q^2 \partial_x \hat{h}_1) + n(\partial_{xxx} h_b) h_b^{n-1} \hat{h}_1 \right] \\ & + q^2 h_b^n (\partial_{xx}\hat{h}_1 - q^2 \hat{h}_1)\,. \end{aligned} \tag{318e}$$

For each value of q, we need to provide an initial perturbation of the Fourier mode with wavenumber q via

$$\hat{h}_1(x, t_0; q) = \hat{h}_{1,t_0}(x; q), \quad \hat{s}_1(t_0; q) = -\hat{h}_{1,t_0}(0; q)/\theta, \tag{318f}$$

where, for simplicity, we have chosen the perturbation of the contact line to be consistent with the first boundary condition in (318b).

Notes on the numerical evaluation

For $n = 0$, the problem (318) was solved with an extension of the numerical scheme used for the base state problem (285), that is, finite differences in space and an extrapolated implicit Euler scheme in time. The initial perturbation $\hat{h}_{1,t_0}$ was set equal to the derivative $\partial_x h_b(x, 0)$ of the initial condition for the base state (287). A different approach was used for $n = 2$, as explained in the part of subsection 6.5.3 focusing on this case. In both cases, the codes were constructed to track the evolution of $\hat{h}_1$ for several wave numbers q simultaneously.

6.5.2 *Asymptotic Analysis*

Solving a time-dependent eigenvalue problem

Notice that the above problem remains coupled to the base state via the second term in (318a) and coefficients in the right hand sides of the second and third boundary conditions in (318b), and that the base state is time dependent. The problem can therefore not be approached by normal modes/separation of variables. For time independent base states, separation of variables leads to an eigenvalue problem, and the long time evolution of the perturbation is usually dictated by the top eigenvalue, which is of often discrete in typical capillary instabilities. We can, however, exploit the fact that for longer times, the base state evolves on a slower time-scale than the typical perturbations and approaches an asymptotically self-similar form. The evolution of the perturbations can then be recovered from the eigenvalue information by using a multiple scales method or WKB approach [44, 69]. We therefore introduce again the slow time scale τ via $t = \tau/\delta$, together with the scalings in (288) and corresponding scalings for the perturbation variables and for the wavenumber, that is,

$$\hat{h}_1 = \delta^{-1/(5-n)}\Phi\,, \quad \hat{s}_1 = \delta^{-1/(5-n)}\hat{S}_1\,, \quad q = \delta^{1/(5-n)}Q\,, \tag{319}$$

Rescaled stability problem

such that the stability problem transforms into

$$\delta^{1/(5-n)}\partial_\tau\Phi - \mathcal{L}(\tau)\Phi = 0 \qquad \text{for } X \geq 0, \tag{320a}$$

$$\theta\partial_X\Phi - \Phi\partial_{XX}H_b = 0, \qquad \text{at } X = 0, \tag{320b}$$

$$H_b^n\left(\partial_{XXX}\Phi - Q^2\partial_X\Phi\right) + nH_b^{n-1}\,\partial_{XXX}H_b\,\Phi - \dot{S}_b\Phi = 0, \qquad \text{at } X = 0, \tag{320c}$$

$$\lim_{X\to\infty}\Phi = 0. \tag{320d}$$

Here

$$\mathcal{L}(\tau)\,\Phi \equiv \dot{S}_b \partial_X \Phi - \partial_X \left[H_b^n \left(\partial_{XXX}\Phi - Q^2 \partial_X \Phi \right) + n(\partial_{XXX} H_b) H_b^{n-1} \Phi \right] + Q^2 H_b^n \left(\partial_{XX}\Phi - Q^2 \Phi \right) \,, \tag{321}$$

and we combined the two boundary conditions in (318b) into one in (320b) .

Step 4: Apply a WKB ansatz..

To exploit the fact that the coefficients in this linear stability problem only change slowly in time, we make a so-called WKB ansatz by introducing

$$\Phi(X,\tau) = \Psi(X,\tau) \exp\left(\frac{\sigma(\tau)}{\delta^{1/(5-n)}} \right) \,. \tag{322}$$

This method has its origin in mathematical physics and is a special case of multiple scale analysis. It represents an efficient method to find approximate solutions to linear differential equations which provide spatially varying coefficients, such as in the present case.
Substituting the above ansatz 322 into the differential equation and canceling out the exponential terms gives

$$\begin{aligned}
\delta^{1/(5-n)} \partial_\tau \Psi + \Psi \partial_\tau \sigma &= \mathcal{L}(\tau)\Psi && \text{for } X \geq 0, && \text{(323a)}\\
\theta \partial_X \Psi - \Psi \partial_{XX} H_b &= 0, && \text{at } X = 0, && \text{(323b)}\\
H_b^n \left(\partial_{XXX}\Psi - Q^2 \partial_X \Psi \right) & \\
+ n H_b^{n-1} \, \partial_{XXX} H_b \, \Psi - \dot{S}_b \Psi &= 0, && \text{at } X = 0, && \text{(323c)}\\
\lim_{X\to\infty} \Psi &= 0 \,. && && \text{(323d)}
\end{aligned}$$

Applying the asymptotic expansions

$$\begin{aligned}
\Psi(X,\tau;\delta) &= \Psi_0(X,\tau) + O(\delta^{1/(5-n)}),\\
\sigma(\tau;\delta) &= \sigma_0(\tau) + O(\delta^{1/(5-n)}),
\end{aligned} \tag{324}$$

together with the expansions (290) for the base state on which the coefficients of this system depend.

Exploiting (292), the leading order problem is

$$\begin{aligned}
\lambda(\tau)\Psi_0 &= \mathcal{L}_0(\tau)\Psi_0 && \text{for } X \geq 0, && \text{(325a)}\\
\theta \partial_X \Psi_0 - \Psi_0 \partial_{XX} H_{b,0} &= 0, && \text{at } X = 0, && \text{(325b)}\\
H_{b,0}^n \left(\partial_{XXX}\Psi_0 - Q^2 \partial_X \Psi_0 \right) & \\
-(1-n)\dot{S}_{b,0}\Psi_0 &= 0, && \text{at } X = 0, && \text{(325c)}
\end{aligned}$$

where

$$\lambda(\tau) \equiv \partial_\tau \sigma_0, \tag{326}$$

$$\mathcal{L}_0(\tau)\,\Psi_0 \equiv (1-n)\dot{S}_{b,0}\partial_X \Psi_0 - \partial_X \left[H_{b,0}^n \left(\partial_{XXX}\Psi_0 - Q^2 \partial_X \Psi_0 \right) \right] + Q^2 H_{b,0}^n \left(\partial_{XX}\Psi_0 - Q^2 \Psi_0 \right) . \tag{327}$$

For $n = 0$, the leading order of (323d) provides a condition in the far-field, while for $n = 2$, the limit $\delta \to 0$ is singular and matching conditions arise at $X = W_{b,0}(\tau)$ instead. The latter will be discussed in detail further below. Our main attention is directed towards determining the perturbations with largest amplification and therefore towards the eigenvalue with largest real part, or top eigenvalue.

..rescale into the slow time-scale of the base state..

Rescaling the variables as in (293), and (311) for $n > 0$, and introducing appropriate scales for the single-mode perturbation, wavenumber and eigenvalue

$$\Psi_0 = \theta^{3/(3-n)} \frac{\phi_1}{\dot{S}_{b,0}^{1/(3-n)}}, \qquad Q = \dot{S}_{b,0}^{1/(3-n)} \frac{\tilde{Q}}{\theta^{n/(3-n)}}, \qquad \lambda = \dot{S}_{b,0}^{(4-n)/(3-n)} \frac{\tilde{\lambda}}{\theta^{n/(3-n)}}, \tag{328}$$

..and solve the time-independent eigenvalue problem

leads to the parameter-free eigenvalue problem

$$\tilde{\lambda}\phi_1 = \tilde{\mathcal{L}}\phi_1 \qquad \text{for } \xi \geq 0, \tag{329a}$$

$$\partial_\xi \phi_1 - \phi_1 \partial_{\xi\xi}\phi_b = 0, \qquad \text{at } \xi = 0, \tag{329b}$$

$$\phi_b^n \left(\partial_{\xi\xi\xi}\phi_1 - \tilde{Q}^2 \partial_\xi \phi_1\right) - (1-n)\phi_1 = 0, \qquad \text{at } \xi = 0, \tag{329c}$$

where

$$\begin{aligned} \tilde{\mathcal{L}}\phi_1 \equiv &(1-n)\partial_\xi \phi_1 - \partial_\xi \left[\phi_b^n \left(\partial_{\xi\xi\xi}\phi_1 - \tilde{Q}^2 \partial_\xi \phi_1\right)\right] \\ &+ \tilde{Q}^2 \phi_b^n \left(\partial_{\xi\xi}\phi_1 - \tilde{Q}^2 \phi_1\right), \end{aligned} \tag{329d}$$

plus the remaining far-field or matching condition.

Case $\boldsymbol{n = 0}$

Stability problem for $n = 0$

For $n = 0$, the remaining condition is

$$\lim_{\xi \to \infty} \phi(\xi) = 0. \tag{330}$$

Moreover, recalling (295), we have

$$\phi_b(\xi) = \frac{2}{\sqrt{3}} \exp\left(-\frac{\xi}{2}\right) \sin\left(\frac{\sqrt{3}}{2}\xi\right) \tag{331}$$

and thus we can set

$$\partial_{\xi\xi}\phi_b|_{\xi=0} = -1 \tag{332}$$

in (329b). Notice that this is the only spot in (329) where the solution of the base state is needed in contrast to the situation for $n > 0$.

Case $n > 3/2$

Stability problem for $3/2 < n < 3$

For $n = 2$ we have a second contact line near the undisturbed film and hence need to determine a matching condition for the inner region ahead of the hump. Similar as for the base state (see Section 6.4) the matching procedure can be generalized and consequently this entire section refers to the cases where $3/2 < n < 3$.

Matching conditions for $3/2 < n < 3$

Consider (318) and pass over to the inner layer analogously as in (306), i.e. rescale x according to (301) and s_b according to (288) while h_b remains unscaled. Rescale $\hat{h}_1$ according to

$$\hat{h}_1 \;=\; \dot{s}_b^{1/3} \cdot w_1 \cdot \hat{h}_{\text{in}} \;=\; \delta^{-n/(3(5-n))} \dot{S}_b^{1/3} \cdot W_1 \cdot \hat{h}_{\text{in}} \,, \tag{333}$$

where w_1 denotes the perturbation of the second contact line and W_1 the corresponding value in outer scalings. Note that this particular scaling results from matching both, base state plus perturbation. Moreover apply the scales (319) for q which altogether leads to the rescaled stability problem

$$\begin{aligned} 0 = \; & -\dot{S}_b \partial_\chi \hat{h}_{\text{in}} + \partial_\chi \left[h_b^n \left(\partial_{\chi\chi\chi} \hat{h}_{\text{in}} \right) + n \left(\partial_{\chi\chi\chi} h_b \right) h_b^{n-1} \hat{h}_{\text{in}} \right] \\ & - \delta^{1/(5-n)} \dot{W}_b \partial_\chi \hat{h}_{\text{in}} + \delta^{4n/(3(5-n))} Q^4 h_b^n \hat{h}_{\text{in}} \\ & - \delta^{2n/(3(5-n))} \left[Q^2 h_b^n \left(\partial_{\chi\chi} \hat{h}_{\text{in}} \right) + \partial_\chi \left(Q^2 h_b^n \partial_\chi \hat{h}_{\text{in}} \right) \right] \\ & + \delta^{(3+n)/(3(5-n))} \left(\dot{S}_b^{1/3} \cdot W_1 \right)^{-1} \partial_\tau \left(\dot{S}_b^{1/3} \cdot W_1 \cdot \hat{h}_{\text{in}} \right) \,. \end{aligned} \tag{334}$$

Applying the asymptotic expansions (290) and (304) as well as

$$\begin{aligned} \hat{h}_{\text{in}}(\chi, \tau; \delta) &= \hat{h}_{\text{in},0}(\chi, \tau) \quad + O(\delta^{1/(5-n)}) \,, \\ W_1(\tau; \delta) &= W_{1,0}(\tau) \quad + O(\delta^{1/(5-n)}) \,, \end{aligned} \tag{335}$$

for $\hat{h}_{\text{in}}$ and W_1, we obtain the leading order equation

$$0 = \; -\dot{S}_{b,0} \partial_\chi \hat{h}_{\text{in},0} + \partial_\chi \left[h_{b,0}^n \left(\partial_{\chi\chi\chi} \hat{h}_{\text{in},0} \right) + n \left(\partial_{\chi\chi\chi} h_{b,0} \right) h_{b,0}^{n-1} \hat{h}_{\text{in},0} \right] \,, \tag{336}$$

which can be integrated once over $[\chi, +\infty)$

$$0 = \; -\dot{S}_{b,0} \hat{h}_{\text{in},0} + h_{b,0}^n \left(\partial_{\chi\chi\chi} \hat{h}_{\text{in},0} \right) + n \left(\partial_{\chi\chi\chi} h_{b,0} \right) h_{b,0}^{n-1} \hat{h}_{\text{in},0} \,. \tag{337}$$

Rescaling $\chi = \xi / \dot{S}_{b,0}^{1/3}$ (analogously as in (306)) reveals the ordinary differential equation

$$0 = \; -\hat{h}_{\text{in},0} + h_{b,0}^n \left(\partial_{\xi\xi\xi} \hat{h}_{\text{in},0} \right) + n \left(\partial_{\xi\xi\xi} h_{b,0} \right) h_{b,0}^{n-1} \hat{h}_{\text{in},0} \tag{338}$$

with solution

$$\hat{h}_{\text{in},0}(\xi) \sim 3 \cdot \left(\frac{n^{3-n}}{3(3-n)(2n-3)} \right)^{1/n} \cdot (-\xi)^{(3-n)/n} \,, \quad \text{for } \xi \to -\infty \,. \tag{339}$$

Matching conditions in outer coordinates

Matching into the outer problem thus requires $\mu_2 = n/(3(5-n))$ and we obtain the outer matching condition

$$\Psi_0(X,\tau) \sim 3 \cdot \left(\frac{-n^{3-n}}{3(n-3)(2n-3)} \right)^{1/n} \dot{S}_{b,0}^{1/n} \cdot W_{1,0} \cdot (W_{b,0}(\tau) - X)^{(3-n)/n} \tag{340}$$

for $X \to W_{b,0}(\tau)$, where $W_{1,0}(\tau)$ represents the δ-leading order perturbation of the second contact line. This matches with the inner expansion. Applying the scales (293) and (328) then reveals

$$\phi_1 \sim 3 \left(\frac{n^{3-n}}{3(3-n)(2n-3)} \right)^{1/n} d_1 (d_b - \xi)^{(3-n)/n} \quad \text{for } \xi \to d_b, \tag{341}$$

where $d_b = \dot{S}_{b,0}^{1/(3-n)} / (\theta^{n/(3-n)}) W_{b,0}$ and $d_1 = \dot{S}_{b,0}^{1/(3-n)} / (\theta^{n/(3-n)}) W_{1,0}$, which closes the eigenvalue problem (329).

Eigenvalue analysis

Case $\boldsymbol{n = 0}$

Eigenvalue problem for $n = 0$

The general solution ϕ_1 of the homogeneous linear differential equation (329a) has the form

$$\phi_1(\xi) = \sum_{j=1}^{4} c_j \exp(k_j \xi), \tag{342}$$

where the k_j are the roots of the fourth order polynomial

$$k_j^4 - 2\tilde{Q}^2 k_j^2 - k_j + \tilde{Q}^4 + \tilde{\lambda} = 0. \tag{343}$$

Roots of the characteristic polynomial

We first restrict our situation to the case where the roots have negative real part, such that the corresponding contributions to (342) satisfy the boundary conditions (330) at $\xi \to \infty$. We now show that there are exactly two of these roots.

Consider

$$f(z) = z^4 - 2\tilde{Q}^2 z^2 - z + \tilde{Q}^4 + \tilde{\lambda}\,, \tag{344}$$

where $z \in \mathbb{C}$ and $\tilde{Q} \geq 0$. We want to show that, if $\tilde{\lambda}$ is in the right half of the complex plane, then $f(z) = 0$ has exactly two solutions with negative real part. Let $\tilde{\lambda} = \tilde{\lambda}_r + i\tilde{\lambda}_i \in \mathbb{C}$, with $\tilde{\lambda}_i \in \mathbb{R}$ and $\tilde{\lambda}_r > 0$.

The argument principle

In the following we will exploit the argument principle in order to prove that $f(z)$ has two zeros in the left half plane, i.e. with negative real part. The argument principle states that, provided that there are no zeros on the boundary, the number of zeros of a polynomial inside a closed curve equals the change in argument over the curve divided by 2π. The closed curve which we would like to consider here is the left half circle of Radius R in the second and third quadrant (that is, start at zero, go along the positive imaginary axis until R, follow the

circle of radius R in positive direction until the negative imaginary axis and then return back to the origin).

First we check that there are no zeros on the boundary. For this purpose we consider $z = ix$, $x \in \mathbb{R}$, on the imaginary axis, $f(z) = 0$ implies that

$$x = \lambda_i \,, \quad \text{and} \quad \left(x^2 + \tilde{Q}^2\right)^2 + \tilde{\lambda}_r = 0 \tag{345}$$

both must be fulfilled, which is impossible since the left hand side of the second equations is always positive, i.e. there are no zeros on the imaginary axis.

We are now in the position to apply the argument principle which requires to compute the change in argument of $f(z)$ in the three segments of our closed curve. For values $z = ix$ on the imaginary axis we have

$$f(ix) = \left(x^2 + \tilde{Q}^2\right)^2 + \tilde{\lambda}_r + i(\tilde{\lambda}_i - x) \tag{346}$$

which always has positive real part so that we can use the formula

$$\arg\left(f(ix)\right) = 2\arctan\left(\frac{\tilde{\lambda}_i - x}{\sqrt{\left(\left(x^2 + \tilde{Q}^2\right)^2 + \tilde{\lambda}_r\right)^2 + (\tilde{\lambda}_i - x)^2} + \left(x^2 + \tilde{Q}^2\right)^2 + \tilde{\lambda}_r}\right) \tag{347}$$

to calculate the change in argument as x takes values between 0 and R. For $x = 0$ we consequently have $\arg(f(0)) = 0$ and as $R \to \infty$ we find $\arg(f(iR)) = 0$, which implies that the argument of $f(z)$ does not change on this part of the path.

On the circular arc, $z = Re^{i\theta}$, with $\pi/2 \leq \theta \leq 3/2\pi$, we have

$$\begin{aligned} f(z) &= R^4 e^{4i\theta} - 2\tilde{Q}^2 R^2 e^{2i\theta} - Re^{i\theta} + \tilde{Q}^4 + \lambda \\ &= R^4 e^{4i\theta}\left(1 - \frac{2\tilde{Q}^2}{R^2 e^{2i\theta}} - \frac{1}{R^3 e^{3i\theta}} + \frac{\tilde{Q}^4 + \lambda}{R^4 e^{4i\theta}}\right) \end{aligned} \tag{348}$$

so as $R \to \infty$ we have $f(z) = R^4 e^{4i\theta}$ and as θ goes from $\pi/2$ to $3/2\pi$ the argument of $f(z)$ goes from 2π to 6π which gives a change in argument of 4π. Finally the negative imaginary axis can be treated analogously as the positive one, resulting in a change in argument of zero. In summary, as $R \to \infty$, the total change in argument is 4π, which implies that there are two zeros in the left half plane.

We denote these roots by k_1 and k_2 and observe that these solutions arise for all $\tilde{Q} \geq 0$ in particular when the real part of $\tilde{\lambda}$ is positive, i.e. $\Re(\tilde{\lambda}) > 0$, which is the region of the complex plane associated with unstable modes.

Linear system for the coefficients c_i

Restricting our attention to these solutions, we have

$$\phi_1(\xi) \;=\; c_1 \exp\left(k_1 \xi\right) \;+\; c_2 \exp\left(k_2 \xi\right). \tag{349}$$

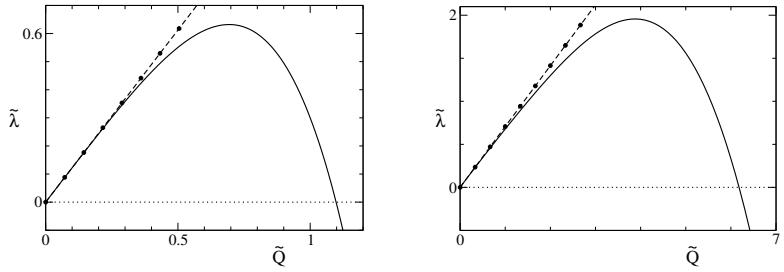

Figure 22: (a), left: Top eigenvalue in the case $n = 0$ for a range of wavenumbers. Results for the exact numerical results for (329) with (330) and (332) are shown by a solid line, and for the long wave analysis (351) by a dashed lines with symbols. (b), right: Top eigenvalue in the case $n = 2$, resulting from solving (329), (341). Linestyles carry over from (a). Figure published in [28].

Substituting (349) into (329b) and (329c) gives a homogeneous linear system of equations for the coefficients c_1, c_2, with the coefficient matrix

$$A = \begin{pmatrix} k_1 + 1 & k_2 + 1 \\ k_1^3 - \tilde{Q}^2 k_1 - 1 & k_2^3 - \tilde{Q}^2 k_2 - 1 \end{pmatrix}, \tag{350}$$

which depends on $\tilde{\lambda}$ via k_1 and k_2. The eigenvalues $\tilde{\lambda}$ are found by solving $\det A = 0$. Numerically, this can be done by finding the intersection of the level sets $\Re(\det A) = 0$ and $\Im(\det A) = 0$ in the $(\Re(\tilde{\lambda}), \Im(\tilde{\lambda}))$-plane. It turns out that for the intersection with largest real part $\Re(\tilde{\lambda})$, the imaginary part $\Im(\tilde{\lambda})$ is zero (within the numerical tolerance). Plotting this $\tilde{\lambda}$ as a function of $\tilde{Q}$ results in the dispersion relation shown in fig. 22(a). We also verified that for this $\tilde{\lambda}(\tilde{Q})$ and for all $\tilde{Q} > 0$, exactly two roots of (343) have non-positive real part, even when, for $\tilde{Q} > 1.10$, the value of $\tilde{\lambda}(\tilde{Q})$ is negative. Thus, $\tilde{\lambda}$ is an isolated eigenvalue.

Numerical procedure

For $\tilde{\lambda}$ with sufficiently small real part, more than two roots of the characteristic polynomial can have negative real part. Then imposing (329b) and (329c) leads to an undetermined system for the coefficients of the decaying exponentials, i.e. which always has nontrivial solutions. Therefore, these $\tilde{\lambda}$ form the essential spectrum of the operator. Due to our previous remark, the essential spectrum is restricted, for all values of $\tilde{Q}$, to a subset of the complex plane with $\Re(\tilde{\lambda}) < 0$. For $\tilde{Q} = 0$, the origin $\tilde{\lambda} = 0$ is equal to the previously discussed isolated eigenvalue and also lies on the boundary of the essential spectrum, which is also the limit for $\tilde{Q} \to 0$ of the isolated eigenvalue discussed above. Similar situations are observed in the analysis of the stability of waves in conservation laws [7, 74, 75, 122].

$\tilde{\lambda}$ with negative real part, the essential spectrum

Case $n > 3/2$

Eigenvalue problem for $3/2 < n < 3$

For $n = 2$, the eigenvalue problem consisting of (329) and (341) was discussed and solved in [58], so we only briefly summarize the results. The essence of these results carries over to the case of general $n > 3/2$. It turns out that for this problem we have two discrete eigenvalues that bifurcate out of the $\tilde{\lambda} = 0$ eigenvalue at $\tilde{Q} = 0$. The dispersion relation for the top eigenvalue, which is the important one for the question of instability, is shown in Fig. 22(b).

Long wave analysis

Linear behavior

Notice that in Fig. 22 the dispersion relation appears to be approximately linear for $\tilde{Q} < 0.3$ and both cases of n, despite the fact that only even powers of $\tilde{Q}$ appear in (329). In fact, for long wavelengths, the eigenvalues can be approximated in terms of small-Q perturbations of the translational mode,

$$\phi_1 = \partial_\eta \phi_b + \phi_{1,1}|\tilde{Q}| + O(\tilde{Q}^2), \qquad \tilde{\lambda} = \tilde{\lambda}_1|\tilde{Q}| + O(\tilde{Q}^2). \tag{351}$$

In addition to the typically expected even powers of $\tilde{Q}$ the expansion also contains odd powers of $\tilde{Q}$ which is due to the fact that the eigenvalue $\tilde{\lambda} = 0$ at $\tilde{Q} = 0$ is degenerate, i.e. belongs to a Jordan block. This is very similar to the situation found for dewetting of a liquid in a slip-dominated case [58]. Proceeding as in that reference, we consider the leading order eigenvalue problem (329) for $0 \leq n < 3$

Generalized long wave analysis for $0 \leq n < 3$

and introduce the expansions

$$\begin{aligned} \phi_1(\xi, \tilde{Q}) &= \phi_{1,0}(\xi,\tau) + \tilde{Q}\,\phi_{1,1}(\xi,\tau) + \tilde{Q}^2\,\phi_{1,2}(\xi,\tau) + O(\tilde{Q}^3), \\ \tilde{\lambda}(\tilde{Q}) &= \tilde{\lambda}_0 + \tilde{Q}\,\tilde{\lambda}_1(\tau) + \tilde{Q}^2\,\tilde{\lambda}_2(\tau) + O(\tilde{Q}^3). \end{aligned} \tag{352}$$

Identifying the parts of $\tilde{\mathcal{L}}_0$ which are independent of and quadratic in $\tilde{Q}$ with $\tilde{\mathcal{L}}_{0,0}$ and $\tilde{\mathcal{L}}_{0,2}$ respectively, i.e.

$$\begin{aligned} \tilde{\mathcal{L}}_{0,0} &\equiv (1-n)\,\partial_\xi - \left(\partial_\xi \phi_b^n\right)\partial_{\xi\xi\xi} - \phi_b^n \partial_{\xi\xi\xi\xi} \\ \tilde{\mathcal{L}}_{0,2} &\equiv (\partial_\xi \phi_b^n)\partial_\xi + 2\,\phi_b^n \partial_{\xi\xi} \end{aligned} \tag{353}$$

we obtain from the leading order problem that $\tilde{\lambda}_0 = 0$ and $\phi_{1,0} = \partial_\eta \phi_b$. Proceeding to $O(\tilde{Q})$ and $O(\tilde{Q}^2)$ then reveals the problems

$$\tilde{\mathcal{L}}_{0,0}\phi_{1,1} = \tilde{\lambda}_1 \partial_\xi \phi_b, \tag{354a}$$

$$\tilde{\mathcal{L}}_{0,0}\phi_{1,2} + \tilde{\mathcal{L}}_{0,2}\partial_\xi \phi_b = \tilde{\lambda}_1 \phi_{1,1} + \tilde{\lambda}_2 \partial_\xi \phi_b\,. \tag{354b}$$

The $O(\tilde{Q})$ problem (354a) implies that $\phi_{1,1}$ must be the λ_1 multiple of the generalized eigenfunction of $\mathcal{L}_{0,0}$ for the eigenvalue $\lambda_0 = 0$ plus an multiple of $\Psi_{0,0} = \partial_X H_{b,0}$, and we obtain

$$\phi_{1,1} = -\frac{\tilde{\lambda}_1}{3-n}\left(\xi\,\partial_\xi \phi_b - \phi_b\right), \tag{355}$$

and substituting this result into (354b) and integrating with respect to ξ yields

$$\int_0^{d_b} \tilde{\mathcal{L}}_{0,2}\partial_{\tilde{\xi}}\phi_b \, d\xi \;=\; -\frac{\tilde{\lambda}_1^2}{3-n} \int_0^{d_b} \xi \, \partial_{\tilde{\xi}}\phi_b - \phi_b \, d\xi \tag{356}$$

for $0 < n < 3$ (note that contributions of $\tilde{\mathcal{L}}_{0,0}\phi_{1,2}$ and $\tilde{\lambda}_2\partial_\eta\phi_b$ vanish due to the boundary conditions for ϕ_b and $O(\tilde{Q}^2)$ boundary conditions for $\phi_{1,2}$) and

$$\int_0^{\infty} \tilde{\mathcal{L}}_{0,0}\phi_{1,2} \, d\xi + \int_0^{\infty} \tilde{\mathcal{L}}_{0,2}\partial_{\tilde{\xi}}\phi_b \, d\xi = -\frac{\tilde{\lambda}_1^2}{3} \int_0^{\infty} \xi \, \partial_{\tilde{\xi}}\phi_b - \phi_b \, d\xi \tag{357}$$

for $n = 0$. In each case the integrals on both sides can be solved and we obtain

$$\tilde{\lambda}_1 \;=\; \pm\sqrt{\frac{3-n}{2}} \, . \tag{358}$$

Notes on the validity

The long wave analysis confirms that as $\tilde{Q} \to 0$, the top eigenvalue decreases to zero and thus converges to a point on the boundary of the essential spectrum. Since the expansions for isolated eigenvalues (see for example Hennessy and Münch [44]) may lose validity if two eigenvalues approach each other, we expect that a similar loss of validity could occur here. This means a separate analysis is needed for the case where $\tilde{Q}$ is allowed to become small as $\delta \to 0$, i.e. for exploring the possibility of distinguished limits arising between these two parameters. However, we expect the growth of perturbations with wave numbers larger than these asymptotically small ones to be more relevant for the question of stability, and will therefore focus on them. We will verify the accuracy of asymptotic estimates derived from the WKB analysis by comparison with numerical results for the initial value problem (318) and point out regions of small wave numbers where we observe a reduction in accuracy.

Case $\boldsymbol{n = 0}$

For $n = 0$ the linear contribution of the long wave expansion for the top eigenvalue, i.e.

$$\tilde{\lambda} = \tilde{\lambda}_1|\tilde{Q}| + O(\tilde{Q}^2); \tag{359}$$

is characterized by the factor

$$\tilde{\lambda}_1 \;\sim\; 1.22 \tag{360}$$

Comparison with numerical computation

according to (358). Good agreement with the numerically found eigenvalues up to $\tilde{Q} = 0.3$ is seen in fig. 22(a) for the positive value for $\tilde{\lambda}_1$. The long wave analysis also allows for an expansion where the $O(\tilde{Q})$ term has the reverse sign, but it turns out that this leads to $\tilde{\lambda}$ in regions of the complex plane where the characteristic equation (343) has more than two roots with negative real part, i.e. which are in the essential spectrum.

Case $\boldsymbol{n = 2}$

The long wave analysis for the top eigenvalue yields

$$\phi_1 = \partial_\eta \phi_b + \phi_{1,1}|\tilde{Q}| + O(\tilde{Q}^2), \qquad \tilde{\lambda} = \tilde{\lambda}_1 |\tilde{Q}| + O(\tilde{Q}^2); \tag{361}$$

with $\tilde{\lambda}_1 = 2^{-1/2}$, according to (358). For the second discrete ("bottom") eigenvalue, the signs of the $O(\tilde{Q})$ corrections need to be reversed. As can be seen from Fig. 22(b), the asymptotic result accurately captures the top eigenvalue obtained from the numerical computation for small $\tilde{Q}$, in fact up to $\tilde{Q} < 1$.

Comparison with numerical computation

6.5.3 *Comparison of asymptotic and numerical solutions*

For these comparisons, we confine ourselves to the values $n = 0$ and $n = 2$ in this section .

Case $\boldsymbol{n = 0}$

Numerical procedure

If we solve (318) for a fixed wavenumber q and a "randomly chosen" initial perturbation (318f), we expect that for long times $t = \tau/\delta$, the solution is approximated by (319), (322), with the leading order behaviour of Ψ and σ given in the subsequent derivations. We can check this by obtaining the solution to (318) numerically and verifying that

$$\frac{d}{dt} \ln \left[||\hat{h}_1(\cdot, t; q)|| \right] = \delta^{4/5} \lambda(\tau; Q) + O(1), \tag{362}$$

where λ is the eigenvalue obtained via (328) and (329), and $||-||$ a convenient norm with respect to x. We will use the maximum norm. With (328), we can in fact write this as

$$\frac{d}{dt} \ln \left[||\hat{h}_1(\cdot, t; q)|| \right] = \delta^{4/5} \dot{S}_{b,0}^{4/3} \tilde{\lambda}(\tilde{Q}) + O(\delta),$$

or, applying $\dot{S}_{b,0} \sim (2/5)^{3/5} \theta^{3/5} (\delta t)^{-3/5}$,

$$\frac{d}{dt} \ln \left[||\hat{h}_1(\cdot, t; q)|| \right] \sim t^{-4/5} \left(\frac{2}{5} \right)^{4/5} \theta^{4/5} \tilde{\lambda}(\tilde{Q}) + O(t^{-1}), \tag{363}$$

with q fixed. We can eliminate the explicit time dependence by using that $\max_x h_b = \delta^{-1/5} \max_X H_{b,0}$ and

$$\max_X H_{b,0} = \left(\frac{2}{5} \right)^{-1/5} \exp\left(-\pi/\sqrt{27} \right) \theta^{4/5} \tau^{1/5} + O(\delta^{1/5}),$$

thus

$$t^{1/5} \sim 1.831 \left(\frac{2}{5} \right)^{1/5} \theta^{-4/5} \max_x h_b,$$

where we have evaluated the exponential expression. We choose $\theta = 1$ and compare the graphs $((1.831 \max_x h_b)\, q, \rho)$ and $(\tilde{Q}, \tilde{\lambda}(\tilde{Q}))$, where

$$\rho(q, t) \equiv (1.831 \max_x h_b)^4 \frac{d}{dt} \ln \left[||\hat{h}_1(\cdot, t; q)|| \right]. \tag{364}$$

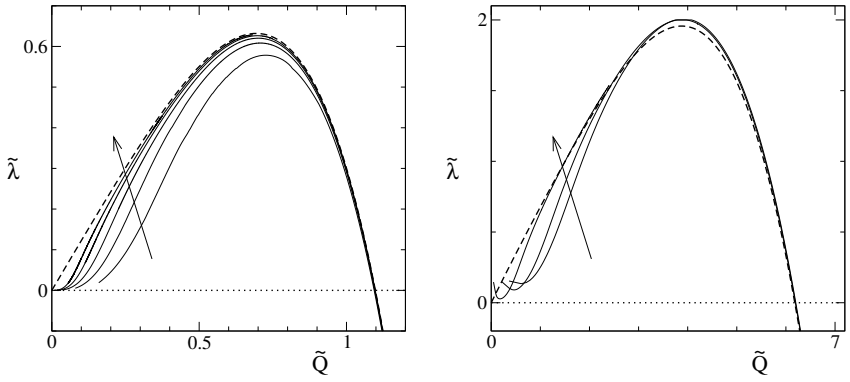

Figure 23: (a), left: Comparison of the amplification rates of the solution to the linear stability problem (318) coupled to (285) with the dispersion relation $\tilde{\lambda}(\tilde{Q})$, for $n = 0$. The dashed line is the top eigenvalue $\tilde{\lambda}(\tilde{Q})$ for (329) and (351) and is the same dispersion relation as in fig. 22(a). The solid lines are the graphs $((1.831 \max_x h_b)\, q, \rho(q,t))$ for amplification rates ρ determined according to (364) for the numerical solutions of (318) coupled to (285), for fixed $q = 1/16$, $1/32$, $1/64$, $1/128$, $1/256$. The arrow points in the direction of decreasing q. Further details are given in the text. (b), right: Comparison for $n = 2$. Dashed line is the dispersion relation as shown in fig. 22(b), solid lines are the amplification rates for $q = 23.7 \times 10^{-3}$, 14.1×10^{-3}, 3.02×10^{-3}, obtained from numerical solutions of the linearized initial value problem for a regularized problem formulation as explained in the main text. The arrow points in the direction of decreasing q. Figure published in [28].

We expect agreement up to an error

$$\rho(q,t) - \tilde{\lambda}(\tilde{Q}) = O((\max_x h_b)^{-1}), \tag{365}$$

where

$$\tilde{Q} = (1.831 \max_x h_b)\, q. \tag{366}$$

The results are shown in Fig. 23. The solid lines with the values for ρ in (364) were obtained from numerical solutions of (318) coupled to (285), while the dashed line with the graph for $\tilde{\lambda}$ is simply the dispersion relation from fig. 22(a). It is visible that the graphs of ρ for different q converge to $\tilde{\lambda}$ as smaller q are chosen, except for a region close to the origin. To understand the convergence, consider two different values for $q = q_1$ and $q = q_2$. These values map to $(1.831 \max_x h_b(x,t))\, q_1$ and $(1.831 \max_x h_b(x,t))\, q_2$, which coincide if we consider different times t_1 and t_2 so that $\max_x h_b(x,t_1) / \max_x h_b(x,t_2) = q_2/q_1$, that is, if the ridge is proportionally larger for the smaller wave number. This also means, according to (365), that the distance between $\rho(q_1,t_1)$ and $\rho(q_2,t_2)$ and the corresponding $\tilde{\lambda}(\tilde{Q})$ is proportionally smaller, for example, by a fact of two if q_1 and q_2 differ by a factor of two. This is approximately the case in the figure, except for very small $\tilde{Q}$. Moreover, for a fixed q, the value of $\max_x h_b(x,t)$ increases as we move to

Convergence for decreasing q

the right in fig. 23, so all curves for ρ are expected to converge to $\tilde{\lambda}$ to the right, which is indeed the case. The different behavior for small $\tilde{Q}$ is also expected in view of the discussion of the validity of the WKB analysis for small wavenumbers.

Case $\boldsymbol{n = 2}$

Equation for the numerical evaluation

For $n = 2$ similar derivations shows that the WKB result implies that

$$\rho(q,t) \equiv \left(\frac{\max_x h_b}{\theta^2 \max_\xi \phi_b} \right)^2 \frac{d}{dt} \ln \left[||\hat{h}_1(\cdot, t; q)|| \right] \tag{367}$$

where $\tilde{Q} = \left(\max_x h_b / (\theta \max_\xi \phi_b) \right) q$, must approach $\tilde{\lambda}(\tilde{Q})$ for fixed q as

Precursor model for the evaluation

$O((\max h_b)^{-1})$. We determine $\rho(q,t)$ from numerical solutions of a regularized thin film equation which includes an intermolecular potential to model the contact line region. This approach avoids a strict contact line at $x = s$ where $h = 0$ by stabilizing a thin precursor of thickness $\nu \ll 1$ and the degeneracy of the partial differential equation (282) leads to singularities in the solution. The sharp interface model with a fixed contact angle condition is recovered in the limit where the precursor thickness becomes small compared to the overall thickness of the film. Details of the model as well as the derivations and the numerical results have been given in [58, 86], so we only use and summarize them here.

The values of ρ obtained from the solutions of the regularized problem are shown by solid lines in Fig. 23(b), each one for a different choice of q. The dashed line is the dispersion relation for (329), (341) also shown in Fig. 22(b). In the same fashion as for $n = 0$, the graphs for ρ converge to a single curve which is slightly larger than the dispersion relation. The deviation is on the order of the precursor thickness, which was chosen to be $\nu = 0.04$. Also as for $n = 0$, the convergence is markedly slower for small values of $\tilde{Q}$.

6.5.4 *Maximal amplification and dominant wavelength*

Superposition of modes

We now would like to consider a superposition of modes with different wavenumbers, i.e.

$$h_1(x,y,t) = \int_{-\infty}^{\infty} \hat{h}_1(x,t;q) \, \exp(iqy) \, dq, \tag{368}$$

in order to determine the dominant wavenumber at a particular time t. Assuming that the rim is perturbed at a time t_0 by an initial perturbation

$$h_{1,t_0}(x,y) = \int_{-\infty}^{\infty} \hat{h}_{1,t_0}(x,q) \, \exp(iqy) \, dq, \tag{369}$$

where the initial amplitude of each contribution has a common fixed value for all wavenumbers, and applying (319) and (322) then results to leading order in

$$h_1(x,y,t) \sim \int_{-\infty}^{\infty} \Psi_0(X,\tau;Q) \exp\left(\int_{t_0}^{t} \lambda(\tau;Q)\, d\tau\right) \exp(iQy)\, dQ. \tag{370}$$

The dominant wavenumber Q_d at a given time t is now the one for which the inner integral is maximal. Rewriting the integral according to (293) and taking derivatives with respect to Q yields

$$\int_{t_0}^{t} \dot{S}_{b,0}\, \tilde{\lambda}'\left(\tilde{Q}(\tau,Q_d)\right)\, d\tau \;=\; 0\,. \tag{371}$$

Rescaling the variables

Expressing the variables in $\tilde{Q}(\tau,Q_d)$ in the following way (for both cases $n=0$ and $n>3/2$)

$$\tilde{Q}(\tau,Q_d) = \frac{\rho_{n,\theta} Q_d}{c(\tau)}\,, \quad \rho_{n,\theta} = \theta^{n/(3-n)}\,, \quad c(\tau) = \dot{S}_{b,0}^{1/(3-n)} \tag{372}$$

and observing that $\tilde{Q}$ is monotonically increasing in τ, since $c(\tau) \sim \tau^{-1/(5-n)}$, we may substitute $\tilde{Q}$ as integration variable and obtain

$$0 \;=\; \int_{\tilde{Q}(t_0,Q_d)}^{\tilde{Q}(t,Q_d)} -\frac{c(\tau)^{5-n}}{\rho_{n,\theta} Q_d c_\tau(\tau)} \tilde{\lambda}'(\tilde{Q})\, d\tilde{Q} \sim \int_{\tilde{Q}(t_0,Q_d)}^{\tilde{Q}(t,Q_d)} \tilde{Q}\lambda'(\tilde{Q})\, d\tilde{Q}\,. \tag{373}$$

Since $\tilde{Q}(t_0,Q_d) = \tilde{Q}(t,Q_d)c(t)/c(t_0) \to 0$ for $t\to\infty$, we can replace the lower integration limit by 0 and integrate (373) by parts to obtain for the asymptotic value of $\tilde{Q} = \tilde{Q}_\infty \equiv \lim_{t\to\infty} \tilde{Q}(t,Q_d)$ the relation

"Equal area rule"

$$\int_0^{\tilde{Q}_\infty} \tilde{\lambda}(\tilde{Q}) - \tilde{\lambda}(\tilde{Q}_\infty)\, d\tilde{Q} \;= 0. \tag{374}$$

The function $\tilde{\lambda}(\tilde{Q})$ is the time-independent dispersion relation, which we computed in Section (6.5.2) for the cases $n=0$ and $n=2$ so we can determine the asymptotic wave number $\tilde{Q}_\infty = \tilde{Q}_\infty(n)$ from this result. The equation (374) has a simple interpretation in that is says that $\tilde{Q}_\infty$ is characterized as the value for which the area underneath the dispersion relation between zero and $\tilde{Q}_\infty$ is equal to the area of the rectangle with corners $(0,0)$ and $(\tilde{Q}_\infty, \tilde{\sigma}(\tilde{Q}_\infty))$. The numerical values we find are $\tilde{Q}_\infty(0) = 0.94$ and $\tilde{Q}_\infty(2) = 5.3$, both rounded to two digits of accuracy.

Dominant wavenumber

The dominant wavenumber in the scalings of the growing rim then is $Q_d = \tilde{Q}(t,Q_d)\; c(\tau)/\rho_{n,\theta}$. We compare this to an intrinsic length scale of the growing rim, for example, a suitably chosen measure of the width, $w(t)$. If the corresponding width for the outer solution is denoted by $\xi_0(n)$, then $w(t) \equiv \xi_0(n)\; \rho_{n,\theta}/c(\tau)$, and we obtain for the dominant wavelength $l_d(t) = 2\pi/Q_d(t)$ the expression

$$\frac{l_d(t)}{w(t)} = \frac{2\pi}{\xi_0(n)\tilde{Q}_\infty}. \tag{375}$$

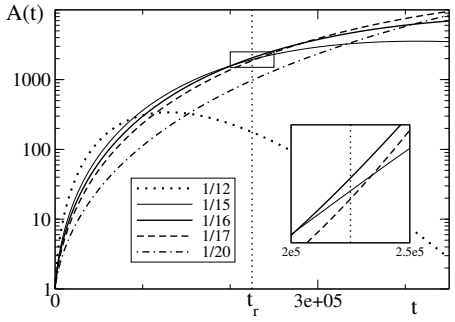

Figure 24: Amplification of perturbations for $n = 0$ for different wave numbers q as shown in the legends. For $q = 12$, the amplification reaches a peak relatively early and the period of decay leads to an amplification less than 1000 at the time where the base state ruptures $t = t_r$ (vertical dotted line, see also fig. 20). Conversely, for $q = 1/20$, the perturbation is still growing and also has an amplification less than 1000 at $t = t_r$. The perturbation with the maximum amplification at $t = t_r$ has wave number $q = 1/16$ (see inset, which is a zoom of the boxed region) and an amplification of about 2000. For $q < 1/16$, a perturbation dominates at a specific time $t > t_r$, and conversely, a perturbation with $q > 1/16$ achieves dominance at at time $t < t_r$ but is then overtaken in particular by the perturbation with with $q = 1/16$. Figure published in [28].

Maximal amplification and film rupture

For $n > 0$, the outer solution for the base state has two contact lines and it is natural to chose their distance for $\xi_0(n) = d_b$, so that in particular for $n = 2$, we have $\xi_0(2) = 1/2$ and therefore $l_d/w = 2.4$. For $n = 0$, we choose the distance between the contact line at $\xi = 0$ and the first zero crossing of (331), which gives $\xi_0(0) = 3.63$, and then $l_d/w = 1.8$. It is also instructive to compare the wavelength with the height of the rim $\max_x h_b$, which is less ambiguous, and this yields $l_d/\max_x h_b = 14$ for $n = 2$ and $l_d/\max_x h_b = 12$ for $n = 0$.

The case $n = 0$

For $n = 2$, the implications for experiments of this results on the dominant wave number was discussed in [85], so we focus here on the case $n = 0$. The first question of interest is of course the maximum amplification achieved at the time when the base state ruptures. While it is difficult to set a specific threshold, it is clear that this amplification has to be significant for a visibly instability to occur while the rim is moving into the unperturbed film. The value of q that will lead to the maximum amplification is the one that, upon rescaling as in (366), is equal to $\tilde{Q}_d$ determined above. Since the value of $\max_x h_b$ at the time of rupture was determined in a previous section following (300b), we can find the estimate $q_d = 1/15.5$. We use this value and adjacent values of q for our numerical solution for (318) and track the amplification

$$A(t;q) = \frac{||\hat{h}_1(\cdot,t;q)||}{||\hat{h}_{1,t_0}(\cdot;q)||}. \tag{376}$$

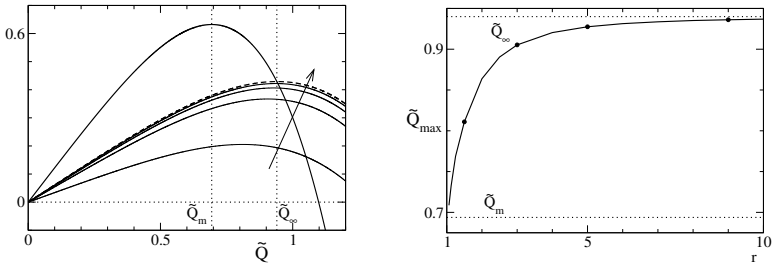

Figure 25: (a) Dispersion relation $\tilde{\lambda}$ (thick solid line), compared to the amplification (except for prefactors) at large times ($r \to \infty$), Ω_∞ (dashed line) and to the amplification at intermediate times, $\Omega(\tilde{Q}, r)$ with $r = 1.5, 3, 5, 9$ (thin solid lines). The arrow indicates increasing values of r. (b) Wave number with maximum amplification for different values of r. Figure published in [28].

The result is shown in fig. 24. Among the wavenumbers used in fig. 24, the maximum amplification at $t = t_r$ is obtained for $q = 1/16$, close to the estimate of $1/15.5$ given above for q_d.

Initial perturbation and amplification rate

For $q = 1/16$, the numerical result gives an amplification of about 2000 at time $t = t_r$ when the base state ruptures and sheds material. The results in fig. 24 were achieved with a specific choice of the initial perturbation $\hat{h}_{1,t_0}$, which was set to be equal to the derivative of the initial profile for the base state (287). We tried other choices, which did not alter the dominant wave number at rupture time, but did have an effect on the amplification rate. The reason for this is that while for the first choice of initial data, the perturbation grew monotonically, there was an initial period of decay for the other choices. This indicates that the initial perturbation contained a higher fraction of modes that were stable and decayed, until finally the growth of the unstable mode dominated the evolution. The minimum was usually achieved early, at $t = 10 \ldots 20$. To take this effect into account, we replaced the denominator in the definition of the amplification (376), and then the final amplification at $t = t_r$ was again close to the value of 2000 stated above.

Fixed dominant wavelength for particular scalings

It is remarkable that a suitable choice of scaling (328) leads to a fixed value $\tilde{Q}_\infty$ for the dominant wavenumber. This suggests that it could be advantageous to formulate the WKB ansatz (322) with σ_0 and τ that depend on $\tilde{Q}$ rather than on Q. This can be achieved by letting $\sigma_0(\tau, Q) = \tilde{\sigma}_0(\tau, \tilde{Q})$, where we have explicitly included the dependence on the wavenumber; similarly for Ψ. The chain rule then implies that in the leading order problem, $\partial_\tau \sigma_0$ has to be replaced by $\partial_\tau \tilde{\sigma}_0 - (\ddot{S}_{b,0}/\dot{S}_{b,0}(3-n))\, \tilde{Q}\, \partial_{\tilde{Q}} \tilde{\sigma}_0$, so that $\tilde{\sigma}$ is determined from the PDE

$$\partial_\tau \tilde{\sigma}_0 - \frac{1}{3-n} \frac{\ddot{S}_{b,0}}{\dot{S}_{b,0}} \tilde{Q}\, \partial_{\tilde{Q}} \tilde{\sigma}_0 = \dot{S}_{b,0}^{\frac{4-n}{3-n}} \tilde{\lambda}(\tilde{Q}), \tag{377}$$

where $\tilde{\lambda}$ is given, as before, by (329). The first order PDE (377) requires initial conditions, and we assume that at some moment τ_0, perturbations are present with amplification factor one for all wavenumbers $\tilde{Q}$, i.e., $\tilde{\sigma}_0(\tau_0, \tilde{Q}) = 0$ for all $\tilde{Q}$. A more general situation could be considered, but this does not lead to an essentially different result. The solution is then given by

$$\tilde{\sigma}_0 = (5-n)\left(\frac{2\alpha}{5-n}\right)^{\frac{4-n}{5-n}} \tau^{\frac{1}{5-n}} \Omega(\tilde{Q}, r), \tag{378a}$$

$$\Omega(\tilde{Q}, r) \equiv \frac{1}{\tilde{Q}}\left[\Lambda(\tilde{Q}) - \Lambda(\tilde{Q}/r)\right], \tag{378b}$$

$$\Lambda(\tilde{Q}) \equiv \int_0^{\tilde{Q}} \tilde{\lambda}(z)dz, \tag{378c}$$

where α is a shorthand for the prefactors in (314) and $r \equiv (\tau/\tau_0)^{1/(5-n)}$.

For $\tau \to \infty$, we have $r \to \infty$ and thus the logarithm of the amplification, $\tilde{\sigma}$, is proportional to

$$\Omega_\infty = \frac{1}{\tilde{Q}} \int_0^{\tilde{Q}} \tilde{\lambda}(z)dz; \tag{379}$$

this is shown in fig. 25(a) by a dashed line and contrasted with the dispersion relation $\tilde{\lambda}(\tilde{Q})$. The maximum of the former curve is shifted compared to the dispersion relation, and in fact, it is equal to $\tilde{Q}_\infty$ determined earlier. Notice that $\tilde{\lambda}$ is the eigenvalue that would have been obtained from a frozen mode analysis of the growing rim, and the comparison clearly shows that as time goes by (and r increases), the wavenumber (in self-similar scales) shifts to larger values (shorter wavelengths). For intermediate values of r, Ω can be determined from (378b). For $r \to 1$, we recover $\tilde{\lambda}(\tilde{Q})$; for $r \to \infty$, the curve quickly converges to Ω_∞. Graphs for Ω are shown for different finite values of r in fig. 25(a).

Comparison to the "frozen mode" wavenumber

Correspondingly, the most amplified wave number $Q_{\max}$ of Ω increases from Q_m, i.e. the maximum for $\tilde{\lambda}$, to Q_∞, determined by (374), as r increases from one to infinity. In fact, convergence is nearly complete already for $r \geq 3$, see fig. 25(b). Because the maximum of the ridge scales like $S_{b,0}^{1/2}$ and (314), the value r can be interpreted as the ratio of the height of the rim at the current time divided by the height at the time when the perturbation is introduced. This implies that after a change in the height of the rim of a factor of three or more is observed as the instability develops, the most amplified wavenumber must be very close to the asymptotic value $\tilde{Q}_\infty$, much closer than to the value $\tilde{Q}_m$ predicted by the frozen mode analysis.

6.6 DISCUSSION AND OUTLOOK

The WKB stability analysis..

In this chapter, we investigated the instability of unsteady and non-

uniform base states for a free boundary problem of the thin-film equation (282), specifically the retracting rim solutions that are susceptible to the "finger" instability. We develop a WKB method to address the multiscale aspects of the linear stability analysis that arise from the time dependence of the base states. The results are used to estimate the amplification of the perturbations and the wavenumber for which this amplification is maximal.

..vs. "frozen mode" analysis

This wavenumber converges to a fixed value $\tilde{Q}_\infty$ scaled with the size of the growing rim, which is larger than the maximum wavenumber of the "frozen mode" dispersion relation. It is interesting to note that nevertheless this value is determined by the dispersion relation through a simple expression (374). It would be interesting to see if this "shift" in the observed wavenumber can be detected in a physical experiment.
We note that the frozen-mode dispersion relation for the class of problems considered in this study has a linear behavior near $\tilde{Q} = 0$, which is in contrast to the quadratic behavior found for the well-studied examples of fingering instabilities for gravity- or Marangoni-driven thin films, [56, 109].

Particular values of n

For $n = 0$, the evolution of the rim is halted by the rupture of the film, but nevertheless, by the time the rupture occurs, the wavenumber has converged close to its asymptotic value. For $n = 2$, the solution evolves into a spatially multilayered structure, which is readily accommodated within the WKB approach. The second value corresponds to the range $3/2 < n < 3$. A generalization of the approach as well as some of the salient results should carry over to the intermediate case $0 < n \leq 3/2$ and also to appropriate formulations of $n \leq 3$, where in addition the contact line singularity needs to be addressed.

Outlook, extension of the method

It would be fruitful to extend our method to a number of further problems with time-dependent base states such as the retracting soap films or surfactant driven films. Moreover, for these and the problems studied in this work, it would also be interesting to investigate the influence of rim curvature in order to, for example, analyze the instabilities which appear in rims of dewetting circular holes.

We are currently considering aspects of the non-linear stability via numerical simulations of (282), in particular the onset of finger pinch-off once they have grown sufficiently.

Part IV

SUMMARY AND OUTLOOK

7

SUMMARY OF RESULTS AND POSSIBILITIES FOR FUTURE RESEARCH

In this dissertation various important mathematical topics concerning solid state dewetting of thin films have been addressed. From the set-up of an anisotropic phase field model for surface diffusion dewetting on a solid substrate, to the derivation of corresponding sharp interface limits, existence of solutions, the numerical simulation and an improved method for the linear stability analysis of a generalized class of thin film equations, many results have been presented. The thesis is summarized on these last pages and at the end possibilities for future research are outlined.

A phase field model for solid state dewetting

The main body of this work begins in Chapter 3 with the formulation of an anisotropic phase field model for solid state dewetting on a solid substrate. The main equations of the resulting model read

$$\begin{aligned} \partial_t u &= \nabla \cdot \mathbf{j}, \\ \mathbf{j} &= m(u)\nabla\mu, \\ \mu &= F'(u) - \epsilon^2 \nabla \cdot \left(\gamma\gamma' \begin{pmatrix} -u_y \\ u_x \end{pmatrix} + \gamma^2 \nabla u \right), \end{aligned} \tag{380}$$

where we consider the homogeneous free energy

$$F(u) = \frac{1}{2}(1-u^2)^2 \tag{381}$$

and the bi-quadratic diffusional mobility

$$m(u) = \left(1-u^2\right)^2. \tag{382}$$

Sharp interface limits

We established, by using an asymptotic analysis which incorporates multiple boundary and interfacial layers as well as techniques of exponential matching, that the present choice of the bi-quadratic mobility (382), combined with the polynomial homogeneous free energy density (381), yields a sharp interface model where surface diffusion is recovered as the dominant driving mechanism, as $\varepsilon \to 0$. We note that this is in contrast to the frequently applied quadratic mobility, which leads to sharp interface models, where a contribution from a non-linear, porous medium like bulk diffusion enters the driving force at the same order of magnitude as surface diffusion, as it has been shown in [64].

The second part of Chapter 3 is concerned with the inclusion of the boundary conditions at the solid substrate

$$\begin{aligned} \epsilon\, \mathbf{n}_\Omega \cdot \left[\gamma(\theta)\gamma'(\theta) \begin{pmatrix} -u_y \\ u_x \end{pmatrix} + \gamma(\theta)^2 \nabla u \right] + \frac{f_w'}{\lambda_m} &= 0, \\ \mathbf{n}_\Omega \cdot (m(u)\nabla\mu) &= 0, \end{aligned} \tag{383}$$

on Γ_w, whereas the boundary conditions on $\partial\Omega \setminus \Gamma_w$ are simply given by

$$\mathbf{n}_\Omega \cdot \nabla u = 0, \qquad \mathbf{n}_\Omega \cdot (m(u)\nabla\mu) = 0. \tag{384}$$

A matching method for the solid boundary

We introduced a matching procedure which exploits another inner layer about the solid substrate and a particular geometry in order to derive the corresponding sharp interface limits of the boundary conditions at the substrate. In particular, the method allows to match the inner and outer layers without matching "into the substrate", which is not well-defined. The result is that the sharp interface limits of the boundary conditions at the substrate recover the Young-Herring equation for the contact angle, and Young's equation in the isotropic case.

Existence of solutions

Chapter 4 presents an existence result for (380), which can be classified as an anisotropic version of the Cahn-Hilliard equation with degenerate mobility. The main difficulty lies in establishing the a priori estimates of Lemma 4.3.7, in particular in view of the degenerate mobility and the non-linear anisotropy function. However, the assumption that the strength of the anisotropy is sufficiently small and considering (380) on a rectangular domain with homogeneous Neumann boundary conditions, enables to apply Lemma 4.3.3 given in the preliminary results of Section 4.3.1. Under these additional assumptions we proved existence of weak solutions in $L^\infty(0,T;H^1(\Omega)) \cap C([0,T];L^2(\Omega))$. Furthermore, we provided that solutions $|u|$ are bounded by one without having a maximum principle.

Numerical simulation

Completing the part which is concerned with the phase field representation, we considered the numerical simulation of (380) with boundary conditions (383)-(384) in Chapter 5. In order to simplify the implementation of the anisotropic boundary conditions we apply a diffuse boundary approximation which suggests to replace μ in (380) by

$$\mu = F'(u) + \delta_{\Gamma_w}\epsilon\frac{f_w'}{\lambda} - \epsilon^2\nabla\cdot\left(\gamma\gamma'\begin{pmatrix}-u_y\\ u_x\end{pmatrix} + \gamma^2\nabla u\right), \tag{385}$$

and consider the boundary conditions

$$\mathbf{n}_\Omega \cdot \nabla u = 0, \qquad \mathbf{n}_\Omega \cdot (m(u)\nabla\mu) = 0, \tag{386}$$

on the whole boundary $\partial\Omega$. We used the method of matched asymptotic expansions in order to show that solutions of the problem including the diffuse boundary approximation converge to those of the original problem. We provide a numerical solution algorithm, applying the finite element method and applying the diffuse boundary approximation. Finally, we present numerical simulations for various initial states which demonstrate the diffuse boundary approximation and reveal some interesting characteristics of solid state dewetting. Motivated by the previous chapters, we address the question of how

the mobility influences the evolution. We compare the results with mobility (382) to the simulations with mobility $m(u) = 1 - u^2$ and demonstrate a significant difference. Considering a fourfold symmetry, for example, leads to film pinch-off in the one case and complete film retraction in the other case. Furthermore, we consider different pinch-off scenarios and anisotropies.

An improved linear stability analysis

The last chapter presents an improved method for the linear stability analysis of unsteady, non-uniform base states in thin film equations of the following form

$$h_t + \nabla \cdot (h^n \nabla \Delta h) = 0, \tag{387}$$

where $h(x, y, t)$ represents the thin film height and $0 \leq n < 3$. Note that the case $n = 0$ corresponds to the small slope approximation of the sharp interface model for surface diffusion dewetting as introduced in Chapter 1.2. Considering (387) on the time-dependent domain $\Omega = \{(x, y);\, s(y, t) < x < \infty,\ -\infty < y < \infty\}$ and with appropriate conditions at the free boundary and in the far field, namely

$$\begin{aligned} h &= 0\,, \quad x = s(y,t) \\ \nabla h \cdot \mathbf{n}_s &= \theta\,, \quad x = s(y,t) \\ h^n \left(\nabla \Delta h \cdot \mathbf{n}_s\right) &= 0\,, \quad x = s(y,t) \\ \lim_{x \to \infty} h &= 1, \end{aligned} \tag{388}$$

we developed a WKB method to address the multiscale aspects of the linear stability analysis that arise from the time dependence of the base states. The results are used to estimate the amplification of the perturbations and the wavenumber for which this amplification is maximal. This wavenumber converges to a fixed value $\tilde{Q}_\infty$, scaled with the size of the growing rim, which is larger than the maximum wavenumber of the "frozen mode" dispersion relation. It is interesting to note that nevertheless this value is determined by the rescaled dispersion relation $\tilde{\lambda}(\tilde{Q})$, where $\tilde{Q}$ is the rescaled wavenumber, through a simple "equal area rule"

"Equal area rule"

$$\int_0^{\tilde{Q}_\infty} \tilde{\lambda}(\tilde{Q}) - \tilde{\lambda}(\tilde{Q}_\infty)\, d\tilde{Q} \; = 0. \tag{389}$$

In addition, we showed that the dispersion relation for the class of problems considered in this study has a linear behavior near $\tilde{Q} = 0$, which is in contrast to the quadratic behavior found for the well-studied examples of fingering instabilities for gravity- or Marangoni-driven thin films, [56, 109].

Extension of the phase field model to 3D

At the end of this thesis, there remain many further interesting question, which constitute possibilities for future research. To begin with, the anisotropic phase field model, as considered in Part II, should be extended to 3D which enables to study the behavior of the three phase

contact line in this case. We note that from liquid dewetting studies it is known that the, typically degenerate, mobility of the governing fourth order parabolic thin film equation does not only control the dewetting rates but also decides the morphology and scale of the contact line instability that arises eventually [3]. In principle, similar scenarios have to be explored here. Moreover, in combination with the anisotropic nature of the solid film, such as for example Si, the evolution of the contact line instability becomes particularly interesting and, according to experimental results [27], depends on the crystalline orientation relative to the contact line. A comparison to realistic experimental results of dewetting solid films would be interesting. To this end it would also be desirable to see the corresponding numerical simulations in 3D.

Generalization of the existence result

In view of the existence result presented in Chapter 4, the most important question is whether the assumptions of Lemma 4.3.3 may be relaxed in order to obtain existence of solution in a more general case. In particular, the existence of solutions on different, not necessarily rectangular, domains would be desirable, which appears to be intuitively possible. Furthermore , it would be interesting to know if there exists a unique solution and study the qualitative behavior, for example as $|u| \to 1$. Just as in the isotropic case we expect that for the present degenerate mobility the sets $\{u = -1\}$ and $\{u = 1\}$ develop an interior which implies a free boundary problem for $\partial\{u = -1\}$ and $\partial\{u = -1\}$, respectively. In addition, it would be interesting to study the asymptotic behavior of solutions in the case as $t \to \infty$.

Uniqueness

Extension of the method for the linear stability analysis

Finally, regarding the improved method for the linear stability analysis presented in Chapter 6, it would be fruitful to extend this method to a number of further problems with time-dependent base states such as the retracting soap films or surfactant driven films. Moreover, for these and the problems studied in this work, it would also be interesting to investigate the influence of rim curvature in order to, for example, analyze the instabilities which appear in rims of dewetting circular holes.

BIBLIOGRAPHY

[1] G. Agbaglah, C. Josserand, and S. Zaleski, *Longitudinal instability of a liquid rim*, Phys. Fluids, 25 (2013), p. 022103.

[2] J. W. Barrett, J. F. Blowey, and H. Garcke, *Finite element approximation of the Cahn-Hilliard equation with degenerate mobility*, SIAM J. Num. Anal., 37 (1999), pp. 286–318.

[3] O. Bäumchen, L. Marquant, R. Blossey, A. Münch, B. Wagner, and K. Jacobs, *Influence of slip on the Rayleigh-Plateau rim instability in dewetting viscous films*, Phys.l Rev. Let., 113 (2014), p. 014501.

[4] F. Bernis and A. Friedman, *Higher order nonlinear degenerate parabolic equations*, J. Diff. Eq., 83 (1990), pp. 179–206.

[5] A. L. Bertozzi, *Symmetric singularity formation in lubrication-type equations for interface motion*, SIAM, J. Appl. Math., 56 (1996), pp. 681–714.

[6] A. L. Bertozzi and M. P. Brenner, *Linear stability and transient growth in driven contact lines.*, Phys. Fluids, 9 (1997), pp. 530–539.

[7] A. L. Bertozzi, A. Münch, M. Shearer, and K. Zumbrun, *Stability of compressive and undercompressive thin film travelling waves*, Europ. J. Appl. Math., 12 (2001), pp. 253–291.

[8] S. Bottin-Rousseau, M. Serefoglu, S. Akamatsu, and G. Faivre, *The surface tension force of anisotropic interphase boundaries is perpendicular to the solidification front during eutectic growth*, IOP Conf. Series: Materials Science and Engineering, 27 (2011), p. 012088.

[9] F. Brochard-Wyart, P.-G. de Gennes, H. Hervert, and C. Redon, *Wetting and slippage of polymer melts on semi-ideal surfaces*, Langmuir, 10 (1994), pp. 1566–1572.

[10] F. Brochard-Wyart and C. Redon, *Dynamics of liquid rim instabilities*, Langmuir, 8 (1992), pp. 2324–2329.

[11] L. Bronsard and F. Reitich, *On three-phase boundary motion and the singular limit of a vector-valued Ginzburg-Landau equation*, Arch. Rat. Mech. Anal., 124 (1993), pp. 355–379.

[12] E. Burman and J. Rappaz, *Existence of solutions to an anisotropic phase-field model*, Math. Meth. Appl. Sci., 26 (2003), pp. 1137–1160.

[13] E. Bussmann, F. Cheynis, F. Leroy, P. Müller, and O. Pierre-Louis, *Dynamics of solid thin-film dewetting in the silicon-on-insulator system*, New J. of Phys, 13 (2011), pp. 043017 1–9.

[14] K. M. Butler and B. F. Farrell, *Three-dimensional optimal perturbations in viscous shear flow*, Phys. Fluids A, 8 (1992), pp. 1637–1651.

[15] J. Cahn, C. Elliott, and A. Novick-Cohen, *The Cahn-Hilliard equation with a concentration dependent mobility: motion by minus the Laplacian of the mean curvature*, Europ. Jour. Appl. Math., 7 (1996), pp. 287–302.

[16] J. Cahn and J. Hilliard, *Free energy of a nonuniform system.I Interfacial free energy*, Jour. Chem. Phys., 28 (1958), pp. 258–267.

[17] J. W. Cahn and J. Hilliard, *Spinodal decomposition: A reprise*, Acta Metall., 19 (1971), pp. 151–161.

[18] J. W. Cahn and J. E. Taylor, *Surface motion by surface diffusion*, Acta Metall. Mater., 42 (1994), pp. 1045–1063.

[19] R. Courant and D. Hilbert, *"Chapter IV. The calculus of variations". Methods of mathematical physics*, Interscience, New York, 1 (1953).

[20] R. V. Craster and O. K. Matar, *Dynamics and stability of thin liquid films*, Rev. Mod. Phys., 81 (2009), pp. 1131–1198.

[21] B. Dacorogna, *Direct methods in the calculus of variations*, Appl. Math. Sc., 78 (1989), pp. 105–108.

[22] S. Dai and Q. Du, *Motion of interfaces governed by the Cahn–Hilliard equation with Highly Disparate Diffusion Mobility*, SIAM J. on App. Math., 72 (2012), pp. 1818–1841.

[23] ——, *Coarsening mechanism for systems governed by the Cahn–Hilliard equation with degenerate diffusion mobility*, Mult. Mod. & Sim., 12 (2014), pp. 1870–1889.

[24] E. Dornel, J.-C. Bare, F. de Crecy, and G. Lacolle, *Surface diffusion dewetting of thin solid films: Numerical method and application to Si/SiO_2*, Phys. Rev. B, 73 (2006), p. 115427.

[25] F. Doumenc, T. Boeck, B. Guerrier, M., and Rossi, *Transient Rayleigh–Bénard–Marangoni convection due to evaporation: A linear non-normal stability analysis*, J. Fluid Mech., 648 (2010), pp. 521–539.

[26] P. Du, M. Khenner, and H. Wong, *A tangent-plane marker-particle method for the computation of three-dimensional solid surfaces evolving by surface diffusion on a substrate*, Comp. Phys., 229 (2010), pp. 813–827.

[27] M. Dufay and O. Pierre-Louis, *Anisotropy and coarsening in the instability of solid dewetting fronts*, Phys. Rev. Lett., 106 (2011), p. 105506.

[28] M. Dziwnik, M. Korzec, M. Münch, and B. Wagner, *Stability analysis of unsteady, non-uniform base states in thin film equations*, SIAM,Mult. Mod. & Sim., 12-2 (2014), pp. 755–780.

[29] B. D. Edmonstone, R. V. Craster, and O. K. Matar, *Surfactant-induced fingering phenomena beyond the critical micelle concentration*, J. Fluid Mech., 564 (2006), pp. 105–138.

[30] J. Eggleston, G. McFadden, and P. W. Voorhees, *A phase-field model for highly anisotropic interfacial energy*, Phys. D, 150 (2001), pp. 91–103.

[31] M. Ellero, X. Hu, J. Frohlich, and N. Adams, eds., *Comprehensive Analysis of Dewetting Profiles to Quantify Hydrodynamic Slip*, Springer, Dordrecht, 2009.

[32] C. M. Elliott and H. Garcke, *On the Cahn-Hilliard equation with degenerate mobility*, Siam J. Math. Anal., 27 (1996), pp. 404–423.

[33] J. Evans, P. Thiel, and M. Bartelt, *Morphological eovlution during epitaxial thin film growth: Formation of 2D islands and 3D mounds*, Surf. Sci. Rep., 61 (2006), pp. 1–129.

[34] L. C. Evans, *Partial differential equations*, vol. 19, Graduate Studies in Mathematics, AMS, Providence, 1998.

[35] J. C. Flitton and J. R. King, *Surface-tension-driven dewetting of Newtonian and power-law fluids*, J. Engrg. Math., 50 (2004), pp. 241–266.

[36] H. Garcke, B. Nestler, and B. Stoth, *On anisotropic order parameter models for multi-phase systems and their sharp interface limits*, Physica D: Nonlinear Phenomena, 115 (1998), pp. 87–108.

[37] H. Garcke and A. Novick-Cohen, *A singular limit for a system of degenerate Cahn-Hilliard equations*, Adv. Diff. Eq., 5 (2000), pp. 401–434.

[38] E. D. Giorgi, *New problems on minimizing movements, in: Boundary value problems for partial differential equations and applications*, RMA Res. Notes Appl. Math., Masson, Paris, 20 (1993), pp. 81–98.

[39] C. Grossmann, H.-J. Roos, and M. Stynes, *Numerical Treatment of partial differential equations*, Springer, 2007.

[40] C. Guggenberger, R. Spatschek, and K. Kassner, *Comparison of phase-field models for surface diffusion*, Phys. Rev. E, 78 (2008), p. 016703.

[41] L. H. Gustavsson, *Energy growth of three-dimensional disturbances in plane poiseuille flow*, J. Fluid Mech., 224 (1991), pp. 241–260.

[42] M. G. Hennessy, V. M. Burlakov, A. Goriely, B. Wagner, and A. Münch, *Controlled topological transitions in thin film phase separation*, WIAS preprint 1885, (2013).

[43] M. G. Hennessy and A. Münch, *Dynamics of a slowly evaporating solvent-polymer mixture with a deformable upper surface*, OCCAM preprint 13/40, Mathematical Institute, University of Oxford, 2013.

[44] M. G. Hennessy and A. Münch, *A multiple-scale analysis of evaporation induced Marangoni convection*, SIAM J. Appl. Math., 73 (2013), pp. 974–1001.

[45] D. S. Henningson, A. Lundbladh, and A. V. Johansson, *A mechanism for bypass transition from localized disturbances in wall-bounded shear flows*, J. Fluid Mech., 250 (1993), pp. 169–207.

[46] C. Herring, *Surface tension as a motivation for sintering*, in The physics of Powder Metallurgy, W. E. Kingston, ed., McGraw-Hill, New York, 1951, pp. 143–179.

[47] K. H. Hoffmann, B. Wagner, and A. Münch, *On the generation and spreading of "finger" instabilities in film coating processes*, Lecture Notes in Computational Science and Engineering, 8 (1999), pp. 245–254.

[48] H. Huppert, *Flow and instability of a viscous current down a slope*, Letters to Nature, 300 (1982), pp. 427–429.

[49] D. Jacqmin, *Calculation of two-phase Navier-Stokes flows using phase-field modelling*, J. Comput. Phys., 155 (1999), pp. 96–127.

[50] ——, *Contact-line dynamics of a diffuse fluid interface*, J. Fluid Mech., 402 (2000), pp. 57–88.

[51] C. Jahan, O. Faynot, L. Tosti, and J. M. Hartmann, *Agglomeration control during the selective epitaxial growth of Si raised sources and drains on ultra-thin silicon-on-insulator substrates*, J. Chryst. Growth, 280 (2005), pp. 530–538.

[52] W. Jiang, W. Bao, C. V. Thompson, and D. J. Srolovitz, *Phase field approach for simulating solid-state dewetting problems*, Acta Mater., 60 (2012), pp. 5578– 5592.

[53] E. Jiran and C. Thompson, *Capillary instabilities in thin, continuous films*, Thin Solid Films, 208 (1992), pp. 23–28.

[54] E. Jiran and C. V. Thompson, *Capillary instabilities in thin films*, J of El. Mat., 19 (1990), pp. 1153–1160.

[55] W. Kan and H. Wong, *Fingering instability of a retracting solid film edge*, J. Appl. Phys., 97 (2005), p. 043515.

[56] D. E. Kataoka and S. M. Troian, *A theoretical study of instabilities at the advancing front of thermally driven coating films*, J. Colloid Interface Sci., 192 (1997), pp. 350 – 362.

[57] J. R. King and M. Bowen, *Moving boundary problems and non-uniqueness for the thin film equation*, European J. Appl. Math., 12 (2001), pp. 321–356.

[58] J. R. King, A. Münch, and B. Wagner, *Linear stability analysis of a sharp-interface model for dewetting thin films*, J. Engrg. Math., 63 (2009), pp. 177–195.

[59] R. Kobayashi, *Modeling and numerical simulations of dendritic crystal growth*, Physica D, 63 (1993), pp. 410–423.

[60] J. Kockelkoren, H. Levine, and W.-J. Rappel, *Computational approach fopr modeling intra- and extracellular dynamics*, Phys. Rev. E., 68 (2003), pp. 1–4.

[61] S. Kodambaka, J. Tersoff, M. C. Reuter, and F. M. Ross, *Germanium nanowire growth below the eutectic temperature*, Science, 316 (2007), pp. 729–732.

[62] M. D. Korzec, P. Evans, A. Münch, and B. Wagner, *Stationary solutions of driven fourth- and sixth-order Cahn-Hilliard-type equations*, SIAM J. Appl. Math., 69 (2008), pp. 348–374.

[63] C. G. Lange, *On spurious solutions of singular perturbation problems*, Studies Appl. Math., 68 (1983), pp. 227–257.

[64] A. A. Lee, A. Münch, and E. Süli, *Sharp-interface limits of the Cahn-Hilliard equation with degenerate mobility*, (2016), pp. 1–26.

[65] F. Leroy, F. Cheynis, T. Passanante, and P. Müller, *Dynamics, anisotropy, and stability of silicon-on-insulator dewetting fronts*, Phys. Rev. B, 85 (2012), p. 195414.

[66] H. Lhuissier and E. Villermaux, *The destabilization of an initially thick liquid sheet edge*, Phys. Fluids, 23 (2011), p. 091705.

[67] X. Li, J. Lowengrub, A. Rätz, and A. Voigt, *Geometric evolution laws for thin crystalline films: Modeling and numerics*, Commun. Comp. Phys., 6 (2009), pp. 433–482.

[68] ——, *Solving pdes in complex geometries: a diffuse domain approach*, Commun. Math. Sci., 7 (2009), pp. 81–107.

[69] W. Lick, *The instability of a fluid layer with time-dependent heating*, J. Fluid Mech., 21 (1965), pp. 565–576.

[70] J. L. Lions, *Quelque méthodes de résolution de problèmes aux limites non linéaires*, Dunod Paris, 1969.

[71] S. Lisini, D. Matthes, and G. Savaré, *Cahn-Hilliard and thin film equations with nonlinear mobility as gradient flows in weighted-Wasserstein metrics*, J. Diff. Eq., 253 (2012), pp. 814–850.

[72] H. Machrafi, A. Rednikov, P. Colinet, and P. Dauby, *Bénard instabilities in a binary-liquid layer evaporating into an inert gas*, J. of Coll. and Int. Sc., 349 (2010), pp. 331–353.

[73] M. A. Makeev, *Self-organized quantum dot superstructures for nanoelectronic and optoelectronic applications.*, J. Nanoel. Optoel., 1 (2006), pp. 176–193.

[74] C. Mascia and K. Zumbrun, *Stability of large-amplitude viscous shock profiles of hyperbolic-parabolic systems*, Arch. Rational Mech. Anal., 172 (2004), pp. 93–131.

[75] ——, *Stability of small-amplitude shock profiles of symmetric hyperbolic-parabolic systems*, Comm. Pure Appl. Math., 57 (2004), pp. 841–876.

[76] M. S. McCallum, P. W. Voorhees, M. J. Miksis, S. H. Davis, and H. Wong, *Capillary instabilities in solid thin films: Lines*, J. Appl. Phys., 79 (1996), p. 7604.

[77] G. B. McFadden, A. A. Wheeler, R. J. Braun, S. R. Coriell, and R. F. Sekerka, *Phase-field models for anisotropic interfaces*, Phys. Rev. E, 48 (1993), pp. 2016–2024.

[78] D. Min and H. Wong, *The effect of strong surface energy anisotropy on migrating grain-boundary grooves*, Jour. Appl. Phys., 100 (2006), p. 053523.

[79] J. Mizsei, *Activating technology of sno2 layers by metal particles from ultrathin metal films*, Sens. Actuators, 16 (1993), pp. 328–333.

[80] L. Modica and S. Mortola, *Il limite nella Γ-convergenza di una famiglia di funzionali ellittici*, Boll Un Mat Ital, 14(5) (1977), p. 526.

[81] W. W. Mullins, *Theory of thermal grooving*, J. Appl. Phys., 28 (1957), pp. 333–339.

[82] W. W. Mullins, *Metal surfaces*, American Society for Metals, Metals Park, OH, (1963), pp. 17–66.

[83] W. W. Mullins and R. F. Sekerka, *Morphological stability of a particle growing by diffusion or heat flow*, Jour. Appl. Phys., 34 (1963), pp. 323–329.

[84] A. Münch and B. Wagner, *Contact-line instability of dewetting thin films*, Physica D, 209 (2005), pp. 178–190.

[85] A. Münch and B. Wagner, *Impact of slippage on the morphology and stability of a dewetting rim*, J. Phys. Condens. Matter, 23 (2011), p. 184101.

[86] A. Münch, B. Wagner, and T. P. Witelski, *Lubrication models with small to large slip lengths*, J. Engrg. Math., 53 (2006), pp. 359–383.

[87] N. Nele Moelans, B. Blanpain, and P. Wollants, *An introduction to phase-field modeling of microstructure evolution*, Calphad, 32 (2008), pp. 268–294.

[88] A. Novick-Cohen, *Triple-junction motion for an Allen-Cahn/Cahn-Hilliard system*, Physica D, 137 (2000), pp. 1–24.

[89] ——, *The Cahn-Hilliard equation*, Handbook of differential equations: evolutionary equations, 4 (2008), p. 931.

[90] N. Owen, J. Rubinstein, and P. Sternberg, *Minimizers and gradient flows for singularly perturbed bi-stable potentials with a dirichlet dondition*, Proc. R. Soc. Lond. A, 429 (1990), pp. 505–532.

[91] R. Passo, H. Garcke, and G. Grün, *On a fourth-order degenerate parabolic equation: Global entropy estimates, existence and qualitative behaviour of solutions*, SIAM J. Math. Anal., 29 (1998), pp. 321–342.

[92] R. L. Pego, *Front migration in the nonlinear Cahn-Hilliard equation*, Proc. Roy. Soc. Lond., 422 (1989), pp. 261– 278.

[93] S. Puri and K. Binder, *Surface effects on spinodal decomposition in binary mixtures and the interplay with wetting phenomena*, Phys. Rev. E, 49 (1994), p. 5359.

[94] A. Rätz, A. Ribalta, and A. Voigt, *Surface evolution of elastically stressed films under deposition by a diffuse interface model*, J. of Comp. Phys., 214 (2006), pp. 187–208.

[95] C. Redon, J. B. Brzoska, and F. Brochard-Wyart, *Dewetting and slippage of microscopic polymer films*, Macromolecules, 27 (1994), pp. 468–471.

[96] G. Reiter and A. Sharma, *Auto-optimization of dewetting rates by rim instabilities in slipping polymer films*, Phys. Rev. Lett., 87 (2001), p. 166103.

[97] J. Robinson, *Infinite-Dimensional Dynamical Systems- From Basic Concepts to Actual Calculations*, Cambridge University Press, 2001.

[98] T. Roubícek, *Nonlinear partial differential equations and applications*, Birkhäuser, 2013.

[99] H. Seidel, *The impact of thermal annealing and adhesion film thickness on the resistivity and the agglomeration behavior of titanium/-platinum thin films*, J. Appl. Phys., 103 (2008), p. 054902.

[100] R. Showalter, *Monotone Operators in Banach Spaces an Nonlinear Partial Differential Equations*, vol. 49, Math. surv. and Mon., 1997.

[101] D. N. Sibley, A. Nold, and S. Kalliadasis, *Unifying binary fluid diffuse-interface motion laws in the sharp-interface limit*, Jour. Fluid Mech., 736 (2013), pp. 5–43.

[102] L. B. Smolka and T. P. Witelski, *On the planar extensional motion on an inertially driven liquid sheet*, Phys. Fluids, 21 (2009), p. 042101.

[103] J. Taylor and J. Cahn, *Diffuse interfaces with sharp corners and facets: Phase field models with strongly anisotropic surfaces*, Phys. D, 112 (1998), pp. 381–411.

[104] C. V. Thompson and J. Ye, *Mechanisms of complex morphological evolution during solid-state dewetting of single-crystal nickel thin films*, Appl. Phys. Let, 97 (2010), p. 071904.

[105] ——, *Anisotropic edge retraction and hole growth during solid-state dewetting of single crystal nickel thin films*, Acta Mat., 59 (2011), pp. 582–589.

[106] S. Torabi, J. Lowengrub, A. Voigt, and S. Wise, *A new phase-field model for strongly anisotropic systems*, Proc. R. Soc. A, 465 (2009), pp. 1337–1359.

[107] L. Trefethen, *Spectral methods in MATLAB*, SIAM, 2000.

[108] L. N. Trefethen, A. E. Trefethen, S. C. Reddy, and T. A. Driscoll, *Hydrodynamic stability without eigenvalues*, Science, 261 (1993), pp. 578–584.

[109] S. M. Troian, E. Herbolzheimer, S. A. Safran, and J. F. Joanny, *Fingering instabilities of driven spreading films*, Europhys. Lett., 10 (1989), pp. 25–30.

[110] Y. Wang, W. Jiang, W. Bao, and D. J. Srolovitz, *Sharp interface model for solid-state dewetting problems with weakly anisotropic surface energy*, Preprint submitted to Elsevier, (2014).

[111] M. R. E. Warner, R. V. Craster, and O. K. Matar, *Unstable van der waals driven line rupture in marangoni driven thin viscous films*, Phys. Fluids, 14 (2002), p. 1642.

[112] W. L. Winterbottom, *Equilibrium shape of a small particle in contact with a foreign substrate*, Acta Metall., 15 (1967), pp. 303–310.

[113] S. Wise, J. Kim, and J. Lowengrub, *Solving the regularized, strongly anisotropic Cahn-Hilliard equation by an adaptive nonlinear multigrid method*, Jour. Comp. Phys., 226 (2007), pp. 414–446.

[114] H. Wong, P. W. Vorhees, M. J. Miksis, and S. H. Davis, *Periodic mass shedding of a retracting solid film step*, Acta Mater., 48 (2000), pp. 1719–1728.

[115] G. Wulff, *Zur Frage der Geschwindigkeit des Wachstums und der Auflösung der Krystallflächen*, Z. Krystallogr. Miner., 34 (1901), pp. 449–530.

[116] T. Young, *An essay on the cohesion of fluids*, Philos. Trans. Roy. Soc. London, 95 (1805), pp. 65–87.

[117] P. Yue, J. Feng, C. Liu, and J. Shen, *A diffuse-interface method for simulating two-phase flows of complex fluids*, J. Fluid Mech., 515 (2004), pp. 293–317.

[118] P. Yue, C. Zhou, and J. Feng, *Sharp-interface limit of the Cahn-Hilliard model for moving contact-lines*, J. Fluid Mech., 645 (2010), pp. 279–294.

[119] E. Zeidler, *Nonlinear functional analysis and its applications. II/B.*, Nonlinear monotone operators, Springer-Verlag, New York, 1990.

[120] J. Zhu, L. Q. Chen, J. Shen, and V. Tikare, *Coarsening kinetics from a variable-mobility cahn-hilliard equation: Application of a semi-implicit fourier spectral method*, Phys. Rev. E., 60 (1999), pp. 3564–3572.

[121] R. Zucker, G. H. Kim, W. C. Carter, and C. V. Thompson, *A model for solid-state dewetting of a fully-faceted thin film*, C. R. Phys., 14 (2013), pp. 564–577.

[122] K. Zumbrun and P. Howard, *Pointwise semigroup methods and stability of viscous shock waves*, Indiana Univ. Math. J., 47 (1998), pp. 741–872.